Pressure–temperature–time (P–T–t) evolution of schist in the Qinling Orogenic Belt, China

Thesis submitted in accordance with the requirements of the University of Adelaide for an Honours Degree in Geology

Jan Varga

November 2016

THE UNIVERSITY of ADELAIDE

PRESSURE–TEMPERATURE–TIME (*P–T–t*) EVOLUTION OF SCHIST IN THE QINLING OROGENIC BELT, CHINA

RUNNING TITLE: *P–T–t* evolution of schist in the Qinling Orogenic belt

ABSTRACT

The Qinling Orogenic Belt marks the amalgamation of the South and North China Cratons during a protracted but punctuated period spanning the Neoproterozoic through to Triassic. The complex evolution of the Qinling Orogen has been extensively studied through U–Pb zircon geochronology, but lacks fundamental characterisation of its thermal history. Moreover, metamorphic studies, of which there are few, focus on high-pressure rocks at the margins of major tectonic divisions within the architecture of the Qinling Orogen. Cordierite schists investigated in this study have metamorphic monazite age affinities to Late Triassic magmatism and metamorphism in the South Qinling Belt (SQB) occurring at 220–230 Ma. Calculated phase equilibrium modelling constrains metamorphism to 0.60–4.25 kbar and 540–570 ˚C, corresponding to steep (extreme) apparent thermal gradients between 135–900 ˚C/kbar. This probably represents contact metamorphism of the Liuling Group turbidite sequence by intruding magmas. Garnet–staurolite schist within the North Qinling Belt (NQB) has metamorphic monazite age data that overlaps with Late Palaeozoic events occurring at ca. 400 Ma. Calculated phase equilibrium modelling constrains peak metamorphism to ~7.1 kbar and 615 ˚C, corresponding to a thermal gradient of ~87 ˚C/kbar. This represents Barrovian-style metamorphism of forearc sedimentary units during arc-continent collision marking the closure of the Shangdan Ocean. Metamorphism of these forearc sequences has a comparable thermal gradient to Guishan Complex equivalents in the Tongbai Orogen, which comprises a continuation of the Qinling to the east. This study establishes previously undocumented contact metamorphism in the northern SQB and Barrovian-style metamorphism in the NQB providing fundamental data that is vital for better constrained tectonic models of the evolution of the Qinling Orogenic Belt.

KEY WORDS

Qinling Orogenic Belt, South China Craton, North China Craton, metamorphism, pseudosection, U–Pb geochronology, monazite, zircon

TABLE OF CONTENTS

LIST OF FIGURES AND TABLES

INTRODUCTION

The Qinling Orogenic Belt (QOB) is located in central China, and forms part of an extensive orogenic system known as the Central China Orogen (CCO). The QOB separates the North China Craton (or North China Block, NCB) and South China Craton (or South China Block, SCB) connecting from east to west the Dabie, Qinling, Qilian and Kunlun Mountains (Bader et al., 2013), and is a complex belt representing the amalgamation of the two cratons (Gilder & Courtillot, 1997; Meng & Zhang, 1999, 2000; Tao et al., 2003; Diwu et al., 2012; Tang et al., 2015; Dong & Santosh, 2016). In particular, the QOB involves a number of terranes that are proposed to have collided through a series of subduction-related collision processes. This has given rise to a large amount of research, from which several tectonic models have been proposed for the orogen (e.g. Bader et al., 2013; Dong & Santosh, 2016; Liu et al., 2016), often with contradicting scenarios.

Of the large number of studies, the few that are metamorphic in nature have tended to focus on either high-pressure–ultra-high-pressure (HP–UHP) mafic rocks at the margins of some terranes in the QOB and/or the ages of metamorphism, as summarised in Table 1 (e.g. Bader et al., 2013; Dong & Santosh, 2016; Liao et al., 2016). Very few of these studies have provided quantitative thermobarometry (e.g. pseudosections) coupled with age data (Xiang et al., 2012; Bader et al., 2013; Tang et al., 2016). Therefore, a paucity exists in quantitative characterisation of the thermal (metamorphic) history of the interior regions of QOB terranes. This paucity results in an overall lack of understanding of the thermal character of the orogen, and more importantly, means that tectonic models proposed for the development of the QOB lack fundamental constraints provided by the thermobarometric record.

In this study, metasedimentary rocks are used to constrain the thermal structure of the North Qinling Belt (NQB), and the Devonian Liuling Group of the South Qinling Belt (SQB), both in the region south of Xi'an (Fig. 1). Calculated *P–T* pseudosections for schist boulders located in north flowing rivers are coupled with U–Pb LA–ICP–MS geochronology of in-situ monazite and mounted monazite and zircon to constrain the *P–T–t* history. Collectively, these results provide a basis for interpreting samples in the context of the existing tectonic framework as well as offering insights into the geodynamics of the QOB.

GEOLOGICAL SETTING

The QOB is an E–W trending belt in central China that is approximately 300 km wide (Fig. 1). It occurs between, and marks the amalgamation of, the NCB and SCB (Dong & Santosh, 2016 and references therein) during a protracted but punctuated period spanning the Early Neoproterozoic through to Triassic (Dong & Santosh, 2016; Zhang et al., 2016). From north to south the QOB consists of four major tectonic units, the Southern-North China Craton (S-NCB; Archean to Paleoproterozoic rocks), the North Qinling Belt (NQB), South Qinling Belt (SQB) and the Northern-South China Craton (N-SCB; Late Archean to Early Proterozoic rocks) (e.g. Fig. 1; Tang et al., 2015). Within these belts are numerous E–W trending terranes that document the complexity that amalgamation involved, including interpreted arcs, basins, ophiolites and accretionary wedges (Dong et al., 2013; Tang et al., 2016).

North Qinling Belt, NQB

The NQB comprises several groups, bound to the south by the Shangdan Suture (SDS) and to the north by the Luonan-Luanchuan-Fault (LLF) (Fig. 1). From north to south, groups that define the NQB are: The Kuanping Group, Erlangping Group, Qinling Group, Danfeng Group and Songshugou Ophiolite (Fig. 1 & 2). Major faults separate these Groups (Zhao et al., 2015). To the south of the SDS, forearc sequences (FAS) are separated from the northern SQB by a shear zone (Dong et al., 2013). As the extent of the FAS is unclear, and is commonly incorrectly identified as SQB sediments (Zhao et al., 2015) it has been inferred (Fig. 1c).

The Kuanping Group consists of an ophiolitic unit and metamorphosed clastic unit (Zhang et al., 1994; Zhang & Zhang, 1995). Metasediments yield detrital U–Pb zircon ages between 610–500 Ma (Dong & Santosh, 2016).

The Erlangping Group is interpreted as a Palaeozoic back-arc basin, consisting of metavolcanic and metasedimentary rocks, possibly deposited during the Cambrian–Ordovician (Lu et al., 2003). Closure of the basin occurred at ca. 450 Ma (Dong & Santosh, 2016).

The Qinling Group consists of biotite gneisses, metapelites (e.g. Table 1; Chen et al., 2006), amphibolite and marble with a maximum deposition in the early Neoproterozoic (Lu et al., 2006; Liu et al., 2013; Shi et al., 2013). Metamorphism is poorly age constrained to periods during the Neoproterozoic (ca. 1000 Ma; You et al., 1991) and Early Palaeozoic (510-380 Ma; e.g. Fig. 2; Bader et al., 2013; Dong & Santosh, 2016) that includes migmatisation (Tang et al., 2015).

The SDS, represented by the Danfeng Group and Songshugou Ophiolite, comprises discontinuous melange outcrop and eclogite-facies mafic-ultramafic rocks (Table 1), with U–Pb ages of 530–420 Ma (Fig. 2; Yan et al., 2009; Dong et al., 2011a).

Forearc sequences (FAS) to the NQB, located south of the SDS, characterised by highly deformed schist, psammite, marble and volcanoclastics defined by a maximum deposition age of ca. 435 Ma in the vicinity of location 2 (Fig. 1; Dong et al., 2013) and 389–330 Ma ~200 km east (Yan et al., 2016). The FAS is interpreted to form in a forearc basin to, and receiving continental arc detritus from, the NQB (Dong et al., 2013).

South Qinling Belt, SQB

The South Qinling Belt is located south of the SDS (Fig. 1). The Mianlue suture separates the SQB from the N-SCB (Fig. 1). Neoarchean–Proterozoic rocks form the basement, with Neoproterozoic to Triassic cover sequences (Zhang et al., 2001). The SQB is dominated by Triassic granitoids and dykes aged between 245–200 Ma (Zhang et al., 2016). Few of these granitoids intrude the southernmost NQB (Fig. 1).

Along the northern margin of the SQB, the Liuling Group is a Middle–Late Devonian turbidite package (Fig. 2) that is interpreted to represent the foreland basin to the NQB after the closure of the Shangdan Ocean (Dong et al., 2013). The group comprises several thousand metres of flysch sediments, including sandstone, siltstone and mudstone (Dong et al., 2013). It is characterised by detrital zircon age signatures from both the SQB and NQB, indicating the closure of the Shangdan Ocean and uplift of both belts (Dong & Santosh, 2016).

Tectonic evolution

Tectonic models for the evolution of the QOB typically involve, in age order, southward-directed subduction of the Kuanping Ocean initiated ca. 1000 Ma, followed by closure at ca. 900–850 Ma (Dong & Santosh, 2016) resulting in voluminous 979–844 Ma magmatism intruding the Qinling Group (Dong et al., 2011b). Northward-directed subduction of the Shangdan Ocean to the south of the NQB occurred during the Palaeozoic (ca. 534–420 Ma), resulting in voluminous 534–403 Ma arc-related intrusions (Dong & Santosh, 2016). Existence of the Erlangping back-arc basin is temporally coeval with the Shangdan Ocean that amalgamated the SQB and NQB. During this time (458–434 Ma), the SQB was separated from the N-SCB by the Mianlue Ocean (Dong & Santosh, 2016). Exhaustion of the Shangdan oceanic lithosphere up to ca. 420 Ma was succeeded by arc-continent collision and continental subduction of the SQB resulting in a foreland basin from the Middle Devonian to Lower Triassic (Dong & Santosh, 2016). At ca. 250 Ma the Mianlue Ocean subducted north underneath the SQB (Lai & Qin, 2010). The closure of Mianlue Ocean resulted in voluminous 245–215 Ma magmatism in the SQB during a period of orogenic thickening (Zhang et al., 2016). Post-orogenic collapse and extension of the SQB resulted in partial melting and migmatisation 215–200 Ma (Zhang et al., 2016). These events are shown in a time-space plot (Fig. 2).

Study area and sample selection

Samples for this study are boulders of schist collected from two north-flowing streams in heavily forested river gorges in the Qinling Mountains, within the NQB. The only accessible outcrop/rock in this part of the Qinling Mountains is along the steep river gorges. Granitoids dominate the total volume of boulders (~99%) within these mountain streams and schist forms a very minor component. The sample sites, and morphology of the streams, are shown in Fig. 3. Samples were attained for this study during field seasons in June 2015 and April 2016.

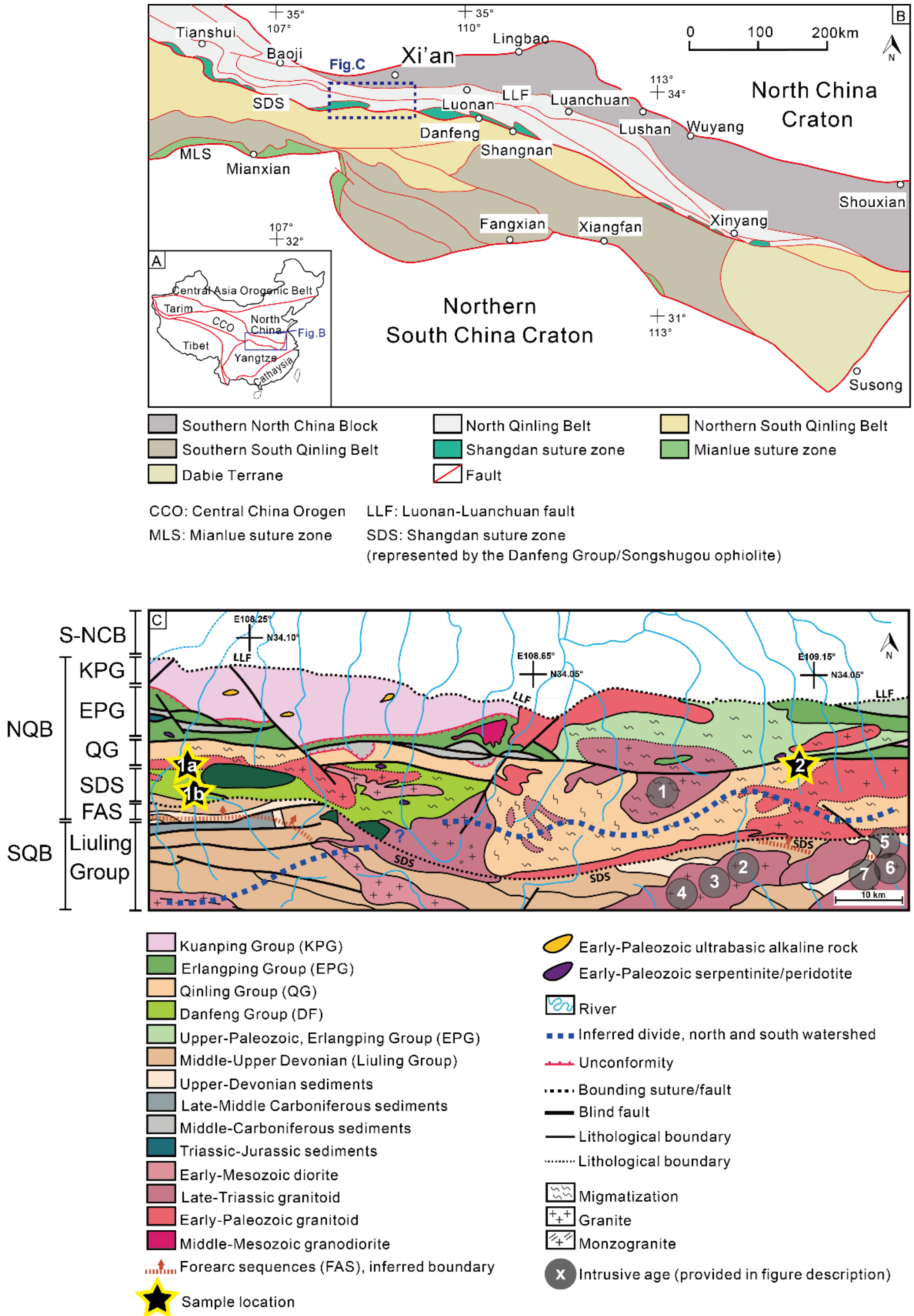

Figure 1: (A) Simplified geological map showing the extent of the Central China Orogen with respect to adjacent craton blocks in China (modified after Tang et al., 2016); (B) Simplified map of the Qinling Orogenic Belt including sutures and faults bounding major tectonic divisions (modified after Tang et al., 2016); (C) Geological map of the study area (adapted from 1:1 000 000 Geologic and Tectonic Maps of the Qinling—Daba Mountains (Zhang, 1992, Zhang et al. 2001). Stars depict sample locations within the North Qinling Belt. Shangdan Suture Zone (SDS, dashed line) marks the boundary between the North and South Qinling Belts. Ages in Ma represented by numbered circles are; (1) 227 ± 3.6 (Jiang et al., 2009); (2) 218 ± 2.4 (Jiang et al., 2009); (3) 210 ± 3 (Sun et al., 2000); (4) 219 ± 2 (Yang et al., 2006); (5) 224 ± 1.1 (Hujun et al., 2009); (6) 213 ± 1.8 (Hu et al., 2004); (7) 209 ± 2 (Hu et al., 2004).

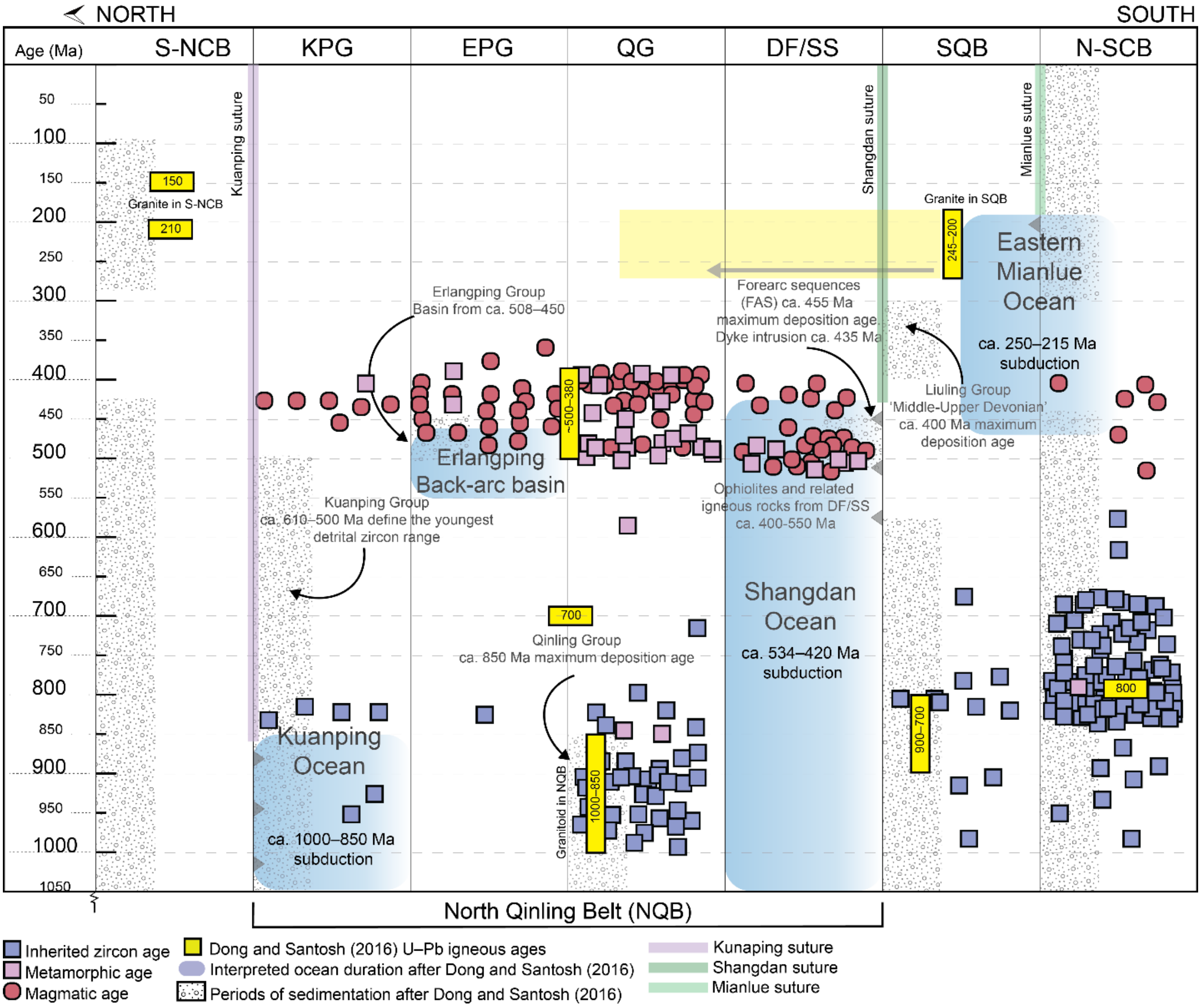

Figure 2: Time-space plot compiled for the northern portion of the Qinling Orogenic Belt, as far south as the N-SCB. Data points are from U–Pb and Th–Pb ages summarized in supplementary material provided by Bader et al. (2013) as 'Table S1'. Red circles represent magmatic ages, blue boxes represent inheritance ages (of igneous rocks), and pink squares represent metamorphic ages from zircon, monazite and titanite. Yellow rectangles represent major magmatic crystallisation ages, identified by Dong and Santosh (2016). Stippled texture in columns represents periods of sedimentation. Columns with a fading blue gradient correspond to interpreted oceans occurring in the history of amalgamation of the QOB.

Table 1: Collection of published literature—summarizing available *P–T–t* conditions and associated thermal gradients. The following describe the means by which *P–T* estimates were determined; CTB = conventional thermobarometry, TC = THERMOCALC, TD = Theriak Domino.

Location	Rock type	*P–T* conditions (CTB, TC, TD)	Thermal gradient (˚C/kbar)	Age (Ma)	Interpretation/comment	Reference
Kuanping Group						
1	Mylonite and mylonitised gneiss			Muscovite $^{40}Ar/^{39}Ar$ 372 ± 1.6, 381.4 ± 1.4, Biotite $^{40}Ar/^{39}Ar$ 372.98 ± 0.94, 372.9 ± 1.2, 371 ± 1	Fault activation	(Song et al., 2009)
2	Amphibolite	Amphibolite facies		Hornblende $^{40}Ar/^{39}Ar$ 434.5 ± 1.8		(Zhai et al., 1998)
3	'Meta-neutral acidic rock'			Zircon 416, 423 and 424	Chinese literature	(Dunyi & Dunmin, 1988)
4	Deformed pegmatite and garnet amphibolite	Amphibolite facies		Zircon 439 ± 24, 442 ± 6, 415 ± 5	Metamorphic ages, ca. 440 Ma upper limit metamorphism, ca. 415 Ma as a result of Pb loss	(Liu et al., 2011)
5	Garnet-biotite-quartz schist			Biotite $^{40}Ar/^{39}Ar$ 319 ± 3.6	Chinese literature, most likely fault activation	(Yan et al., 2008)
6	Mica-schist			Biotite $^{40}Ar/^{39}Ar$ 328 ± 7; Muscovite $^{40}Ar/^{39}Ar$ 348 ± 7		(Mattauer et al., 1985)
Erlangping Group						
1	Pillow basalt	Greenschist facies		Whole-rock Rb-Sr 401.9 ± 6.3		(Sun et al., 1996)

2	Pillow basalt	Greenschist facies	Whole-rock Rb-Sr 405 ± 22	Resetting ‘metamorphic event’	(Sun et al., 2002a)
3	Garnet amphibolite		Zircon 440 ± 3, 394 ± 5, 359 ± 6	ca. 440 Ma due to amphibolite facies metamorphism. Younger ages represent ‘metamorphic-deformational event’	(Liu et al., 2011)
4	Intrusive diorite and amphibolite		Horblende $^{40}Ar/^{39}Ar$ 433 ± 2 (diorite), 404 ± 5		(Zhai et al., 1998)
Qinling Group					
1	Staurolite + kyanite + garnet and sillimanite + andalusite + garnet + staurolite paragneiss		Monazite EPMA 520 ± 23, 435 ± 9	Subduction-accretion along Gondwana, subduction-collision Proto-Tethys	(Chen et al., 2006)
2	Felsic gneiss		Zircon 511 ± 35, 507 ± 37	Peak metamorphism, >120 km subduction based on diamond identification	(Yang et al., 2003)
3	Gneiss		ZIrcon 508 ± 12	Peak metamorphism	(Liu et al., 2003)
4	Paragneiss, diamond bearing		Zircon 493 ± 170	Peak metamorphism, continental subduction based on coesite and diamond identification	(Yang et al., 2005)
5	Eclogite		Zircon 505 ± 12	>90 kb based on diamond and coesite, continental subduction	(Liu et al., 2010)
6	Eclogite		Zircon 502 ± 11	Peak metamorphism - Chinese literature	(Chen & Liu, 2011)

7	Eclogite	660–710 ˚C, 26–28 kb (CTB & TD)		Zircon 501 ± 9	Peak metamorphism	(Cheng et al., 2012)
8	Eclogite			Zircon 489 ± 6, 484 ± 5, 490 ± 6	Subductoin of NQT under EPG No P-T work	(Wang et al., 2011)
9	Eclogite			Lu-Hf garnet 494 ± 3, Zircon 490 ± 4	Eclogite facies ‘recrystallization’ and minimum ecl. Metamorphism age	(Cheng et al., 2012)
10	Eclogite	*P–T* conditions cited from Cheng et al. (2012)		Zircon 490 ± 12	NQT subduction under EPG (continental eclogite)	(H. Wang et al., 2013)
11	Retrograde eclogite			Zircon 490 ± 4, 473 ± 4	Peak and retrograde, respectively	
12	Retrograde eclogite			Garnet-Amphibole Lu–Hf 414 ± 1	Retrograde	(Cheng et al., 2011)
13	Retrograde eclogite			Garnet-Amphibole Sm–Nd 400 ± 8	Retrograde, interpreted with caution – thought to consist of mnz/ttn inclusions	(Cheng et al., 2011)
14	Retrograde eclogite			Zircon 490 ± 6, 453 ± 9	Peak and retrograde, respectively	(Liu et al., 2013)
15	Two-pyroxene and garnet-granulites (mafic protolith)	757–840 ˚C, ~9.5 kbar (CTB)	~80–88	Zircon ca. 470–435		(Kröner et al., 1993)
16	Biotite-gneisses (amphibole and biotite analysis)			^{40}Ar/^{39}Ar below 540 °C ca. 400 Ma. Below 300 °C 330–340 Ma or 368	Exhumation	(Dong et al., 2011c)

17	Amphibolite, diamond bearing	>40 kbar, 1-2 µm diamond inclusion		Zircon 490 ± 6	Peak metamorphism	(Wang et al., 2014)
18	Retrograded eclogite	760–770 ˚C, 11.4–14.0 kbar, and 679–765 ˚C, > 16.7 kbar (TC)	~67–55 and ~40–46	Zircon 497 ± 2 (Peak), 461 ± 5, 425 ± 3 (Retrograde)	Peak and retrograde metamorphism	(Liao et al., 2016)
19	Retrograded eclogite	800–850 ˚C, 14.5–15.6 kbar and 795–855 ˚C, 8.3–10 kbar (TC)	~55–54 and ~96–85	Zircon 501 ± 9, 471 ± 8	Peak and retrograde metamorphism, respectively	(Liao et al., 2016)
20	Two pyroxene granulite			Zircon 440 ± 2, 426 ± 1	Retrograde metamorphism	(Zhang et al., 2011)
	Garnet amphibolite			Zircon 503 ± 5 (Peak), 452 ± 5, 400 ± 3 (Retrograde)	Peak and retrograde metamorphism	Liu et al. (2013)
21	Garnet amphibolite (retrogressed eclogite)	550 ˚C, ~31 kbar (TD)	~18			(Bader et al., 2013)
22	Garnet gneiss	635 ˚C, 10.6 kbar (TD)	~60			(Bader et al., 2013)
23	Garnet-phengite gneiss	633 ˚C, 15.4 kbar (TD)	~40	$^{40}Ar/^{39}Ar$ Mica 470 ± 1	Retrograde metamorphism	(Bader et al., 2013)
24	Garnet amphibolite (retrogressed eclogite)	660 ˚C, 21.5 kbar (TD)	~30			(Bader et al., 2013)
25	Garnet amphibolite (retrogressed eclogite)			Titanite 471 ± 17	Retrograde metamorphism	(Bader et al., 2013)
26	Garnet-sillimanite gneiss (migmatite)	743 ˚C, 7.1 kbar (TD)	~105	Zircon 502.4 ± 5.9		(Bader et al., 2013)

27	Granite (post-migmatitic)			Monazite 394.9 ± 3.3		(Bader et al., 2013)
28	Meta-granite (weakly recrystallized)			Zircon 450.6 ± 3.1		(Bader et al., 2013)
29	Amphibolite			Zircon 401.7 ± 4.3		(Bader et al., 2013)
30	Pegmatite (leucosome)			Zircon 400.6 ± 3.1		(Bader et al., 2013)
31	Garnet-sillimanite gneiss (melanosome)	699 ˚C, 6.6 kbar (TD)	~106			Bader et al. (2013)
32	g-sill gneiss (melanosome)	693 ˚C, 7.2 kbar (TD)	~96			(Bader et al., 2013)
33	Amphibolite			Titanite 404.6 ± 3.6	Described as 'syn-kinematic'. Age of deformation	(Bader et al., 2013)
34	Garnet-sillimanite gneiss (melanosome)	722 ˚C, 6.2 kbar (TD)	~116			(Bader et al., 2013)
35	Mylonitic garnet-gneiss (post-migmatitic leucogranite)			Monazite 397.1 ± 5.4	Minor age at 352 Ma, monazite age interpreted as age of deformation (resetting)	(Bader et al., 2013)
36	Garnet-gneiss (blasto-mylonite; melanosome)	712 ˚C, 6.1 kbar	~117	Monazite 380.5 ± 7.4	Minor age at 352 Ma, monazite age interpreted as age of deformation (resetting)	(Bader et al., 2013)
37	Garnet-hornblende-biotite schist (melanosome)	675 ˚C, 7.2 kb–760 ˚C, 6.8 kbar (TD)	~95–112	Zircon 464.0 ± 2.9	Minor age at 505 Ma. Metamorphic age	(Bader et al., 2013)
38	Garnet-gneiss	754 ˚C, 7.5 kbar (TD)	~100	Zircon 487 ± 11	2 grains, mostly Neoproterozoic dataset	(Bader et al., 2013)

39	Syeno-granite (post-migmatitic)			Monazite 392.4 ± 4.2	Minor age at 354 Ma related to deformation (resetting)	(Bader et al., 2013)
40	Garnet-gneiss (migmatites)	727 ˚C, 5.2 kbar (TD)	~140			(Bader et al., 2013)
41	Garnet-gneiss (melanosome)	700 ˚C, 8 kbar, –680 ˚C, 10.5 kbar (TD)	~88–65			(Bader et al., 2013)
42	Garnet-gneiss (melanosome)	773 ˚C, 5.1 kbar (TD)	~150			(Bader et al., 2013)
Danfeng-Songshugou Group						
1	Arc-volcanic amphibolite facies, sheared amphibolite			$^{40}Ar/^{39}Ar$ amphibole 426 ± 2, Rb–Sr mineral isochron 411 ± 5	'Late Silurian metamorphic event' for Danfeng/NQB	(Sun et al., 2002a)
2	Amphibolite			$^{40}Ar/^{39}Ar$ 420 ± 30	Retrograde metamorphism	(Ratschbacher et al., 2003)
3	Rodingite	710 ˚C, 10.5 kbar–675 ˚C, 10 kbar (TD)	~68			(Bader et al., 2013)
4	Greenschist (tuffitic protolith)			Zircon 499.4 ± 9.3	Neoproterozoic inheritance	(Bader et al., 2013)
5	Garnet-amphibolite			Titanite 324 ± 12		(Bader et al., 2013)
6	Garnet-gneiss (melanosome)	702 ˚C, 6.8 kbar (TD)	~103	Monazite 458 ± 6.8	Minor age group at 342 Ma interpreted as age of deformation (resetting)	(Bader et al., 2013)
7	Garnet-amphibolite	498 ˚C, 22.5 kbar–530 ˚C, 25.4 kbar–680	~22, 21, 60, 90, 88			(Bader et al., 2013)

		˚C, 11.5 kbar–680 ˚C, 7.5 kbar–615 ˚C, 7 kbar (TD)				
8	Rodingite	680 ˚C, 7.5 kbar–615 ˚C, 7 kbar (TD)	~90, 88			(Bader et al., 2013)
9	Garnet-pyroxenite			Zircon 501 ± 10	'HP-Granulite facies' metamorphism, subduction	(Su et al., 2004)
10	Basic granulite	828–887 ˚C, 14-15.8 kbar, 795–825 ˚C, 10.3–11.4 kbar (CTB)		Zircon 485 ± 3	Peak metamorphism	(Chen et al., 2004)
11	Garnet amphibolite			Zircon 500 ± 10, 506 ± 7	Peak metamorphism	(Liu et al., 2010)
12	Basic and felsic granulite			Zircon 504 ± 7, 506 ± 3	Peak metamorphism	(Zhang et al., 2007)
13	Garnet amphibolite			Zircon 484 ± 4, 418 ± 5	Peak and retrograde metamorphism, respectively	(Li et al., 2012)
14	Felsic granulite			Zircon 497 ± 8 (peak), 448 ± 4, 421 ± 2 (retrograde)	Peak and retrograde metamorphism	(Liu et al., 2013)
15	Garnet amphibolite			Zircon 496 ± 9	Peak metamorphism	(Qian et al., 2013)
16	Felsic gneiss			Titanite 413 ± 20	Retrograde metamorphism	(Li et al., 2014)
17	Garnet amphibolite	750–850 ˚C, 15-19 kbar (TC)	~50–45	Zircon 515 ± 12	Ophiolite emplacement age	(Tang et al., 2016)

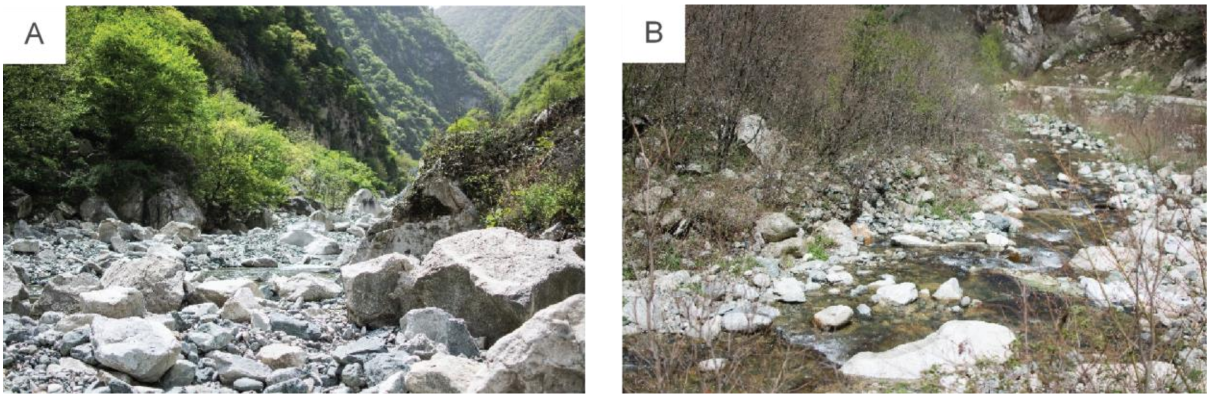

Figure 3: Representative streams of sample locations (A) Representative photograph of river sample locations 1a and 1b in Fig. 1c. (B) Representative photograph of sample location 2 in Fig. 1. Angular to sub-rounded off-white boulders are granitic erosional material. Granitic material forms ≥99% of the bedload in streams visited in the Qinling Mountains.

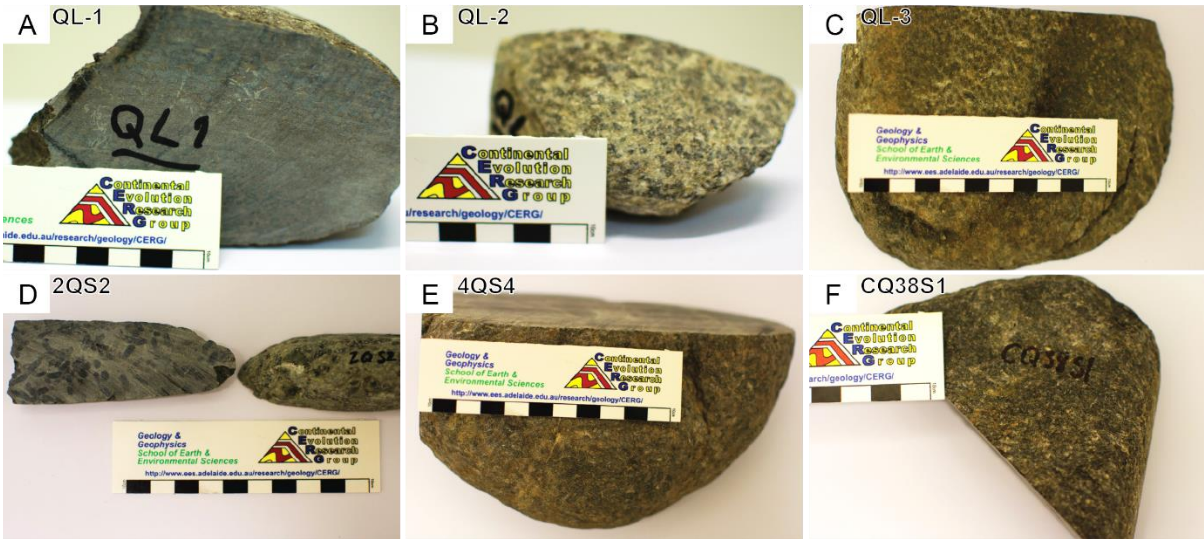

Figure 4: Hand-samples of schists collected from locations in Fig. 1c. Samples QL-1, QL-2, QL-3, 2QS2 and 4QS4 were collected in the river at locations 1a and 1b (see also Table 2). Sample CQ38S1 was collected in the river at location 2 (Table 2). In hand sample, schists are characterized by a micaceous foliation with homogenously distributed spots of dark bluish-grey spots of cordierite (up to 0.5 cm). CQ38S1 is a cordierite absent garnet–staurolite schist, also defined by a micaceous foliation with garnets clearly visible on fresh surface, up 0.2 cm in diameter. The location coordinates, sample dimensions and mineralogy are detailed in Table 2.

Table 2: Summary of samples collected, rock description and collection locality (WGS84 datum, latitude and longitude presented in degrees, minutes and seconds).

Sample	Rock type	Dimensions (~L x W cm)	Location number (Fig. 1c)	Geological setting	Coordinates
QL-1	cd-bi schist	~15 x 12.5	1a	Southern NQB	~33°55'50.13"N ~108° 8'54.87"E
QL-2	cd-bi schist	~25 x 15	1a	Southern NQB	~33°55'50.13"N ~108° 8'54.87"E
QL-3	cd-bi-chl schist	~20 x 13	1a	Southern NQB	~33°55'50.13"N ~108° 8'54.87"E
2QS2	cd-and schist	~12 x 8	1b	Southern NQB	33°55'12.17"N 108° 9'9.71"E
4QS4	cd-and schist	~20 x 15	1b	Southern NQB	33°54'52.40"N 108° 9'10.77"E
CQ38S1	g-st schist	~15 x 12	2	Central NQB	33°56'14.00"N 109° 7'31.00"E

Sample petrography

In the following descriptions, the logic that peak minerals are coarser grained and/or define a fabric and that retrograde minerals define either no fabric or are aligned at an angle to the main fabric is applied. Petrography and photomicrographs for samples QL-2, QL3, 2QS2 and 4QS4 are provided in Appendix A because these samples were not used to constrain *P–T* conditions. The modal abundance (‘mode’) of minerals in each sample are provided in Table 3 because these data are used to constrain *P–T* conditions.

QL-1

Matrix minerals consist of biotite (50–300 μm), quartz (50–200 μm) and plagioclase (< 100 μm) that are distributed evenly throughout (Fig. 5a, b). Biotite defines a pervasive foliation that encloses cordierite. Poikiloblastic cordierite (300–1400 μm) contains abundant inclusions of matrix minerals, but is completely pinitised. Inclusions in cordierite are generally finer grained (≤ 100 μm) than matrix grains. Inclusions define a fabric that is both parallel and misaligned. Accessory minerals include rutile, zircon, monazite and tourmaline. The interpreted peak assemblage is cordierite + biotite + quartz + plagioclase + rutile.

CQ38S1

The matrix consists of biotite (≤ 100 μm), muscovite (≤ 100 μm), quartz (≤ 300 μm), plagioclase (≤ 50 μm) and ilmenite (≤ 20 μm). The dominant fabric of the sample is defined by biotite, muscovite and quartz. S_1 and S_2 fabrics are observed throughout (Fig. 5c,d). Porphyroblasts of garnet (100–700 μm) and staurolite (100–200 μm) are typically separated and the fabric defined by matrix minerals wraps around them. Garnet contains inclusions of quartz, biotite and ilmenite. Staurolite has numerous inclusions of ilmenite. Garnet grains are commonly fractured with fine grained (< 20 μm) muscovite and biotite occurring in the cracks. The interpreted peak assemblage is garnet + staurolite + biotite + plagioclase + muscovite + quartz + ilmenite. Sparse amounts of interpreted retrograde chlorite occur on the margins of garnet.

Table 3: Summary of mineral modal proportions for each sample. Mineral abbreviations used throughout this study include; g (garnet), st (staurolite), cd (cordierite), and (andalusite), chl (chlorite), bi (biotite), mu (muscovite), ab (albite), pl (plagioclase), ru (rutile), ilm (ilmenite), q (quartz), tm (tourmaline). Totals for modal proportion do not equal 100% because Fe-Ti oxides including accessory phases zircon, monazite, tourmaline and apatite do not form part of the estimation. These minerals collectively occur in modal proportions <2%. Samples QL-2, QL-3, 2QS2 and 4QS4 are in Appendix A, abbreviated to ‘Ap. A’ for the relevant sample.

Sample					**Modal proportion**					
	g	st	cd	and	bi	chl	mu	pl	q	**Total**
QL-1	-	-	23%	-	32%	-	-	30%	12%	97%
QL-2 Ap. A	-	-	28%	-	25%	-	5%	10%	30%	98%
QL-3 Ap. A	-	-	15%	-	20%	5%	15%	10%	32%	97%
2QS2 Ap. A	-	-	23%	5%	20%	5%	5%	15%	25%	98%
4QS4 Ap. A	-	-	25%	10%	15%	-	5%	10%	34%	99%
CQ38S1	5%	1%	-	-	40%	<1%	17%	10%	25%	99%

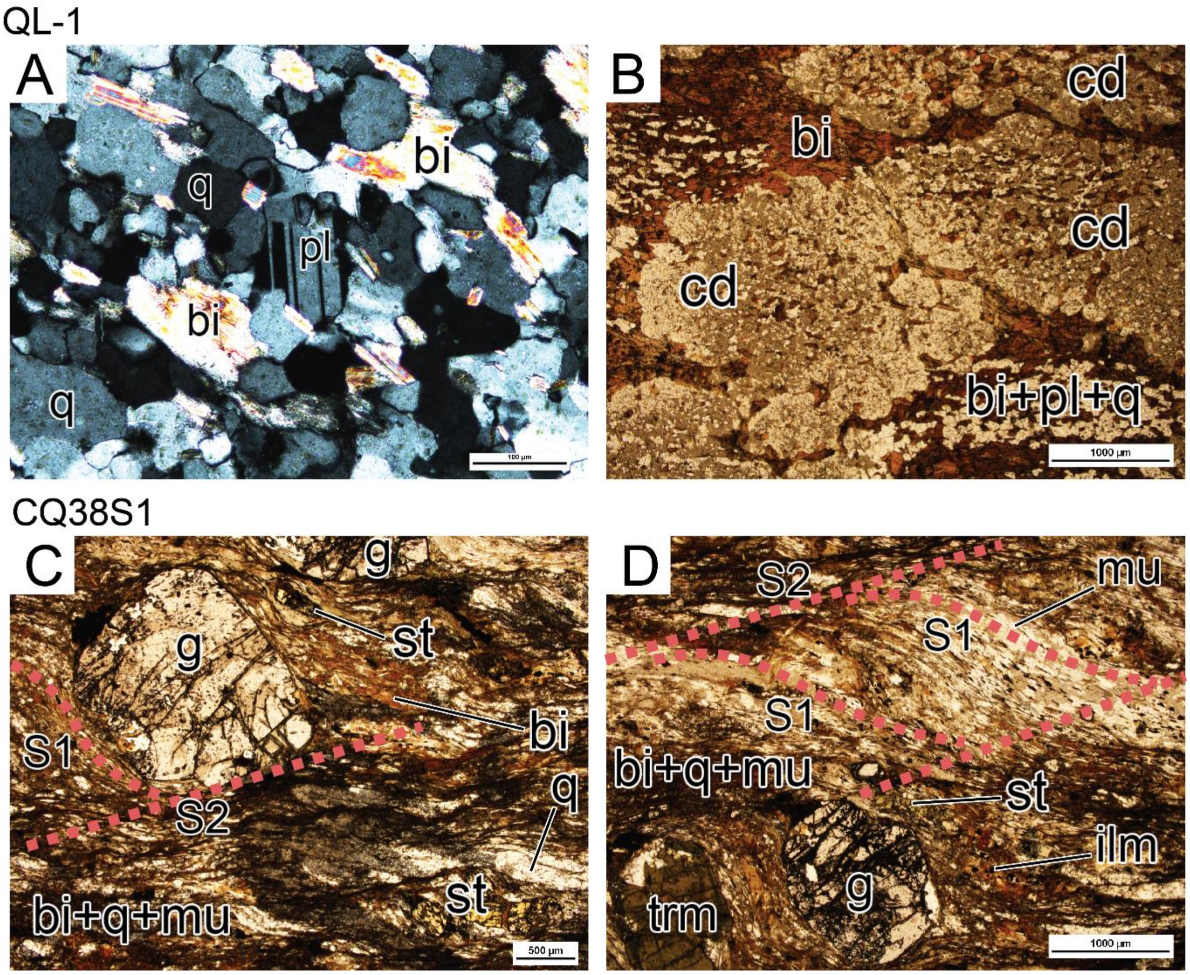

Figure 5: Photomicrographs of samples used in this study: (A) Image: fine-grained plagioclase in the matrix; (B) Cordierite porphyroblasts surrounded by a matrix consisting of biotite + quartz + plagioclase + rutile which also commonly occur as inclusions in cordierite. Biotite clearly wraps around cordierite; (C) S_1/S_2 fabric defined by biotite + muscovite + quartz, wrapping around garnet. Staurolite is separated from garnet by matrix grains; (D) S_1/S_2 fabric wrapping around garnet. Accessory tourmaline grain separated from garnet by matrix. S_1/S_2 fabric is mainly defined by muscovite. Staurolite is separated from garnet by matrix grains. Staurolite is finer-grained compared to garnet.

ANALYTICAL METHODS

Geochronology

To establish the provenance of schist boulders and age of metamorphism, three complementary geochronological methods were applied. U–Pb zircon ages were acquired from QL-3 in the 79–400 μm fraction, and in the < 79 μm fraction for samples 2QS2, 4QS4 and CQ38S1 by laser ablation-inductively coupled plasma-mass spectrometry (LA–ICP–

MS). In-situ U–Pb monazite ages were acquired from samples QL-1, QL-2 and QL-3 as well as epoxy-resin mounted monazite in CQ38S1 (< 79 µm fraction) by LA–ICP–MS. Sample preparation and operational procedures for these techniques are detailed in Appendix L.

Phase equilibria forward modelling

Phase equilibria calculations were performed using the software program THERMOCALC (Powell & Holland, 1988; Holland & Powell, 2011) in the model chemical system MnO–Na_2O–CaO–K_2O–FeO–MgO–Al_2O_3–SiO_2–H_2O–TiO_2–O (MnNCKFMASHTO), where 'O' is a proxy for Fe_2O_3, using the latest internally-consistent thermodynamic dataset 'ds6' (filename tc-dsc62.txt; Holland & Powell, 2011) and activity–composition models (Powell et al., 2014; White et al., 2014a; White et al., 2014b). Calculations in THERMOCALC are based on the user specifying the stable assemblage and calculating all the field boundaries and intersection points in turn. The initial stable assemblage is determined by performing a Gibbs energy minimisation calculation at a set pressure–temperature (*P–T*) condition. The diagram is built up and around from that initial assemblage and involves many trial and error calculations in order to determine which phases appear or disappear as a function of pressure, temperature and/or composition. Therefore, a single diagram commonly comprises >150–200 total line and point calculations, and the user is intellectually involved in the calculations at every step along the way. This amounts to several weeks of calculation per diagram. The most uncertain compositional variables are Fe_2O_3 and H_2O, commonly requiring that these be constrained with *T–M* type diagrams (where *M* refers to amount of an oxide component) prior to the calculation of the *P–T* pseudosection. In this study of un-melted rocks, H_2O is assumed to be present in saturating amounts for all calculations, negating the need for T–M_{H2O} diagrams. The choice of pressure at which to calculate the *T–M* diagrams is based on broadly estimating the pressure at which the observed peak metamorphic assemblage is stable.

Contouring of phase equilibria models for the normalised abundances (‘mode’) of phases was calculated using the Matlab-based, automated software TCInvestigator v1.0 (Pearce et al., 2015). Input to TCI requires THERMOCALC input files and executable (.exe) files as well as the finished *P–T* model from THERMOCALC.

RESULTS

Geochronology

Zircon was analysed to constrain the age of schist protolith (Fig. 6–9) whereas monazite was analysed to constrain the age of metamorphism (Fig. 10–13).

ZIRCON U–PB LA–ICP–MS GEOCHRONOLOGY

Sample QL-3

One-hundred and thirty-nine analyses were collected from 121 zircon grains. Twenty-four were excluded from age calculations (< 90% concordance and > 105% concordance). All zircons show internal structure (oscillatory zoning). Commonly, oscillatory zoning is truncated by another generation of oscillatory zoning as shown in Fig 6. Twenty-six analyses forming the youngest age peak at ca. 431 Ma range between 411–495 Ma. Five analyses range between 544–653 Ma. Fifty-three analyses range between 705–892 Ma. Ten analyses are between 910–944 Ma. Fourteen analyses are between 1070–1886 Ma. Eight analyses are between 2034 and 2617 Ma.

Sample 2QS2

This sample provided a relatively low yield of small (< 30 μm) zircon. Fourty-five analyses were obtained on 45 individual grains. Of the forty-five analyses, seventeen were rejected (< 90% concordance and > 105% concordance). Typically zircon morphology is rounded with 1.5:1 dimensions. Minor age peaks occur at <600 Ma, two analyses have ages of 356 Ma and

395 Ma and four analyses range between 413–541 Ma. Nine analyses range between 621–984 Ma. Nine analyses range between 1000–1810 Ma. Four analyses range between 2290–2790 Ma. Dominant peaks occur at ca. 400–500, ca. 808–1130, ca. 1630 and ca. 2280–2790 Ma.

Sample 4QS4

This sample provided a relatively low yield of small (< 30 μm) zircon. Thirty-five analyses were obtained on 35 individual grains. Of the thirty-five analyses, ten were rejected (< 90% concordance and > 105% concordance). Zircons in this sample have well rounded grain boundaries with common examples of zircon with 2:1 dimension in their morphology. Major peaks occur between 400–500 Ma, 900–1000 Ma and minor peaks at ca. 1600 and ca. 2700 Ma. The distribution of data is; seven grains range between 298–343 Ma. Four analyses between 437–531 Ma. Thirteen analyses between 706–1220 Ma and single grain analyses at 1680 Ma and 2703 Ma.

Sample CQ38S1

One-hundred and thirty-five analyses were collected from 135 individual zircon grains. Of those analyses, twenty-seven were excluded from age calculations (< 90% concordance and > 105% concordance). Zircons in this dataset were ablated without identification of complex internal structures due to their size (< 30 μm). To avoid potential bias, every identifiable zircon mounted was analysed. The data predominantly concentrates between c. 400 Ma and 600 Ma (Fig. 9d). From the probability density plot (Fig. 9a) there are four approximate age ranges 375–390 Ma, 403–608 Ma, 666.9–722 Ma and 837–920 Ma. Fifteen data points (13.8% of dataset) occur between 296–399 Ma. Twenty-two data points occur between 400-420 Ma. The remaining 71 data points are distributed as ages > ca. 420 Ma.

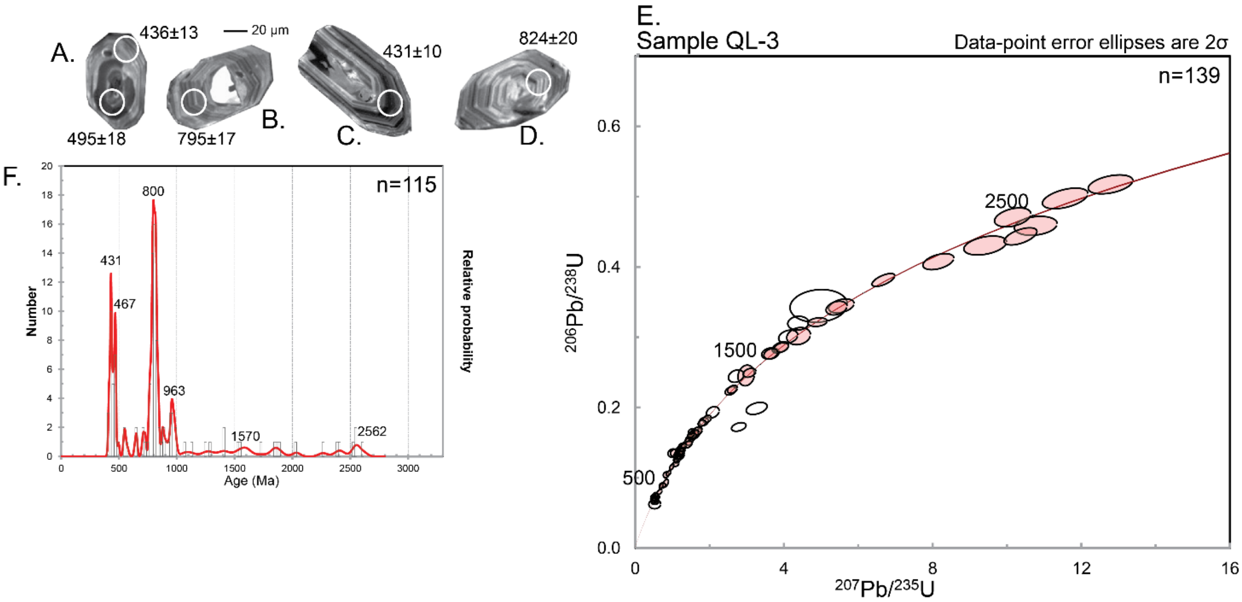

Figure 6: Zircon U–Pb geochronological data for sample QL-3: (A) Zircon with distinct older core and younger oscillatory overgrowth; (B) Older, oscillatory zoned zircon grain with bright CL core; (C) Lighter and darker oscillatory internal structures in zircon; (D) Zircon with oscillatory zoning internal structure; (E) Wetherill concordia plot corresponding to data presented in 'F'. White ellipses are excluded from age determinations due to discordancy (< 90% or > 105%); (F) Relative probability density plot for concordant (90–105%) zircon grains in sample QL-3. Major peaks are labelled (Ma).

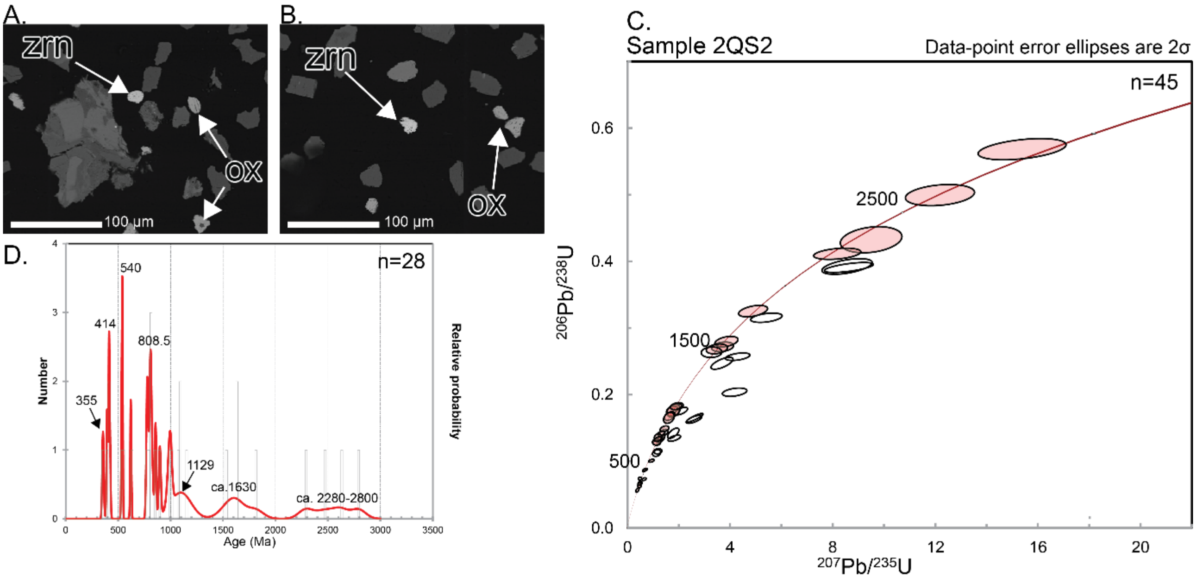

Figure 7: Zircon U–Pb geochronology for sample 2QS2: (A) BSE images of identifiable zircon grains occurring in the < 79 µm fraction. Zircon grains appear rounded to sub-rounded; (B) BSE image of another zircon which is brighter than other mineral grains (Fe–Ti oxide, silicates) forming part of the < 79 µm separate; (C) Wetherill concordia plot corresponding to data presented in 'D'. White ellipses are excluded from age determinations due to discordancy (< 90% or > 105%); (D) Relative probability density plot for concordant (90–105%) zircon grains in sample 2QS2. Major peaks are labelled (Ma).

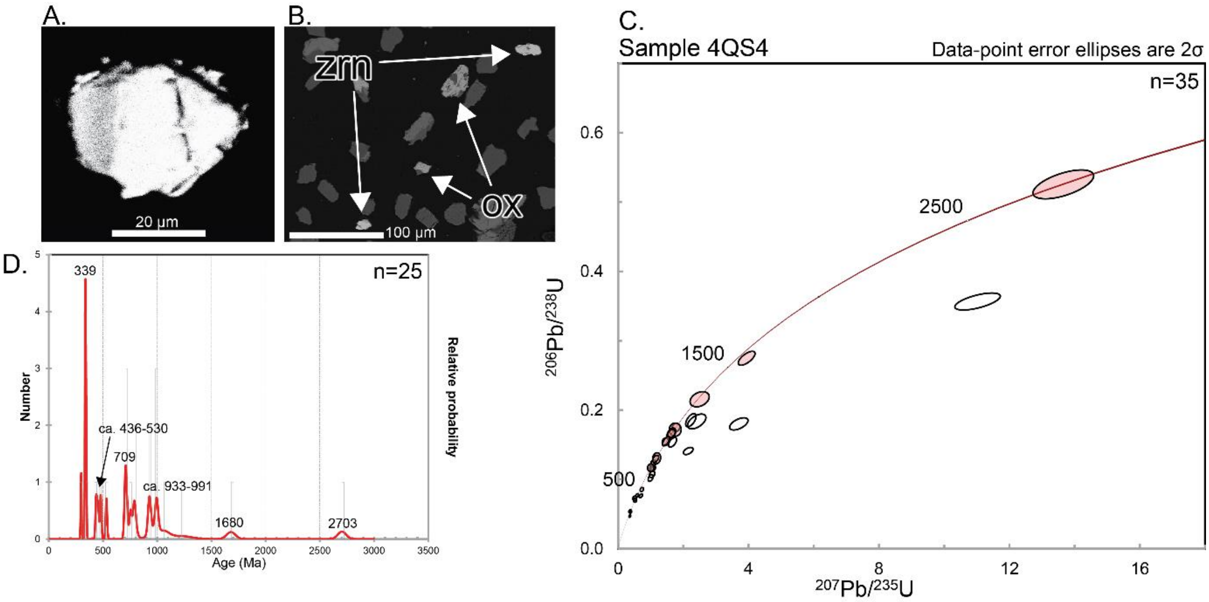

Figure 8: Zircon U–Pb geochronology for sample 4QS4 (A) CL image of a < 30 µm zircon grain, complex internal structure is un-identifiable; (B) BSE image of zircon grains identified in the grain mount with adjacent oxide grains appearing less bright; (C) Wetherill concordia plot corresponding to data presented in 'D'. White ellipses are excluded from age determinations due to discordancy (< 90% or > 105%); (D) Relative probability density plot for concordant (90–105%) zircon grains in sample 4QS4. Major peaks are labelled (Ma).

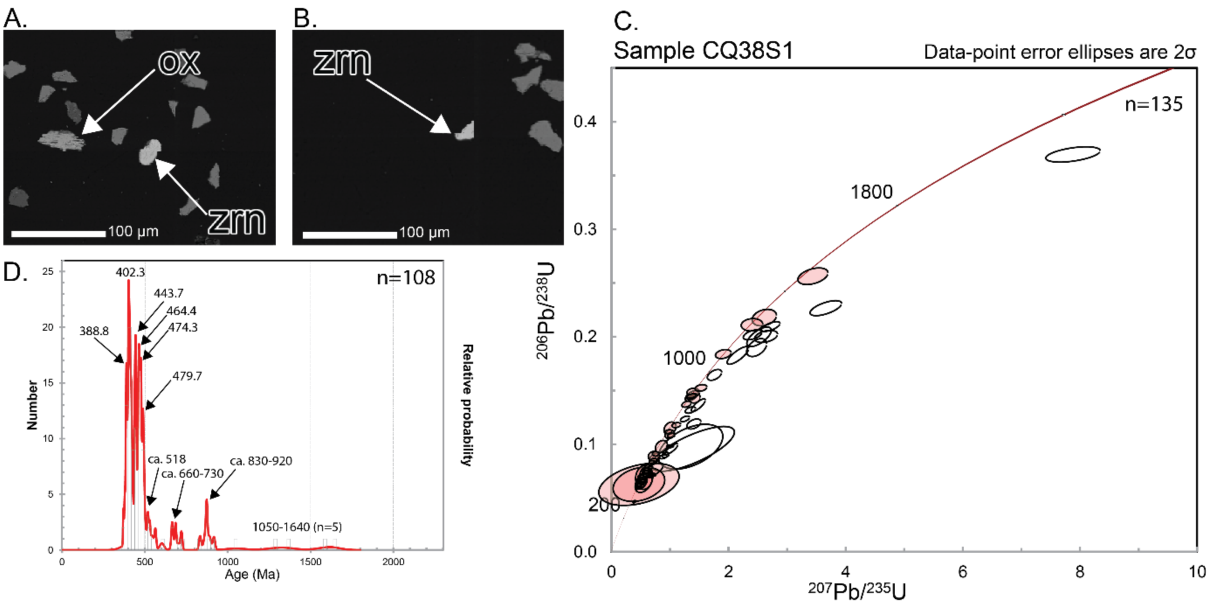

Figure 9: Zircon U–Pb geochronology for sample CQ38S1: (A) BSE image of a larger zircon grain identified in the epoxy mount of < 79 µm. Zircon grains are brighter than Fe–Ti oxides and silicate grains; (B) BSE image of an angular zircon grain; (C) Corresponding Wetherill concordia plot to data presented in 'D'. White ellipses are excluded from age determinations due to discordancy (< 90% or > 105%); (D) Relative probability density plot for concordant (90–105%) zircon grains for sample CQ38S1. Major peaks are labelled (Ma).

MONAZITE U–PB LA–ICP–MS GEOCHRONOLOGY

Sample QL-1

Forty-two analyses were collected from 42 individual in-situ monazite grains. Of the forty-two analyses, two were rejected on the basis of their $^{206}Pb/^{238}U$ error (> 1) and an additional four on the basis of their particularly low concordance values (< 30%). The remaining data define a lower intercept age of 219 ± 13 Ma *(n = 42*, MSWD = 2.0) and a concordia age of 222.9 ± 2.9 Ma *(n = 8*, MSWD = 10.2). A linear probability diagram for analyses that define the concordia age shows the spread of $^{206}Pb/^{238}U$ ages (i.e. between 213–216.8 Ma).

Sample QL-2

Forty-eight analyses were collected from 48 individual in-situ monazite grains. Of the forty-eight analyses, eleven were rejected on the basis of their negative error correlation value, and an additional two due to their significant deviation from the dominant spread (monazite grains 55 and 36). The remaining data is heavily discordant, defining a lower intercept age of 214 ± 7.6 Ma *(n = 37*, MSWD = 3.4) and an upper intercept that approximates the age of Earth.

Sample QL-3

Forty-nine analyses were collected from 49 individual in-situ monazite grains. Of the forty-nine, six were rejected due negative error correlation values, and an additional six on the basis of their large $^{207}Pb/^{235}U$ error (> 0.5–1). The remaining data define a lower intercept age of 221.8 ± 3.6 Ma (*n = 37*, MSWD = 1.3) and a concordia age of 228.9 ± 4.5 Ma (*n = 9*, MSWD = 2.9). A linear probability diagram for analyses that define the concordia age shows the spread of $^{206}Pb/^{238}U$ ages (i.e. between 214–239 Ma).

Sample CQ38S1

Seventy-nine analyses were collected from 79 individual epoxy resin-mounted monazite grains. Of the seventy-nine, twenty analyses were excluded from age calculations (> 10% discordance) and one was rejected on the basis of a negative error correlation value. The remaining data (50%) defines a concordia age of 405.0 ± 1.5 Ma (*n* = *40*, MSWD = 7.3). A linear probability plot for analyses used to define the concordia age shows the spread of $^{206}Pb/^{238}U$ ages. The spread of this data defines approximately two groups occurring between 388.6–404.6 Ma and 407.4–412.8 Ma. Concordant data that was excluded from the preceding age calculations is shown in Fig. 13 forming a spread between 387.6 and 330.8 Ma (21% of data).

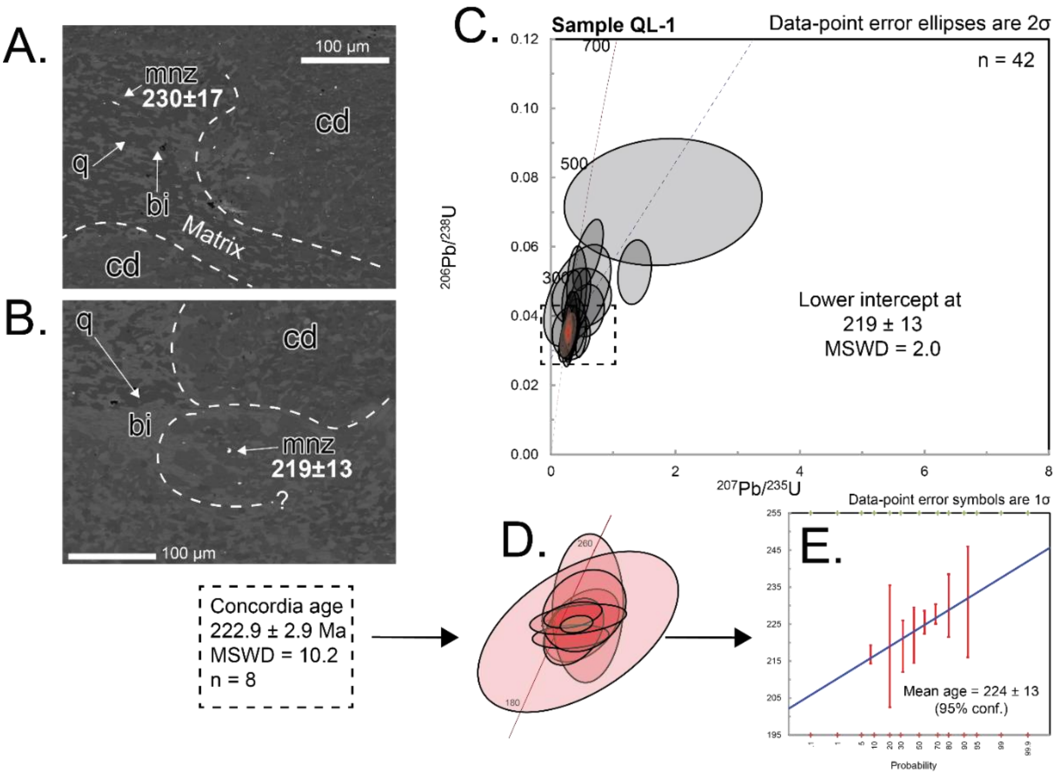

Figure 10: U–Pb geochronology for in situ monazite from sample QL-1: (A) Backscattered electron image showing the microstructural location of monazite with the corresponding concordant age of 230 ± 17 Ma; (B) BSE image showing the microstructural location of monazite, aged 219 ± 13 Ma; (C) Wetherill concordia plot for all data. Grey coloured ellipses were used for an intercept age (219 ± 13 Ma, MSWD = 2.0, n = 42), red ellipses were used to obtain a concordia age calculation (222.9 ± 2.9, MSWD = 10.2, n = 8); (D) A close-up of the data forming a concordia age on the basis of overlapping ellipses; (E) A linearised probability diagram showing the distribution of concordant monazite grains forming the concordia age.

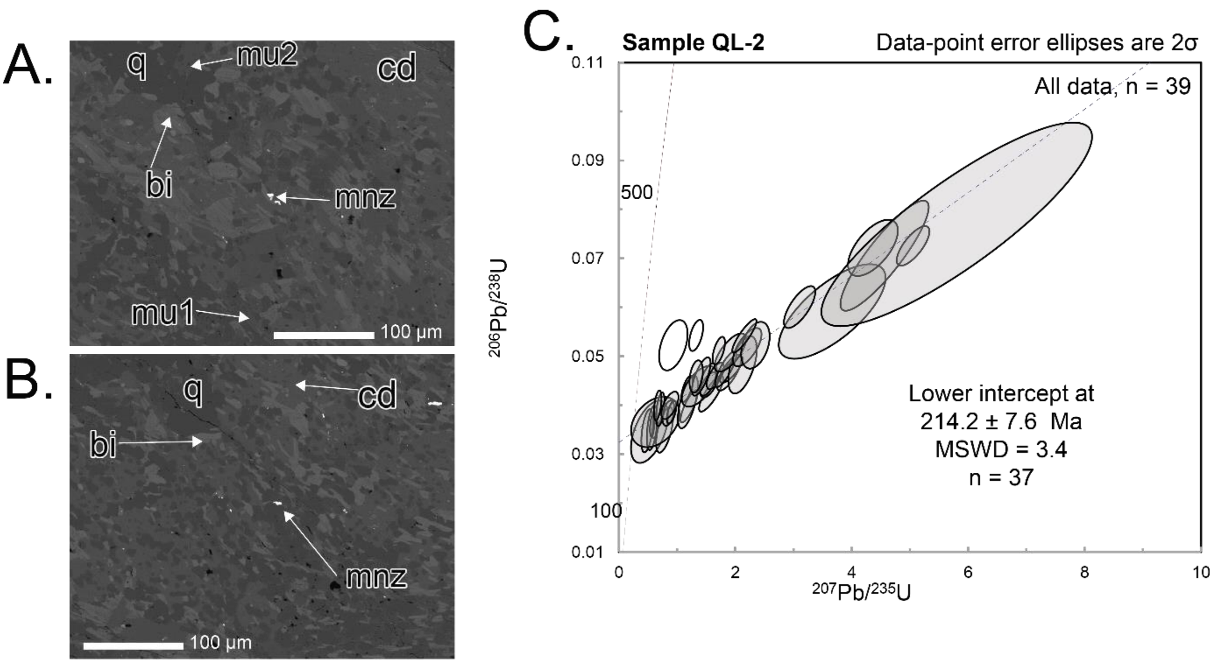

Figure 11: (above) U–Pb geochronology for in situ monazite from sample QL-2: (A) Backscattered electron image showing the microstructural location of monazite in contact with matrix biotite and quartz; (B) Backscattered electron image showing the microstructural location of monazite surrounded by quartz in the matrix; (C) Wetherill concordia diagram for all data (n = 39). White ellipses were not used for the purpose of calculating the lower intercept age of 214.2 ± 7.6 Ma, MSWD = 3.4 (n = 37). The upper intercept defines an age of 4974 ± 93 Ma (effectually age of Earth).

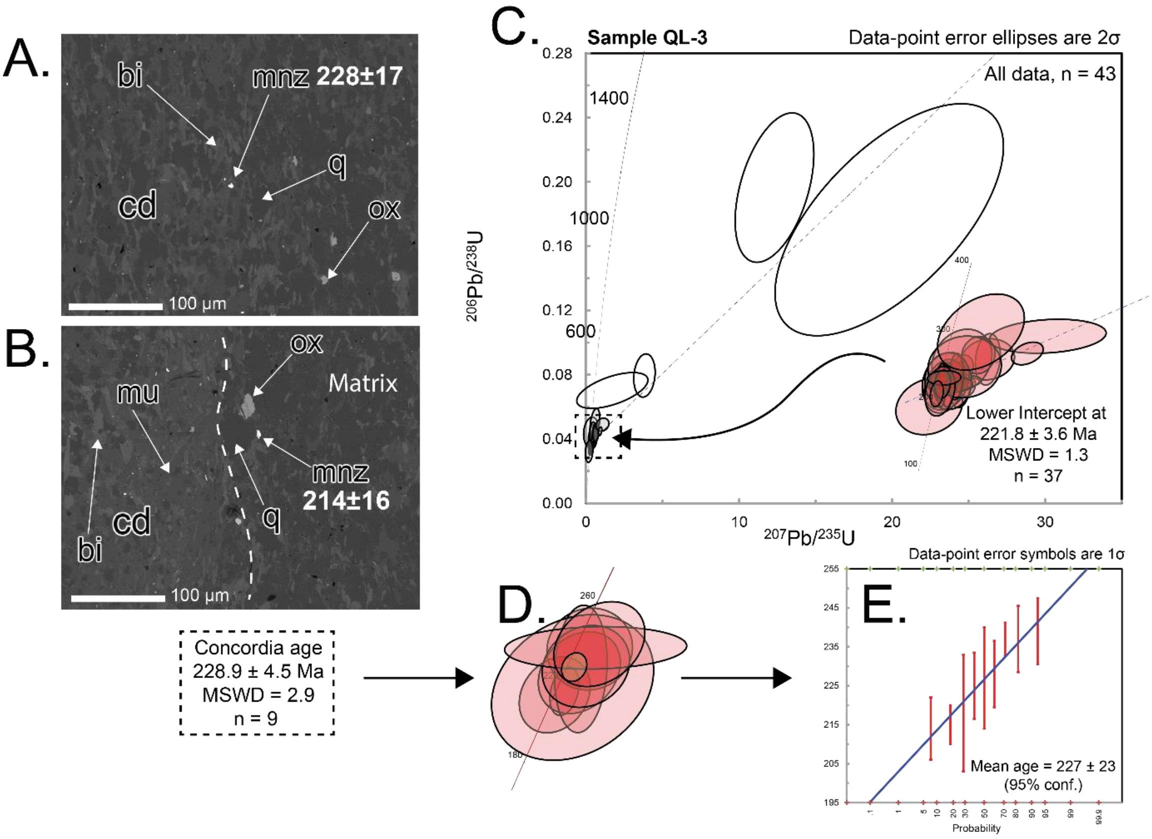

Figure 12: U–Pb geochronology for in situ monazite from sample QL-3: (A) Backscattered electron image of monazite with the corresponding concordant spot age of 228 ± 17 Ma; (B) Backscattered electron image of in-situ monazite aged 214 ± 16 Ma; (C) Wetherill concordia plot showing all data (n = 43), white ellipses are excluded data. Grey (too small to see, identified by arrow) ellipses are data used to define an intercept age (also shown as red, right) at 221.8 ± 3.6 Ma (MSWD = 1.3, n = 37); (D) Subset of data which define a concordia age calculation of 228.9 ± 4.5 Ma (MSWD = 2.9, n = 9); (E) Linearised probability diagram of data showing the distribution of concordant monazite grains defining the concordia age.

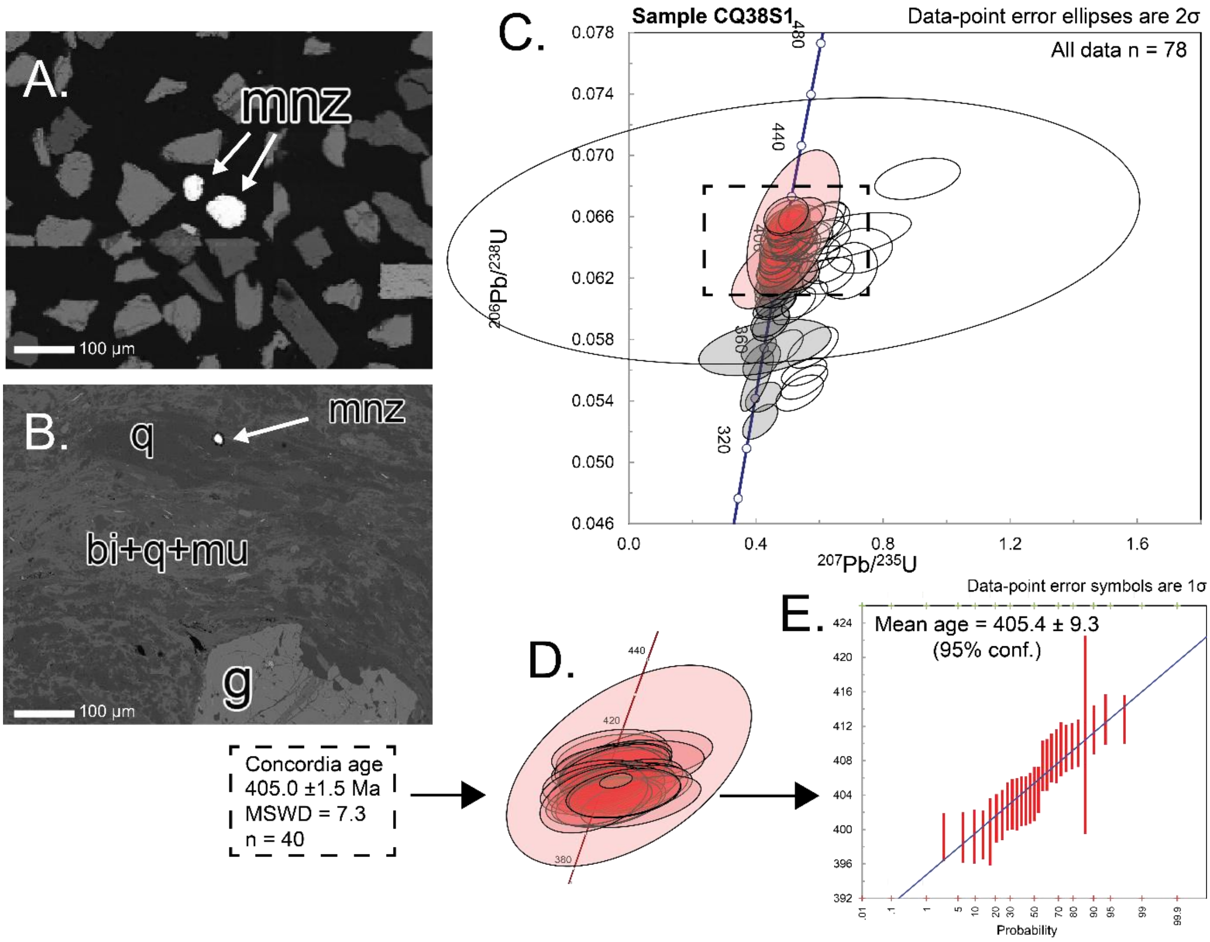

Figure 13: U–Pb geochronology for grain mounted monazite from sample CQ38S1; (A) Backscattered electron image of bright monazite in epoxy resin-mount, surrounded by matrix-type minerals in the < 79 µm fraction; (B) Backscattered electron image showing the in-situ microstructural location of in-situ monazite in the matrix. The size of the in-situ monazite is significantly smaller than that which was separated from the sample. Therefore,—in-situ monazite was not analysed in this sample due to its small size; (C) Wetherill concordia plot of all data, white ellipses are excluded from age determinations due to discordancy (< 90% or > 105%), red ellipses define a concordia age. Grey ellipses are concordant (90–105%) and define a spread to younger ages approaching ca. 320 Ma; (D) Close-up of data defining a concordia age calculation of 405.0 ± 1.5 Ma (MSWD = 7.3, n = 40), 66.6% of concordant data defines a concordia age; (E) Linearised probability plot, showing the spread of data that define the concordia age. Two distinct groups are identified between ca. 411–408 Ma, and ca. 404–400 Ma.

Phase equilibria forward modelling: *T–M_O* and *P–T*

Temperature–Molar oxidation (*T–M_O*) and pressure–temperature (*P–T*) pseudosections were calculated for samples QL-1 and CQ38S1. The objective of the phase equilibria modelling was to constrain *P–T* conditions for two metapelitic samples, thus developing the thermal framework for their metamorphic evolution.

The principle uncertainty in pseudosection modelling relates to the determination of effective composition, particularly in this study Fe_2O_3 (e.g. Kelsey & Hand, 2015). The appropriate oxidation state, or Fe_2O_3 (as 'O') vs FeO amount for *P-T* pseudosections was constrained for each sample by first calculating *T–M_O* pseudosections. In each *T–M_O* section the oxidation state along the M axis varies from 100% FeO to 99% Fe_2O_3, 1% FeO at $M = 1$. A fixed pressure is required to calculate the *T–M_O* sections. For modelling QL-1 this pressure was 3 kbar and for CQ38S1 this pressure was 5 kbar, based on independent published information (e.g. White et al., 2014a; White et al., 2014b).

Sample QL-1

The calculated *T–M_O* pseudosection for QL-1 is shown in Fig. 14 and the pseudosection contoured for the modes of phases is shown in Fig. 15. The peak assemblage for sample QL-1 is interpreted to be cordierite + biotite + plagioclase + rutile + quartz, shown as a field bound by a bold outline in Fig. 14.

The chosen oxidation state corresponds to the composition at $M = 0.02$ on the basis that modal proportions estimated in Table 3 coincide with the calculated modes of phases in Fig. 15.

The calculated *P–T* pseudosection shows that the peak assemblage field occurs in a narrow area over a large *P–T* range 0.5–4.4 kbar and 530–675 ˚C (Fig. 16). The area of *P–T* space that coincides with observed proportions of cordierite, biotite, plagioclase and quartz (Table 3) is between 0.6–4.25 kbar and

540–670 ˚C, as illustrated in Fig. 17f. This field is constrained by the presence of andalusite up pressure, and presence of K-feldspar down pressure.

Sample CQ38S1

The peak assemblage for CQ38S1 is interpreted to be garnet + staurolite + biotite + muscovite + plagioclase + ilmenite + quartz. Chlorite is interpreted as a retrograde mineral.

The calculated T–M_O pseudosection for CQ38S1 is shown in Fig. 18. The mode of peak assemblage phases in CQ38S1 did not prove comparable with observations and therefore TCI outputs are not used to constrain the degree of oxidation. The chosen oxidation state corresponds to the composition at M = 0.07 and was based on the absence of rutile-bearing assemblages to higher pressures, maximising the full possible range of staurolite–ilmenite bearing assemblages up-pressure for the purpose of comparing observations to calculated modes in TC Investigator.

The peak field in the calculated *P–T* pseudosection (Fig. 19) is constrained to conditions of ~7.1 kbar and 615 ˚C (Fig. 20d). This field is bound by the presence of rutile up-pressure, occurrence of margarite down-temperature and occurrence of sillimanite (and disappearance of staurolite) up-temperature and down-pressure.

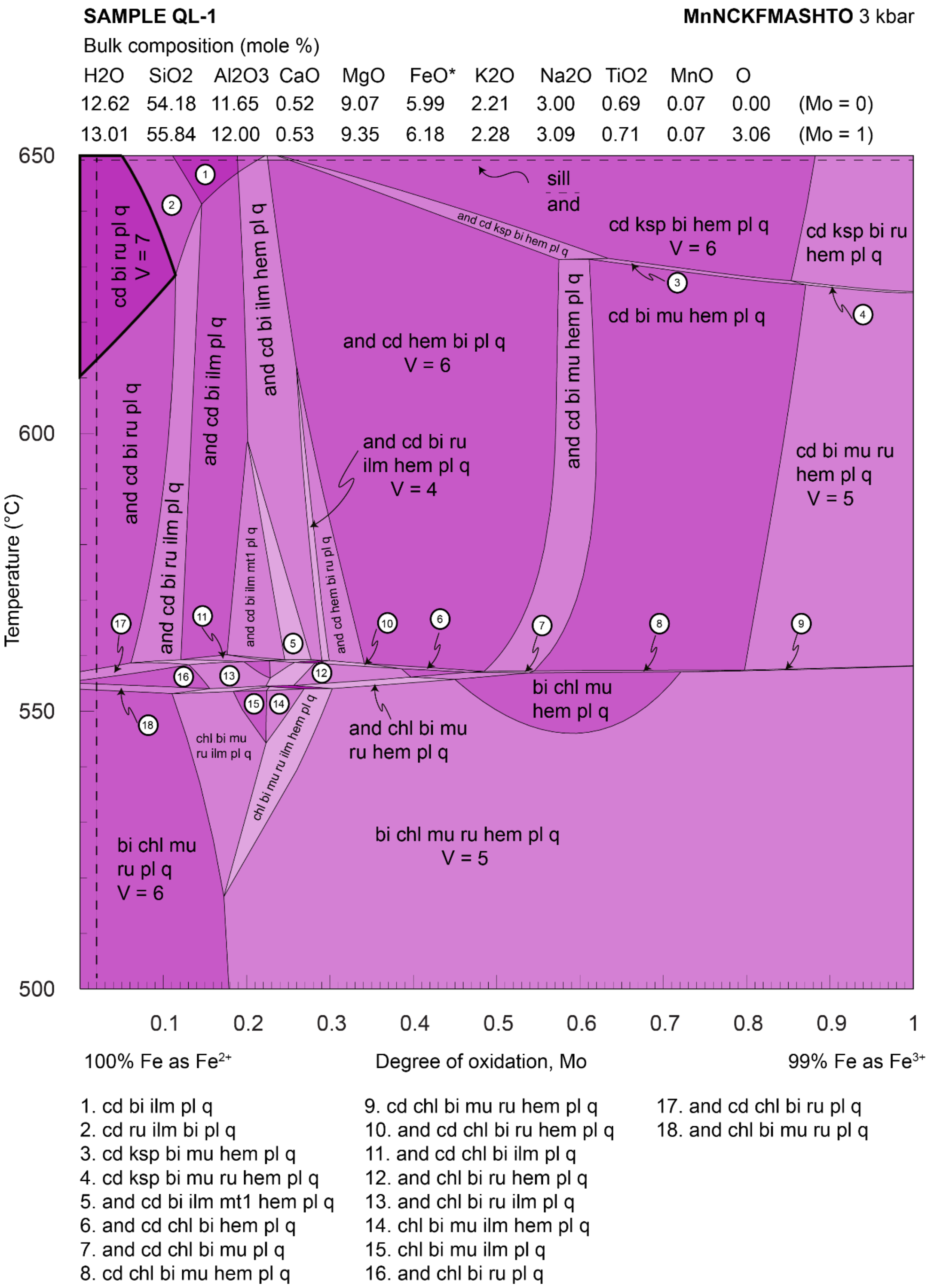

Figure 14: Calculated T–M_O pseudosection for sample QL-1. All fields in the diagram contain water, H_2O, as part of the equilibrium assemblage. Fields too small to be directly labelled are identified by numbered circles corresponding to the assemblage occurring within the field. Progressively darker tones are representative of increasing variance, V, where V = components – phases + 2 (components = 11). The compositions in mole% used to calculate the diagram, corresponding to that at M = 0 and M = 1, are provided above the diagram. FeO* = FeO + 2 × 'O'. The composition used for the calculation of the P–T pseudosection, Fig.16, is that at M_O = 0.02, depicted as a vertical dashed line. This composition passes through the interpreted peak assemblage field cordierite + biotite + rutile + plagioclase + quartz + H_2O, which occurs in the top left of the diagram (bold outline).

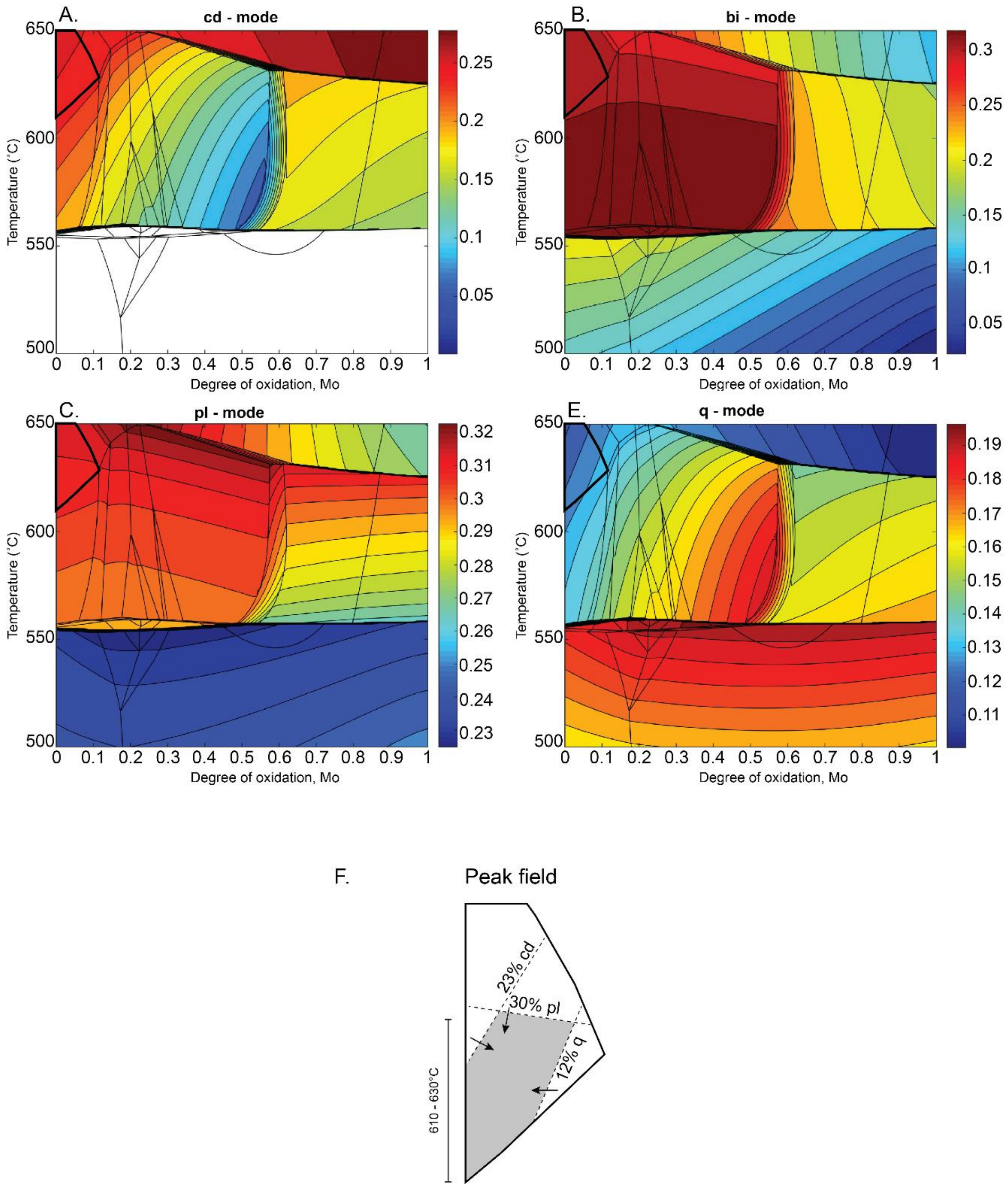

Figure 15: Calculated *T–M*T–M_O pseudosection for sample QL-1 contoured for the abundance ('mode') of some phases. The calculated abundance of phases in the peak assemblage field (at top left, bold outline, also in F) was used in conjunction with estimated abundances of minerals in the sample (Table 3) to choose an appropriate composition along the M_O axis for calculation of the *P–T* pseudosection, Fig.16. Diagram (F) shows the peak field with calculated abundances of phases (combination of A, B, C and D) with respect to estimated modal proportions in Table 3 to further constrain the oxidation state within the peak assemblage field.

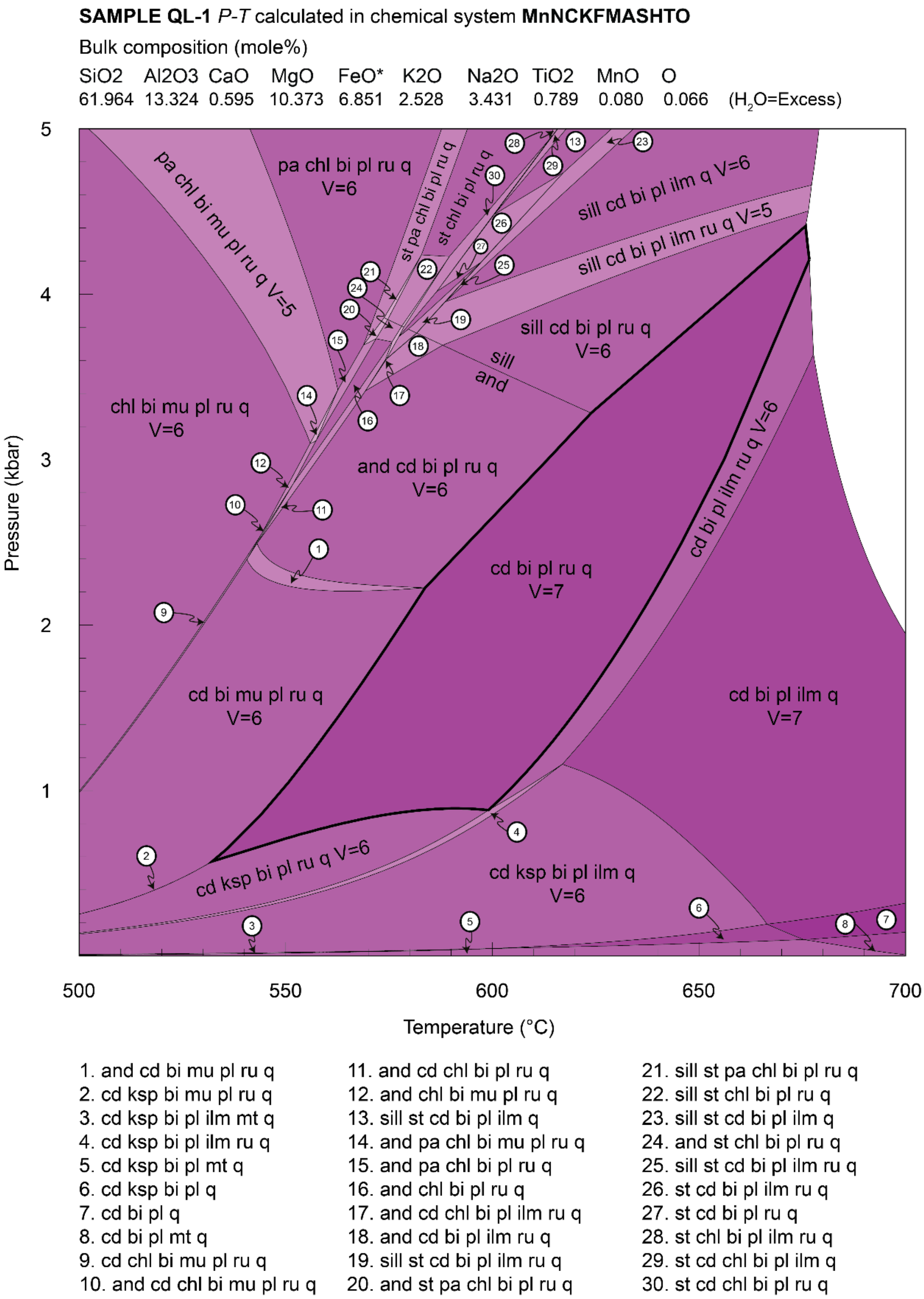

Figure 16: Calculated *P–T* pseudosection for sample QL-1. All fields in the diagram additionally contain water, H_2O, as part of the equilibrium assemblage. Fields too small to be directly labelled are identified by numbered circles corresponding to the assemblage occurring within the field. Progressively darker tones are representative of increasing variance, V, where V = compoennts - phases + 2 (components = 11). The composition in mole% used to calculate the diagram, corresponding to that at *M* = 0.02 in Fig.14, is provided above the diagram. FeO* = FeO + 2 × 'O'. The white area at top right of diagram is melt-bearing. This was not calculated as the sample is not migmatitic. The peak assemblage field cordierite + biotite + plagioclase + rutile + quartz + H_2O is outlined in bold.

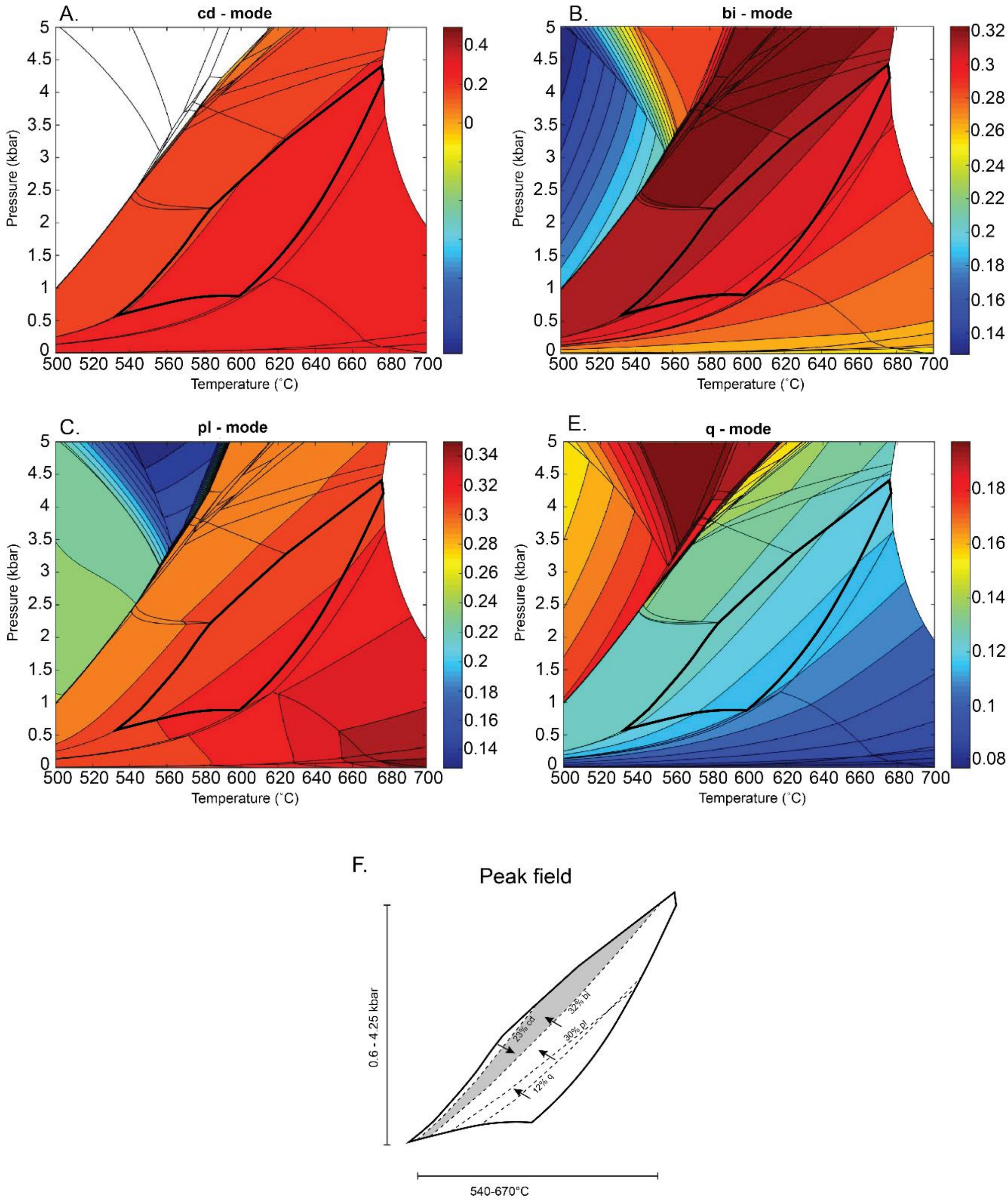

Figure 17: Calculated *P*–*T* pseudosection for sample QL-1 contoured for the abundance ('mode') minerals in the peak assemblage. The calculated abundances of phases in the peak assemblage field (outline in bold, also shown in detail in F), were used in conjunction with estimated abundances of minerals in the sample (Table 3) to constrain the peak *P*–*T* conditions experienced by the rock. Diagram (F) shows the detail of the peak assemblage with calculated abundances of phases (combination of A, B, C and D) coinciding with estimated modal proportions in Table 3 to further constrain the metamorphic conditions within the peak assemblage field.

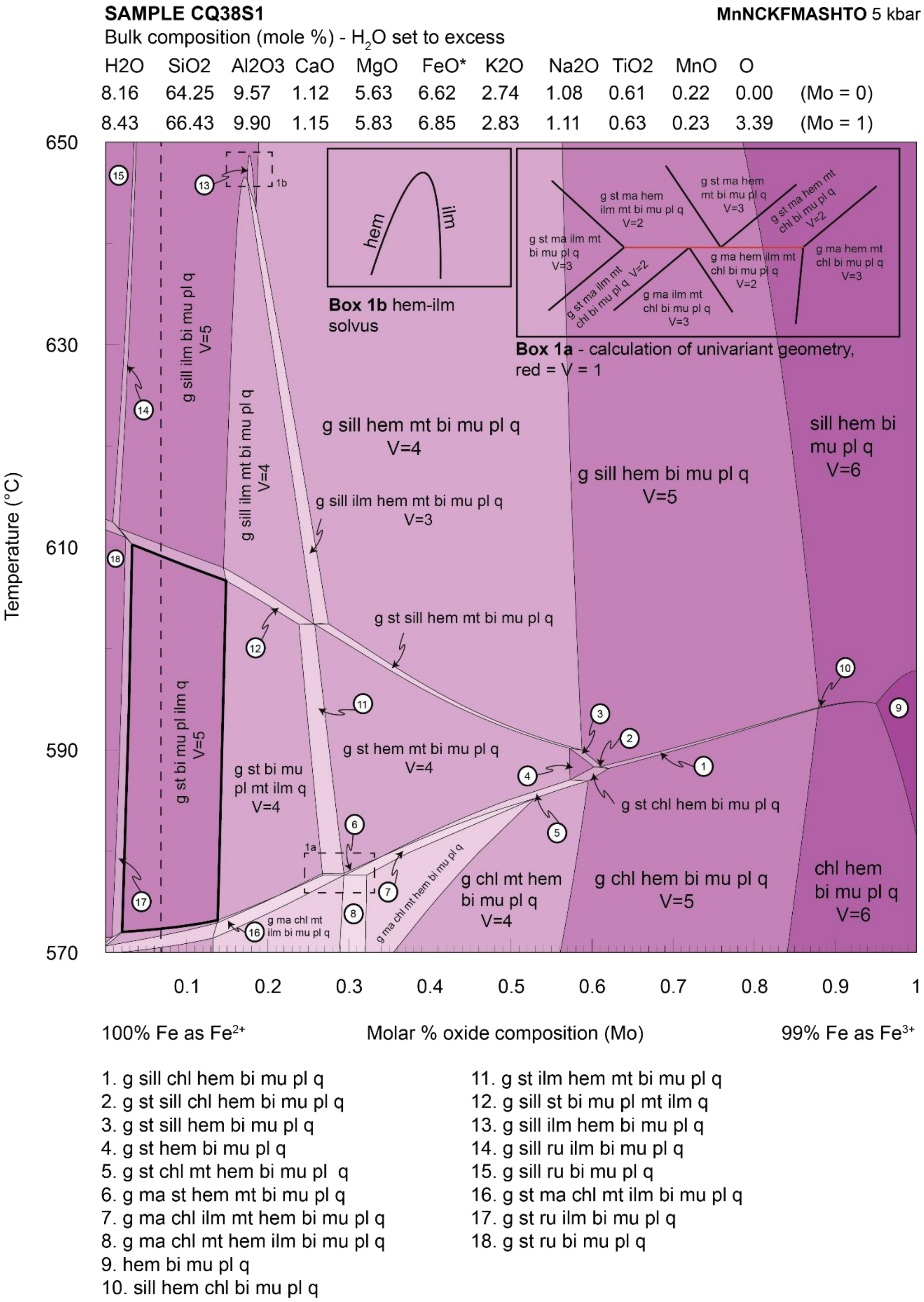

Figure 18: Calculated T–M_O pseudosection for CQ38S1. All fields in the diagram contain water, H_2O, as part of the equilibrium assemblage. Fields too small to be directly labelled are identified by numbered circles corresponding to the assemblage occurring within the field. Progressively darker tones are representative of increasing variance, V, where V = components – phases + 2 (components = 11). The compositions in mole% used to calculate the diagram, corresponding to that at M = 0 and M = 1, are provided above the diagram. FeO* = FeO + 2 × 'O'. The composition at M_O = 0.07 passes through the interpreted peak assemblage field garnet + staurolite + biotite + muscovite + ilmenite + plagioclase + quartz + H_2O, which occurs in the top left of the diagram (bold outline).

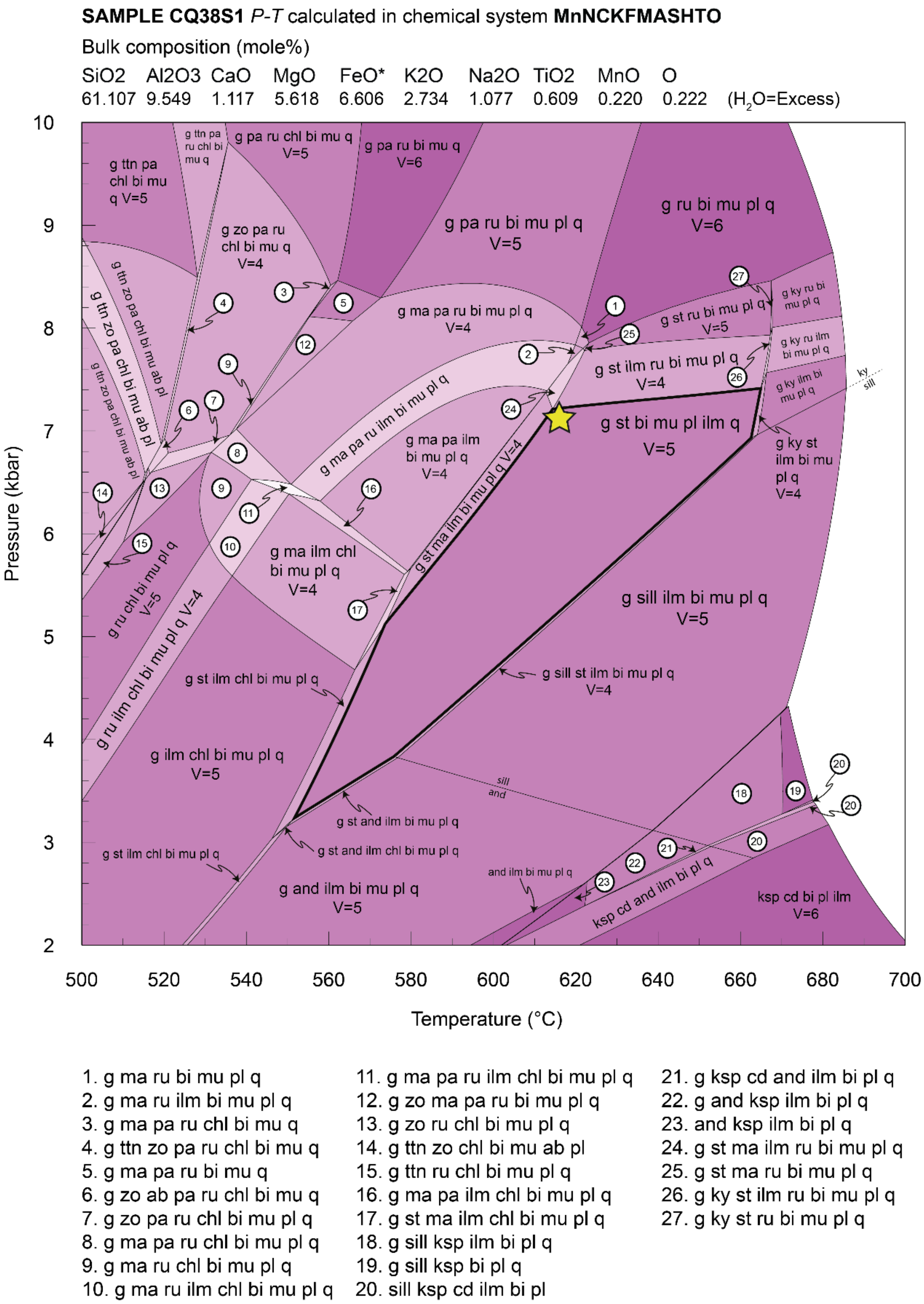

Figure 19: Calculated *P–T* pseudosection for sample CQ38S1. All fields in the diagram additionally contain water, H_2O, as part of the equilibrium assemblage. Fields too small to be directly labelled are identified by numbered circles corresponding to the assemblage occurring within the field. Progressively darker tones are representative of increasing variance, V, where V = components – phases + 2 (components = 11). The composition in mole% used to calculate the diagram, corresponding to that at M_O = 0.07 in Fig.18 is provided above the diagram. FeO* = FeO + 2 × ’O’. The white area at top right of diagram is melt-bearing. This was not calculated as the sample is not migmatitic The peak assemblage field garnet + staurolite + biotite + muscovite + ilmenite + plagioclase + quartz + H_2O is outlined in bold.

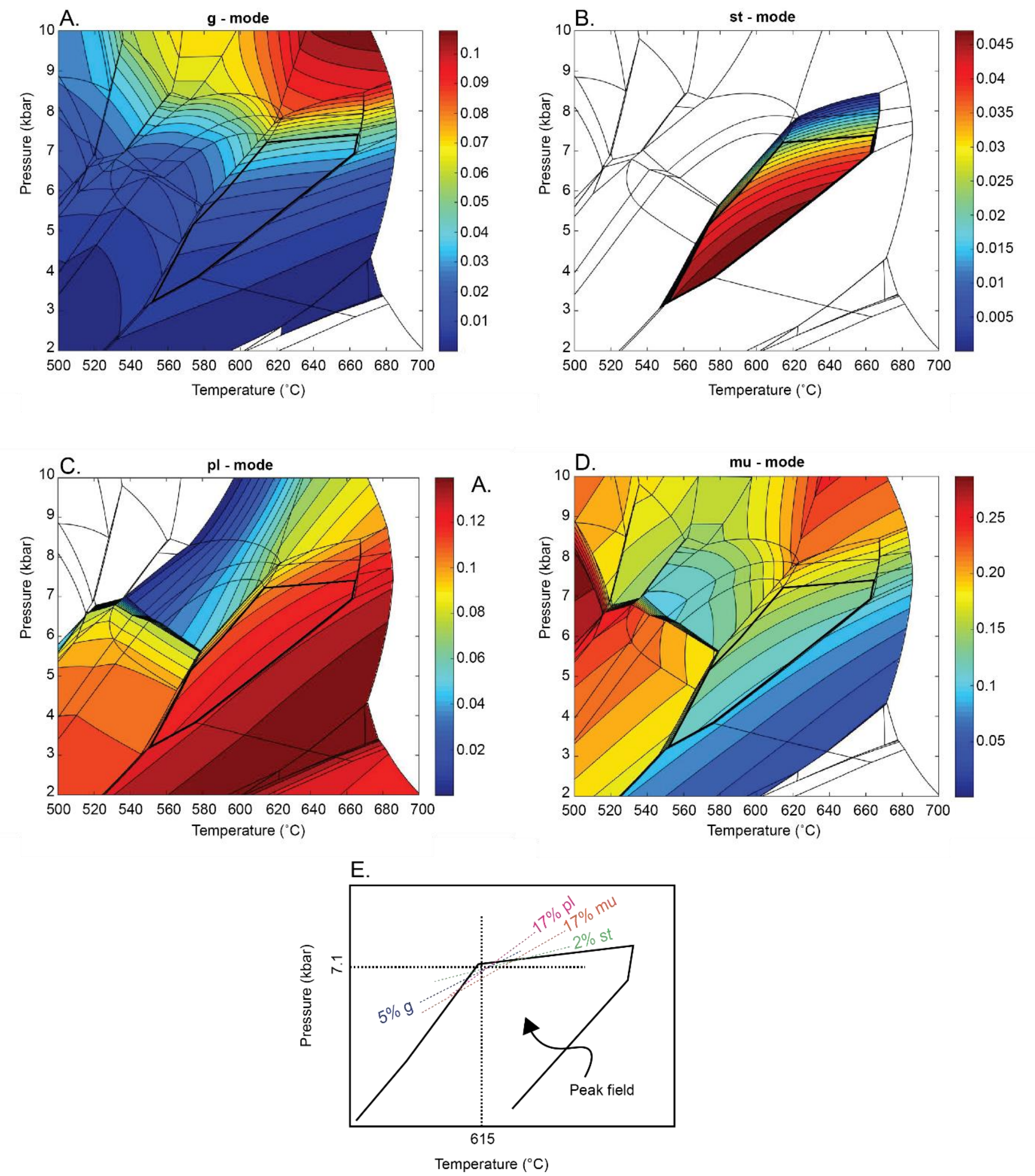

Figure 20: Calculated *P–T* pseudosection for sample CQ38S1 contoured for the abundance (‘mode’) of some phases. The calculated abundance of phases in the peak assemblage field (at top left, bold outline, also in F) was used in conjunction with estimated abundances of minerals in the sample (Table 3) to choose an appropriate composition along the Mo axis for calculation of the *P–T* pseudosection, Fig.16. Diagram (F) shows the detail of the peak assemblage field with calculated abundances of phases (combination of A, B, C and D) coinciding with estimated modal proportions in Table 3 to further constrain the metamorphic conditions within the peak assemblage field.

DISCUSSION

The aim of this study is to understand the source, timing of metamorphism and thermal character of schists within the complex framework of the (northern) Qinling Orogen, for the purpose of providing constrains on models of its tectonic evolution. Published data including detrital zircon geochronology, magmatic geochronology and *P–T–t* constraints are used as the basis with which to compare the results of this study.

Geomorphological analysis of schist boulder provenance

The probable source and total displacement of schist samples occurring as boulders in mountain stream settings within the NQB are constrained by the integration of several key observations and data detailed in Appendix B. These include: (i) the known origin of the streams and drainage divide of the river system with respect to the known geology (Fig. 1c); (ii) the hydrological processes influencing bedload transport and (iii) weathering rates of comparable rock-types. It is reasonable to infer that samples in this study do not have a long residence time in the streams, and in combination with (i), (ii) and (iii), have probably travelled a maximum distance of the order of ~10 km. The conclusions derived from this analysis are discussed further in subsequent sections outlining U–Pb zircon geochronology of the schists, and comparison between monazite ages from the schists and known tectono-thermal events within the framework of the QOB.

Geochronology

Zircon and monazite are the two most widely used geochronometers for understanding high-temperature processes and sources of rocks in the crust (e.g. Spear & Pyle, 2002; Dempster et al., 2004; Taylor et al., 2016). Zircon has additional utility as a detrital mineral for constraining the provenance of sedimentary rocks (e.g. Fedo et al., 2003). The rocks of this study record mid to upper-amphibolite facies temperatures, but have not melted. This is crucial for the interpretation of age data from zircon and monazite. Zircon is largely unresponsive to metamorphism up-temperature until partial melting occurs (e.g. Rubatto et al., 2001; Dempster et al., 2004; Rubatto et al., 2013). Conversely, monazite commonly commences growth during prograde metamorphism at temperatures of ~400–500 °C (e.g. Smith & Barreiro, 1990; Janots et al., 2008).

INTERPRETATION OF U-PB ZIRCON GEOCHRONOLOGY

Although zircon is largely unresponsive to metamorphism below the solidus, a number of factors need to be considered in order to correctly interpret the age data collected in this study. First, the internal structure or zoning of zircon, as revealed by CL imaging, provides critical clues as to its origin and evolution. Zircon grains of igneous origin are characterised by oscillatory zoning (Corfu et al., 2003). Xenocrystic cores mantled by overgrowths with oscillatory zoning are interpreted as inheritance in igneous sources (Corfu et al., 2003). Pre-existing zircons modified by metamorphic processes, or grown during metamorphism, are typically characterised by sub-rounded grain morphologies and homogeneous CL responses (Corfu et al., 2003; Taylor et al., 2016). Second, zircon is known to grow at low grades of metamorphism—greenschist facies or lower—in some cases in slates and phyllites (Dempster et al., 2008; Hay & Dempster, 2009). However, very small zircon grains (~5–30 μm), interpreted to be detrital, can also occur in low-grade (sub-solidus) metasedimentary rocks (e.g. Hay & Dempster, 2009).

The internal structure of zircon grains from sample QL-3 are dominantly characterised by oscillatory zoning and/or xenocrystic cores mantled by small overgrowths with oscillatory zoning (Fig. 6b). Therefore, it is interpreted that much of the zircon in QL-3 is detrital. For samples 2QS2, 4QS4 and CQ38S1, the entire zircon age datasets were obtained from separated grains < 30 μm in size due to an absence of larger zircons. These grains did not show any internal structure with CL imaging. At face value, this makes it difficult interpret whether such grains are metamorphic or detrital origin (e.g. Dempster et al., 2004; Dempster et al., 2008; Hay & Dempster, 2009). However, by comparison to existing magmatic and detrital age spectra from the QOB in the following section, it is possible to interpret their origin.

SOURCE OF SCHISTS USING ZIRCON DETRITAL AGE SPECTRA COMPARISONS

Numerous datasets of magmatic, metamorphic and detrital zircon ages exist for the QOB (e.g. Diwu et al., 2012; Bader et al., 2013; Yu et al., 2015; Dong & Santosh, 2016). To constrain the source of the schists in this study and decipher whether < 30 μm zircon grains are detrital or metamorphic in origin, Figs. 21–23 compare the zircon geochronology of this study to published data.

The drainage system in which sample QL-3 was collected starts amongst Devonian units (Liuling Group), and flows north through the NQB. Fig. 21 compares the age spectra to that of the Liuling Group (Fig. 21c) and NQB and FAS (Fig. 21b). Ages for the NQB between ca. 400–500 Ma are a mix of metamorphic and magmatic ages, not detrital (Diwu et al., 2014). The age spectra for QL-3 (purple shaded columns to aid comparison) compares favourably with parts of the spectra for the NQB (especially ca. 510–1050 Ma) and Liuling Group. The FAS is characterised by detrital zircon ages between ca. 455–600 Ma and ca. 700–800 Ma. However, sample QL-3 arguably compares most favourably with the FAS (compare Fig. 21a with Fig. 21b). The FAS is reported to contain a mixture of rock types as is typical of forearc sequences, but pelites are not described. However, there are no relict Barrovian-style metamorphic minerals in QL-3 (see CQ38S1), which might be expected based on metamorphic ages (see monazite geochronology discussion). Therefore, the Liuling Group rather than the FAS may be the source of QL-3. Zircon ages ≤ 400 Ma in QL-3 cannot belong to the FAS or the Liuling Group as this age post-dates the deposition of both packages ca. 400 Ma (Dong & Santosh, 2016). These analyses are discussed separately below.

Samples 2QS2 and 4QS4 are from the same drainage system as QL-3 (Fig. 1c, Table 2). As the total zircon yield of concordant zircon from 2QS2 and 4QS4 is comparatively low (Fig. 7c, Fig. 8c) it is difficult to definitively constrain the source of these samples. As for QL-3, zircon age spectra for 2QS2 and 4QS4 are dominantly between ca. 400–600 Ma and ca. 700–1300 Ma, with fewer ages occurring ca. 1500-1700 Ma, ca. 2200–2900 Ma (2QS2) and a single peak at ca. 2700 Ma (4QS4). The FAS arguably has a better spectra fit than the Liuling Group. However using the logic argued for QL-3, the Liuling Group is interpreted to reflect the most likely source for these samples. As such, this additionally implies that the ≤ 30 μm zircons are for the most part detrital. Analogous to sample QL-3, zircon ages ≤ 400 Ma post-date deposition of the Liuling Group and are discussed separately below.

Sample CQ38S1 was collected from a drainage system to the east of the remaining samples, where the headwaters of the streams occur within the NQB. Therefore CQ38S1 may not share a similar source to samples QL-3, 2QS2 and 4QS4. Figure 21 shows a comparison of age spectra from CQ38S1 to QL-3 and numerous parts of the QOB and its bounding cratons. Because the Liuling Group and FAS (Fig. 21c, 21b) contain detritus from numerous sources, including the NQB represented by the Qinling Group, the zircon age spectra for these packages compares well with that of CQ38S1. Ages in CQ38S1 between ca. 630–730 and ca. 830–920 are identified in both the NQB and SQB. For the SQB these ages form shoulders to the major peak at ca. 730 Ma and for the NQB major identifiable age peaks align with the ages in CQ38S1 in (Fig. 21a,b). However, the NQB can be ruled out as a source as its maximum deposition age is ca. 850 Ma and the ca. 400–500 peak in the spectra (Fig. 21b) is in fact a mix of metamorphic and magmatic rather than detrital ages (Diwu et al., 2014). The

SQB can be ruled out because it is south of the drainage divide (Fig. 1c). CQ38S1 was most likely sourced from FAS or Liuling Group. The FAS is more likely than the Liuling Group because the Liuling Group does not appear to show evidence of Barrovian-style metamorphism (e.g. QL-3), wheras the FAS is known to consist of reclict garnet bearing assemblages (Yan et al., 2016). This interpretation is consistent with the FAS being intruded by a dyke dated at 435 ± 7 Ma (Dong et al., 2013), which constrains the maximum depositional age for the FAS within the proximity of this study. Ages < ca. 435 Ma defining the FAS in Fig. 21b are from a younger part of the FAS that occur further east of the sample locations in this study (Yan et al., 2016).

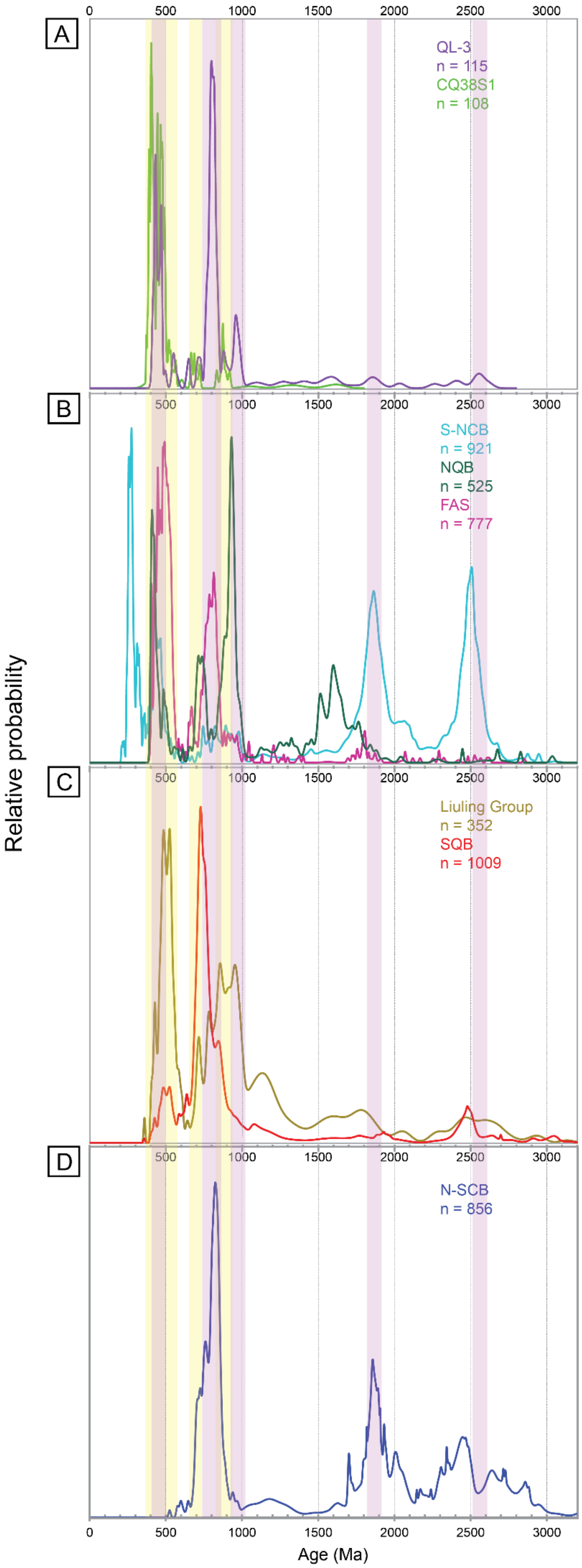

Figure 21: U–Pb zircon dataset comparison for samples QL-3 and CQ38S1 (A) U–Pb detrital zircon ages from samples QL-3 and CQ38S1 collected in this study; (B) U–Pb detrital zircon age spectra of the southern part of southern- North China Craton (S-NCB) datasets are sourced from: (Li et al., 2010; Zhu et al., 2011; Diwu et al., 2012; Yang et al., 2014). The U–Pb age spectra for the NQB excludes the Kuanping Group (detrital U–Pb zircon ages between 610-500 Ma) and Erlangping Group as there are no existing datasets for the group—but combines detrital zircon ages (≥ 850 Ma) attributed to the Qinling Group with magmatic and metamorphic ages which are erroneously incorporated into modern U–Pb 'detrital zircon spectra' for the NQB (metamorphic ages are attributed to ages between 530–400 Ma, and magmatic ages are attributed to ranges 950–850 Ma related to the southward subduction of the Kuanping Ocean and 867–729 Ma mafic rocks and 730–610 Ma mafic-granitic dykes in the Qinling and Kuanping groups), these datasets collectively characterise the NQB—sourced from: (Lu et al., 2006; Yu et al., 2009; Yan et al., 2010; YuSheng et al., 2011; Diwu et al., 2014). U–Pb detrital zircon age spectra for the FAS is sourced from: (Dong et al., 2013; Yan et al., 2016); (C) Detrital U-Pb zircon ages from the SQB are sourced from: (Dong et al., 2013; Liu & Zhang, 2013; Shi et al., 2013; Zhu et al., 2014). Magmatic ages in the SQB occur 760–710 Ma, U–Pb detrital zircon ages for the Liuling Group are sourced from Dong et al. (2013); (D) U–Pb detrital zircon ages for the northern South China Craton (N-SCB) are sourced from: (Wang et al., 2012; Chen et al., 2013; J. Wang et al., 2013; L. Wang et al., 2013; Yin et al., 2013). Coloured vertical bars through the diagram correspond to age peaks or distributions in QL-3 and CQ38S1 to aid in comparison to other datasets. Samples 2QS2 and 4QS4 are not shown in this diagram due to population size, but are shown separately in Fig. 21.

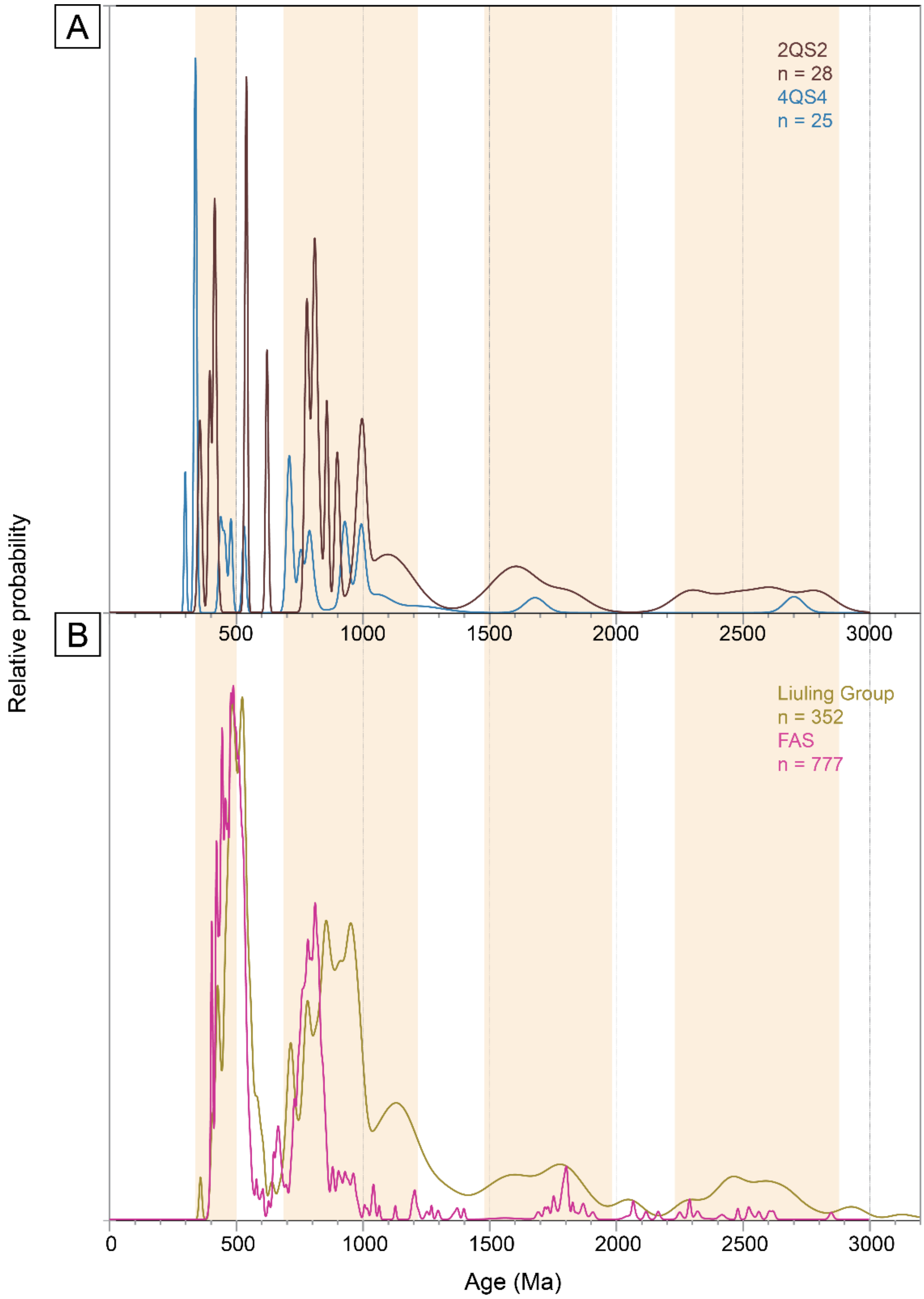

Figure 22: (A) U–Pb detrital zircon ages from samples 2QS2 and 4QS4 collected in this study; (B) U–Pb deital zircon datasets representing the Liuling Group turbidite, source; (Dong et al., 2013) and the forearc sequences, a product of detritus from the NQB, during northward subduction of the Shangdan Ocean, source; (Dong et al., 2013; Yan et al., 2016). A low abundance of zircon in both samples 2QS2 and 4QS4 makes comparison difficult. However broadly these samples align with both the Liuling Group and FAS. Coloured vertical bars through the diagram correspond to age peaks or distributions in 2QS2 and 4QS4 to aid in comparison to datasets of the Liuling Group and FAS.

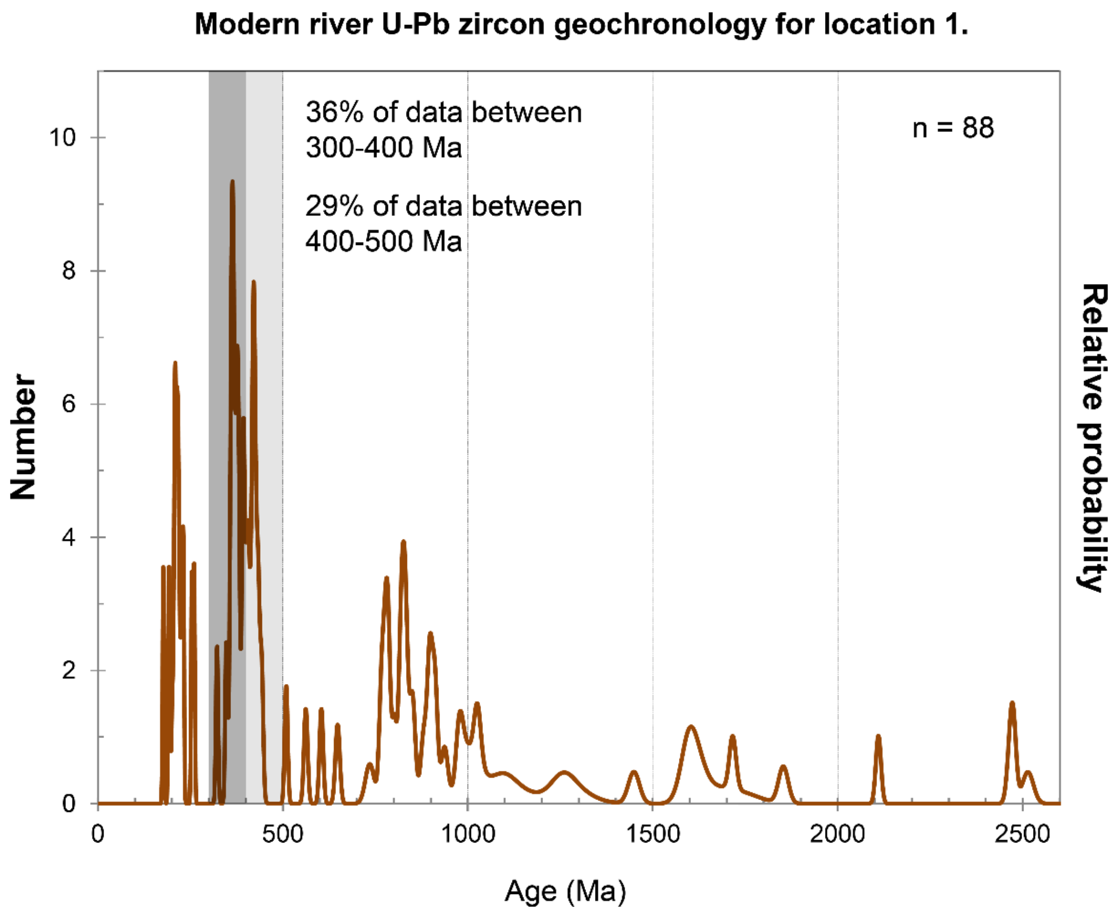

Figure 23: Detrital zircon U–Pb spectra for modern river sediments of the north flowing river system which forms part of location 1, sourced from Hong (2008). This plot demonstrates that detrital zircons with ages corresponding to potential contaminants e.g. < 400 Ma, form an abundant part of the river material to which samples QL-3, 2QS2 and 4QS4 were collected from.

INTERPRETATION OF U–PB MONAZITE GEOCHRONOLOGY

Monazite is well understood to grow in metasedimentary rocks during prograde metamorphism (e.g. Smith & Barreiro, 1990; Wing et al., 2003; Corrie & Kohn, 2008; Janots et al., 2008). Detrital monazite is understood to mostly have reacted or recrystallized to form metamorphic monazite by ~350 °C (e.g. Wing et al., 2003; Janots et al., 2008). However, monazite is also known to be responsive to resetting in the presence of hydrothermal fluids (e.g. DeWolf et al., 1993; Janots et al., 2012; Seydoux-Guillaume et al., 2012; Didier et al., 2013). As all the schist in this study preserves mid-upper amphibolite facies mineral assemblages (cordierite; cordierite + andalusite; garnet + staurolite), attesting to temperatures of > 550 °C, monazite age data in this study are plausibly the result of: (i) a single metamorphic event or (ii) poly-metamorphism: or (iii) fluid-rock interaction resetting the U–Pb system. Samples QL-1, QL-2 and QL-3 record monazite ages in the range 214.2 ± 7.6 Ma (lower intercept) to 228.9 ± 4.5 Ma (concordia age). For each sample, the agreement (within uncertainty) between the concordia and lower intercept ages suggests that the ages are robust. The spread of data along a discord in QL-2 (Fig. 11c) is attributed to common Pb as the upper intercept approximates the age of Earth. Monazite age data from these three samples are coincident with zircon U–Pb geochronology of granulite facies metamorphism at ca. 220 Ma within the SQB (Yang et al., 1999), as well as known intrusion of voluminous granitoids and dykes in the interval 230–210 Ma (Dong et al., 2011b; Zhang et al., 2016) in the SQB and the southern part of the NQB, as shown in Fig. 1. Within the vicinity of the study area, examples of Upper Triassic granitoids intrude the Liuling Group and the NQB (Fig. 1c). Therefore it is interpreted that the monazite data records the age of metamorphism in these three schist samples.

The monazite geochronology of sample CQ38S1 is complex. Arguably a population occurs at 405.0 ± 1.5Ma (concordia age), but there are also a significant number of younger analyses (Fig. 13). Although metamorphism in the QOB, and more specifically the NQB, is mostly thought to cease at ca. 400 Ma (Fig. 2), individual studies (e.g. Tang et al., 2015) suggest that migmatisation continued until ca. 380 Ma, and monazite resetting related to post-orogenic deformation until ca. 350 Ma (Table 1; Bader et al., 2013). As the monazite data for CQ38S1 records ages as young as ca. 325 Ma (Fig. 13c), it is conceivable that either (1) metamorphism was protracted over an interval of ca. 80 Myr, (2) that hydrothermal fluids caused partial resetting of ca. 405 Ma metamorphic monazite, to result in ages being drawn down concordia to ca. 325 Ma, or (3) that a combination of both occurred. The spread of concordant ages between 400–330 Ma is coincident with three biotite $^{40}Ar/^{39}Ar$ ages occurring between 330–368 Ma in the NQB (Dong et al., 2011c). As it is not currently possible to distinguish between these possibilities, it is tentatively interpreted that the 405.0 ± 1.5 Ma concordia age represents the timing of metamorphism, and that a combination of protracted metamorphism and partial resetting led to the spread of monazite ages along concordia to ca. 325 Ma. Evidence for limited retrogression (chlorite mantling garnet) makes it reasonable to attribute some of this spread to fluid-related resetting processes.

ORIGIN OF ≤400 Ma ZIRCONS IN SCHIST SAMPLES

All samples (except QL-3) analysed for zircon geochronology contain zircons that are apparently younger than the published maximum deposition age of the metasediment host. Samples 2QS2 and 4QS4 are argued to be sourced from the Liuling Group which has a maximum deposition of age of 400 Ma (Dong et al., 2013). Sample CQ38S1 is argued to be derived from the NQB, which although comprises many groups, contains a youngest deposition age of ca. 455 Ma, represented by the FAS (Dong et al., 2013). A detrital zircon study of modern stream sediments in the drainage systems of this study by Hong (2008) showed that a significant proportion of the zircon age data (32%) is ≤ 400 Ma (Fig. 23). Ages in the interval 190–250 Ma (Fig. 23) correspond to known ages of Triassic magmatism in the QOB (Dong et al., 2011b; Lu et al., 2016; Zhang et al., 2016). Ages in the interval ca. 380–400 Ma correspond to migmatisation and granitoid emplacement in the NQB (Tang et al., 2015; Dong & Santosh, 2016). As abundant amounts of zircons of these ages occur in the streams (Fig. 23), and the boulder material in the streams is greatly dominated by granitic rock as opposed to schist, it is possible that the schist has been contaminated by these young zircons as boulder transport down the high gradient mountain stream occurs. In the specific cases of ≤ 30 μm zircons separated from samples 2QS2 and 4QS4, they may have migrated into microfractures and/or impacted into the mica rich matrix during boulder transport. An analogous phenomenon occurs at Port Macquarie on the east coast of Australia where from low-temperature eclogites and later intrusive trondhjemite have published zircon ages (Aitchison & Ireland, 1995; Nutman et al., 2013) that are erroneously dated to zircon ages in the modern beach sand (Sircombe, 1999), pointing to modern contamination during high impact beach wave action.

Pressure–Temperature conditions

LIMITATIONS OF PHASE EQUILIBRIA MODELLING

As the model chemical system MnNCKFMASHTO was used to represent a complex natural system, it is acknowledged that there are a number of limitations. For example, chemical components such as ZnO, Cr_2O_3 and P_2O_5 cannot be modelled to represent natural mineral equilibrium processes involving these components in minerals such as staurolite (ZnO) and apatite (P_2O_5). Apatite occurs as an accessory mineral in samples of this study but, at present, cannot be modelled in the available model chemical systems. Apatite is a Ca-bearing phase, therefore its absence from calculations increases the stability of Ca-bearing phases in the calculations, such as garnet and plagioclase. However, the abundance of apatite is very low (<< 1%) by contrast to the abundance of garnet and plagioclase (Table 3), the whole rock compositions of most samples contain very little P_2O_5 (Appendix C), and all samples contain monazite. Therefore, the impact of Ca contained in apatite being included in the model calculations is here considered to be minor (Morrissey et al., 2015).

PURPOSE OF PHASE EQUILIBRIA MODELLING

Phase equilibria modelling has been used to determine the thermal character recorded by the schist samples, for the purpose of constraining their potential tectonic significance in the architecture of the QOB. In sample QL-1, the peak assemblage biotite + cordierite +

plagioclase + rutile + quartz (+ water) is preserved with no evidence of retrogression. Therefore the abundances of the minerals estimated from thin section (Table 3) may be used in conjunction with calculated abundances ('modes') to constrain the peak *P–T* conditions. The region with the peak assemblage field (Fig. 16) that corresponds most closely with the observed and calculated modes is in the *P–T* range ~0.6–4.25 kbar, ~540–670 °C. This *P–T* range corresponds to approximate apparent thermal gradients of between about 135 °C/kbar and 900 °C/kbar.

Inferring a *P–T* path for sample QL-1 is difficult due to the lack of inclusions in cordierite that differ from the matrix minerals, and also due to the lack of obvious retrograde reaction. However, the lack of andalusite in this rock probably precludes the prograde *P–T* path from passing through andalusite-stable fields because andalusite is known to be a sluggish reactor (Alias et al., 2002; Pattison & Tinkham, 2009). Therefore, if the prograde path had passed through andalusite-stable fields to the peak (andalusite-absent) field, one may expect relict andalusite to survive in the rock. Although not a robust constraint, the absence of K-feldspar inclusions in cordierite suggests a prograde path traversing about 1–2 kbar.

As andalusite occurs in samples 2QS2 and 4QS4 and is interpreted to post-date cordierite due to its spatial positioning, the retrograde *P–T* path for these samples, and perhaps by inference for QL-1, passed up-pressure into andalusite stability (e.g. Fig. 16; Alias et al., 2002). The absence of late andalusite from QL-1 may reflect sluggish nucleation or rock composition unsuitable for the growth of andalusite. If the interpretation of a post-peak up-pressure *P–T* evolution is correct for QL-1, this probably means the prograde part of the *P–T* path involved either a gradual pressure increase to peak pressure or effectually remaining at the pressure corresponding to peak pressure if the rock was metamorphosed as a consequence of contact metamorphism (see later). Regardless of the specifics of the prograde trajectory, this most likely means that chlorite and muscovite were once stable in sample QL-1 (see lower-temperature part of Fig. 16). The prograde growth of cordierite probably formed at the expensive of H_2O-bearing chlorite and muscovite, via the simplified reaction chl + mu → cd + bi.

In sample CQ38S1 the peak assemblage biotite + garnet + staurolite + muscovite + plagioclase + ilmenite + quartz (+ water) is preserved with only minor amounts of biotite and muscovite (that occurring in fractures in garnet) and rare localised examples of chlorite mantling garnet that are attributed to retrogression. Therefore the abundances of the minerals estimated from thin section (Table 3) may be used in conjunction with calculated modes to constrain the peak *P–T* conditions. The region within the peak assemblage field (Fig. 19) that corresponds most closely with the observed and calculated modes is the top left, where staurolite abundance is low, at ~7 kbar and ~615 °C. This *P–T* condition corresponds to an apparent thermal gradient of ~87 °C/kbar, which is a typical 'Barrovian' thermal character (Stüwe, 2007; e.g. Brown, 2014). Inferring a *P–T* path for this sample is difficult due to a lack of extensive retrogression and the absence of an inclusion record in garnet and staurolite to provide information about the prograde trajectory. However, given that Barrovian thermal regimes are *typically* associated with metamorphism resulting from convergence (e.g. Brown, 2006; Brown, 2007; Brown, 2014), it may be that the *P–T* path was clockwise (e.g. England & Richardson, 1977).

REGIONAL IMPLICATIONS

Apparent thermal gradients constrained from analysis of metamorphic mineral assemblages may be used in conjunction with other geological information to provide constraints on the tectonic setting of metamorphism (e.g. Stüwe, 2007; Brown, 2014; Kelsey & Hand, 2015). This is chiefly because different tectonic settings are characterized by different thermal regimes (Spear, 1993; Vernon & Clarke, 2008). For sample QL-1 with apparent thermal gradients of ~135–900 °C/kbar, these very high values may correspond to regional extension or contact metamorphism in the upper crust. South of the sample site for QL-1 (and 2QS2, 4QS4) in the northern SQB migmatisation to produce garnet–sillimanite-bearing assemblages is reported to be ca. 220 Ma in age (Yang et al., 1999), coincident with the age of metamorphism in the cordierite schists. Migmatisation occurs at upper-amphibolite and granulite facies conditions and therefore requires elevated thermal gradients. *P–T* conditions are not provided by Yang et al. (1999) so it is not possible to directly compare to those estimated for sample QL-1.

If it is assumed that the extreme thermal gradients for QL-1 were regional, the total thickness of crust could not exceed ~4.5–15 km (assuming density where 1 kbar = 3 km). Continental crustal thickness of ≤ 15 km, would necessitate (extreme) crustal extension. The ca. 220 Ma timeline in the QOB is characterised by emplacement of voluminous granitoids (Dong et al., 2011b; Zhang et al., 2016), which are interpreted to have intruded in a thickened orogen (e.g. Zhang et al., 2016 and references therein). In addition, the total thickness of the Liuling Group is estimated to be 3–4 km (Dong et al., 2013).

In light of these constraints, it appears unlikely that total crustal thickness was regionally in the range ~4.5–15 km. As a result, the alternative of contact metamorphism in the shallow crust may provide the most reasonable explanation for the generation of the cordierite schists where magmatic heating caused local steep thermal gradients (Lux et al., 1986; Barton & Hanson, 1989; Collins & Vernon, 1991). Cordierite—and andalusite—are common minerals in shallow contact aureoles (Symmes & Ferry, 1995; Baboza & Bergantz, 2000; Alias et al., 2002; Pattison & Tinkham, 2009) and attest at least locally to steep or extreme thermal gradients. In samples QL-1, QL-2, QL-3, 2QS2, 4QS4, cordierite is wrapped by a biotite–quartz (± muscovite) fabric. This implies that contact metamorphism, and indeed magmatic emplacement, occurred in a dynamic, deforming orogenic system, rather than in a static environment. In this interpretation, regional migmatisation (215–210 Ma) occured at deeper crustal levels (Zhang et al., 2016). Closure of the Mianlue Ocean (Fig. 1a), resulting in amalgamation of the South China Craton/Block with the SQB–NQB–S-NCB, occurred at ca. 220 Ma (Zhang et al., 2016) and is the most reasonable cause of the regional deformation and magmatism and contact metamorphism at ca. 220–230 Ma.

For sample CQ38S1, the apparent thermal gradient of ~87 °C/kbar corresponds to a Barrovian-style thermal regime. The age of metamorphism in CQ38S1 is uncertain, but possibly occurs at ca. 405 Ma, or extends over a protracted period to ca. 325 Ma. If the 405 Ma age corresponds to peak or near-peak metamorphism, then thickening of the FAS must have preceded ca. 405 Ma. Similar Barrovian-style schists (garnet–staurolite ± kyanite ± sillimanite) in the NQB occur ~150 km west of the sample site for CQ38S1 record EPMA monazite ages of 435 ± 9 Ma (Table 1; Chen et al., 2006). However, the discordance uncertainty in chemical age data (e.g. Suzuki & Kato, 2008; Spear et al., 2009) makes it unclear as to tectonic significance of this dataset. In the Tongbai Orogen—600 km to the east representing the continuation of the Qinling Orogen—the ‘Guishan Complex’ is arguably related to the FAS as it is characterised by a forearc sedimentary protolith metamorphosed in a Barrovian-style thermal regime (65–75 ˚C/kbar; Liu et al., 2011), highlighting that this thermal character probably had regional extent.

Taken as a whole, the existing age data highlights that the geological evolution of the NQB and QOB remains unresolved in detail. Retrogression associated with exhumation of the tectonically thickened NQB is interpreted have ceased by ca. 400 Ma (e.g. Bader et al., 2013; Dong et al., 2016; Liu et al., 2016), and cooling continued until ca. 330 Ma. (e.g. Table 1; Dong et al., 2011c). Others interpret that migmatisation occurred in the NQB as late as ca. 380 Ma (Table 1; e.g. Bader et al., 2013; Tang et al., 2015). Nevertheless, there is evidence that crustal thickening and metamorphism occurred in the NQB as a consequence of subduction-related convergence of the Shangdan Ocean leading up to ca. 400 Ma (Fig. 2).

However, this presumably did not set up the Barrovian thermal conditions in the FAS as forearcs are not typically known to involve warm thermal regimes (e.g. Baitsch-Ghirardello et al., 2014). Metamorphism continued during final ocean closure and arc-continent collision at ca. 420–400 Ma (Dong & Santosh, 2016) and it is at this time that Barrovian thermal conditions were presumably generated by thickening of the FAS (e.g. Dymkova et al., 2016). This suggests that originally forearc-derived sequences were no longer located in the forearc setting by the time of metamorphism, ca. 35 Myr later than the maximum depositional age. Metamorphism potentially continued for some time following, until at least ca. 380 Ma and possibly to ca. 352 Ma. However, monazite ages later than ca. 400 Ma in the NQB are typically attributed to deformation and resetting processes (e.g. Table 1; Bader et al., 2013).

Using constraints from the samples investigated in this study, as well as information and data sources in Fig. 2, (e.g. Bader et al., 2013; Dong & Santosh, 2016), Fig. 24 shows a series of schematic cross-sections conveying the tectonic evolution of the QOB for the timelines of direct relevance to the metamorphism of samples investigated in this study. Existing models are deficient in the thermal characterisation of lithologies younger than the early Neoproterozoic or subduction related mafic rocks—these rocks alone cannot represent the full complex evolution of the QOB. The Kuanping Group, Erlangping Group, FAS, and Liuling Group are limited to unclear age constrains, lacking meaningful thermal character (Table 1). Importantly, the value of this study provides the first detailed and coupled *P–T–t* constrains from the Liuling Group and FAS (Fig. 24), two sequences that are poorly studied in terms of their metamorphic character. These constrains require that tectonic models for the evolution of the OQB must now include Barrovian-style metamorphism.

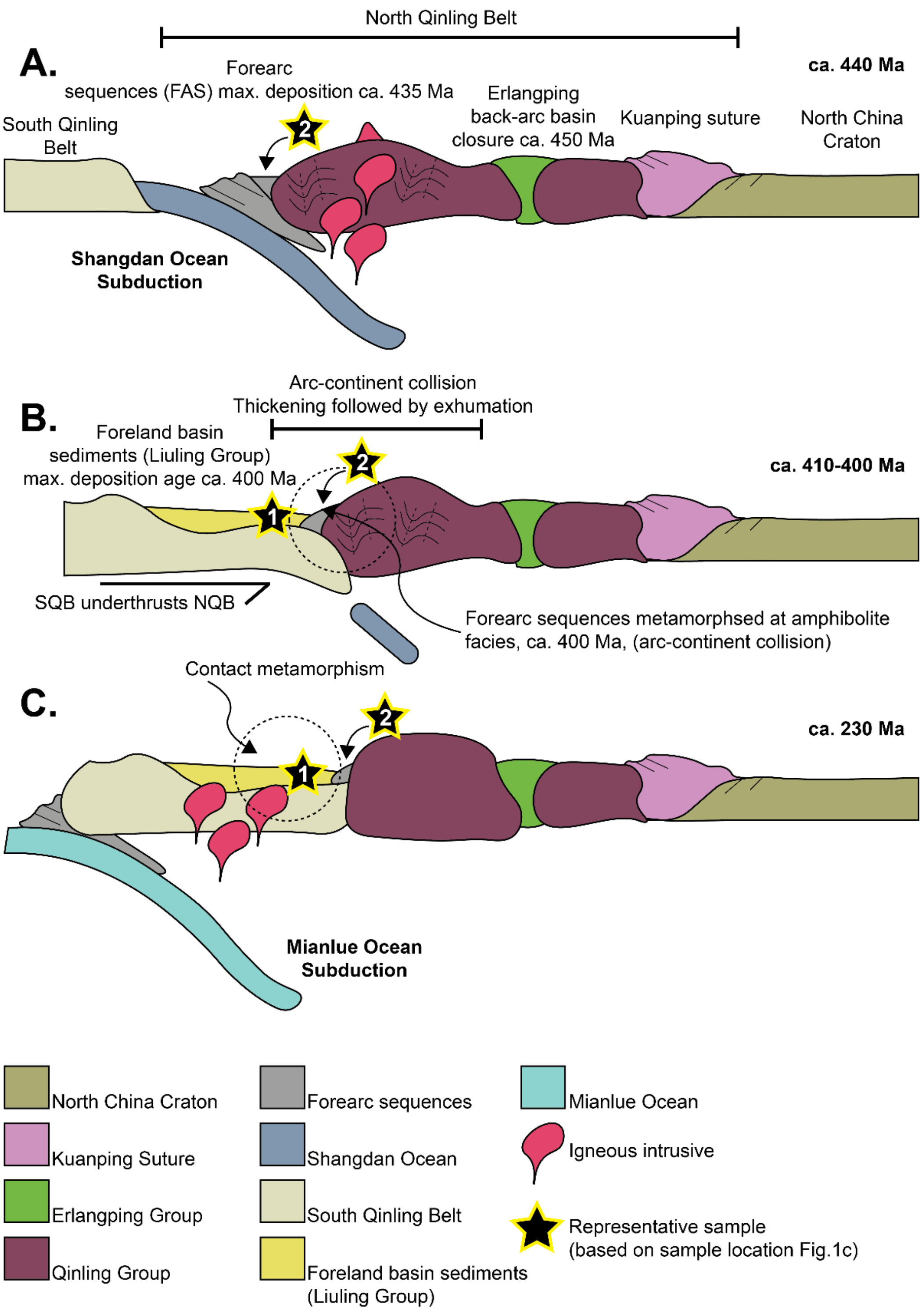

Figure 24: Schematic north–south oriented cross-sections for the tectonic evolution of the QOB during the ca. 440 (earliest Silurian) to ca. 230 Ma (mid Triassic) interval: (A) Shangdan Ocean closure with deposition of the fore-arc sediments (FAS), which were intruded at ca. 435 Ma by mafic dykes; (B) Exhaustion of the Shangdan Ocean at ca. 400 Ma resulting in continent–continent collision and deposition of the Liuling Group in a foreland–basin on the northernmost SQB; (C) Voluminous Upper–Triassic magmatism in the SQB during thickening. Model is based on findings in this study, and adapted from Dong and Santosh (2016).

CONCLUSIONS

This study provides the first zircon and monazite age data coupled to detailed, quantitative *P–T* estimates to unravel the source and *P–T–t* history of in the Qinling Orogenic Belt, China. Detrital zircon geochronology constrains cordierite schists to be most likely sourced from the Devonian Liuling Group and garnet–staurolite schists most likely from the Ordovician-Silurian FAS. Cordierite schists have metamorphic ages that overlap with Late Triassic magmatism and metamorphism in the South Qinling Belt at 220–230 Ma. Calculated phase equilibria modelling constrains metamorphism of the cordierite schists to involve very steep apparent thermal gradients, between 135–900 ˚C/kbar, interpreted to represent contact metamorphism of Liuling Group turbidite sequence. Garnet–staurolite schist within the North Qinling Belt has metamorphic ages that align with known Late Palaeozoic events occurring at ca. 400 Ma, with metamorphism possibly occurring over a protracted interval to ca. 350 Ma that is also consistent with existing age data. Calculated phase equilibria modelling constrains metamorphism of the garnet–staurolite schist to involve Barrovian apparent thermal gradients of ~87 ˚C/kbar, interpreted to represent metamorphism of the forearc sequences as a consequence of arc-continent collision that marks final amalgamation between the NQB and SQB.

The *P–T–t* evolution of schists undocumented in previous studies now form a part of the known geological framework of the Qinling Orogenic Belt. Models of the QOB have previously excluded the evolution of forearc sequences and Barrovian metamorphism, which now must be incorporated into collisional models for the North Qinling Belt. These key findings constitute a platform for further research, as this study has identified meaningful thermal and geochronological data for the SQB and NQB to better understand the complex architecture and evolution of the QOB.

Acknowledgements

The Northwest University, Shaanxi Province, China, are thanked for their generous hospitality, assistance in the field and on campus. In particular, Professor Yunpeng Dong is greatly thanked for his support, time, guidance in the field and hospitality including all accommodation, and costs. Mr Hui Bo, Dr Shengsi Sun and Mr Yunfei Ren are thanked for their assistance in the field and on campus. My supervisor, Dr David Kelsey, is gratefully thanked for invaluable guidance and support throughout the course of this project. Henry Wenk and Professor Alan Collins are thanked for their assistance in the field. Dr Tom Raimondo and Professor Martin Hand are thanked for their guidance. The staff of Adelaide Microscopy including Aoife McFadden, Ben Wade and Ken Neubauer are thanked for their training on instrumentation and technical support throughout data acquisition. Laura Morrissey and Naomi Tucker are thanked for their guidance within this project. Classmates Renee Tamblyn and Adrian Gaehl are thanked for their ongoing support and advice.

References

AITCHISON, J. T., & IRELAND, T. (1995). Age profile of ophiolitic rocks across the Late Palaeozoic New England Orogen, New South Wales: implications for tectonic models. *Australian Journal of Earth Sciences, 42*(1), 11-23.

ALIAS, G., SANDIFORD, M., HAND, M., & WORLEY, B. (2002). The P–T record of synchronous magmatism, metamorphism and deformation at Petrel Cove, southern Adelaide Fold Belt. *Journal of Metamorphic Geology, 20*(3), 351-363.

BABOZA, S. A., & BERGANTZ, G. W. (2000). Metamorphism and anatexis in the mafic complex contact aureole, Ivrea Zone, Northern Italy. *Journal of petrology, 41*(8), 1307-1327.

BADER, T., FRANZ, L., RATSCHBACHER, L., CAPITANI, C., WEBB, A. A. G., YANG, Z., . . . LINNEMANN, U. (2013). The Heart of China revisited: II Early Paleozoic (ultra)high-pressure and (ultra)high-temperature metamorphic Qinling orogenic collage. *Tectonics, 32*(4), 922-947. doi:10.1002/tect.20056

BAITSCH-GHIRARDELLO, B., GERYA, T. V., & BURG, J.-P. (2014). Geodynamic regimes of intra-oceanic subduction: Implications for arc extension vs. shortening processes. *Gondwana Research, 25*(2), 546-560.

BARTON, M. D., & HANSON, R. B. (1989). Magmatism and the development of low-pressure metamorphic belts: Implications from the western United States and thermal modeling. *Geological Society of America Bulletin, 101*(8), 1051-1065.

BROWN, M. (2006). Duality of thermal regimes is the distinctive characteristic of plate tectonics since the Neoarchean. *Geology, 34*(11), 961-964.

BROWN, M. (2007). Metamorphic conditions in orogenic belts: a record of secular change. *International Geology Review, 49*(3), 193-234.

BROWN, M. (2014). The contribution of metamorphic petrology to understanding lithosphre evolution and geodynamics. *Geoscience Frontiers, 5*(4), 553-569.

CHEN, D., LIU, L., SUN, Y., ZHANG, A., LIU, X., & LUO, J. (2004). LA-ICP-MS zircon U-Pb dating for high-pressure basic granulite from North Qinling and its geological significance. *Chinese Science Bulletin, 49*(21), 2296-2304. doi:10.1360/03wd0544

CHEN, D. L., & LIU, L. (2011). New data on the chronology of eclogite and associated rock from Guanpo Area, North Qinling orogeny and its constraint on nature of North Qinling HP-UHP eclogite terrane. *Earth Science Frontiers, 18*(2), 158-168.

CHEN, Q., CHEN, N., WANG, Q., SUN, M., WANG, X., LI, X., & SHU, G. (2006). Electron microprobe chemical ages of monazite from Qinling Group in the Qinling Orogen: Evidence for Late Pan-African metamorphism? *Chinese Science Bulletin, 51*(21), 2645-2650. doi:10.1007/s11434-006-2152-7

CHEN, W. T., ZHOU, M.-F., & ZHAO, X.-F. (2013). Late Paleoproterozoic sedimentary and mafic rocks in the Hekou area, SW China: implication for the reconstruction of the Yangtze Block in Columbia. *Precambrian Research, 231*, 61-77.

CHENG, H., ZHANG, C., VERVOORT, J. D., LI, X., LI, Q., WU, Y., & ZHENG, S. (2012). Timing of eclogite facies metamorphism in the North Qinling by U–Pb and Lu–Hf geochronology. *LITHOS, 136-139*, 46-59. doi:10.1016/j.lithos.2011.06.003

CHENG, H., ZHANG, C., VERVOORT, J. D., LI, X., LI, Q., ZHENG, S., & CAO, D. (2011). Geochronology of the transition of eclogite to amphibolite facies metamorphism in the North Qinling orogen of central China. *LITHOS, 125*(3), 969-983. doi:10.1016/j.lithos.2011.05.010

CHURCH, M., & HASSAN, M. A. (1992). Size and distance of travel of unconstrained clasts on a streambed. *Water Resources Research, 28*(1), 299-303.

COLLINS, W. J., & VERNON, R. H. (1991). Orogeny associated with anticlockwise PTt paths: Evidence from low-P, high-T metamorphic terranes in the Arunta inlier, central Australia. *Geology, 19*(8), 835-838.

CORFU, F., HANCHAR, J. M., HOSKIN, P. W. O., & KINNY, P. (2003). Atlas of zircon textures. *Reviews in mineralogy and geochemistry, 53*(1), 469-500.

CORRIE, S. L., & KOHN, M. J. (2008). Trace-element distributions in silicates during prograde metamorphic reactions: Implications for monazite formation. *Journal of Metamorphic Geology, 26*(4), 451-464.

DEMPSTER, T. J., HAY, D. C., & BLUCK, B. J. (2004). Zircon growth in slate. *Geology, 32*(3), 221-224.

DEMPSTER, T. J., HAY, D. C., GORDON, S. H., & KELLY, N. M. (2008). Micro-zircon: origin and evolution during metamorphism. *Journal of Metamorphic Geology, 26*(5), 499-507.

DEWOLF, C., BELSHAW, N., & O'NIONS, R. (1993). A metamorphic history from micron-scale 207 Pb/206 Pb chronometry of Archean monazite. *Earth and Planetary Science Letters, 120*(3), 207-220.

DIDIER, A., BOSSE, V., BOULVAIS, P., BOULOTON, J., PAQUETTE, J.-L., MONTEL, J.-M., & DEVIDAL, J.-L. (2013). Disturbance versus preservation of U–Th–Pb ages in monazite during fluid–rock interaction: textural, chemical and isotopic in situ study in microgranites (Velay Dome, France). *Contributions to Mineralogy and Petrology, 165*(6), 1051-1072.

DIWU, C., SUN, Y., ZHANG, H., WANG, Q., GUO, A., & FAN, L. (2012). Episodic tectonothermal events of the western North China Craton and North Qinling Orogenic Belt in central China: constraints from detrital zircon U–Pb ages. *Journal of Asian Earth Sciences, 47*, 107-122.

DIWU, C., SUN, Y., ZHAO, Y., LIU, B., & LAI, S. (2014). Geochronological, geochemical, and Nd-Hf isotopic studies of the Qinling Complex, central China: Implications for the evolutionary history of the North Qinling Orogenic Belt. *Geoscience Frontiers, 5*(4), 499-513.

DONG, Y., GENSER, J., NEUBAUER, F., ZHANG, G. W., LIU, X. C., YANG, Z., & HEBERER, B. (2011c). U-Pb and 40Ar/ 39Ar geochronological constraints on the exhumation history of the North Qinling terrane, China. *Gondwana Research, 19*(4), 881-893. doi:10.1016/j.gr.2010.09.007

DONG, Y., LIU, X., NEUBAUER, F., ZHANG, G., TAO, N., ZHANG, Y., . . . LI, W. (2013). Timing of Paleozoic amalgamation between the North China and South China Blocks: evidence from detrital zircon U–Pb ages. *Tectonophysics, 586*, 173-191.

DONG, Y., SAFONOVA, I., & WANG, T. (2016). Tectonic evolution of the Qinling orogen and adjacent orogenic belts. *Gondwana Research, 30*, 1-5. doi:http://dx.doi.org/10.1016/j.gr.2015.12.001

DONG, Y., & SANTOSH, M. (2016). Tectonic architecture and multiple orogeny of the Qinling Orogenic Belt, Central China. *Gondwana Research, 29*(1), 1. doi:10.1016/j.gr.2015.06.009

DONG, Y., ZHANG, G., HAUZENBERGER, C., NEUBAUER, F., YANG, Z., & LIU, X. (2011a). Palaeozoic tectonics and evolutionary history of the Qinling orogen: Evidence from geochemistry and geochronology of ophiolite and related volcanic rocks. *LITHOS, 122*(1–2), 39-56. doi:http://dx.doi.org/10.1016/j.lithos.2010.11.011

DONG, Y., ZHANG, G., NEUBAUER, F., LIU, X., GENSER, J., & HAUZENBERGER, C. (2011b). Tectonic evolution of the Qinling orogen, China: Review and synthesis. *Journal of Asian Earth Sciences, 41*(3), 213-237. doi:10.1016/j.jseaes.2011.03.002

DUNYI, L., & DUNMIN, Z. (1988). Direct determination of the 207Pb/206Pb age of single grain zircon by use of the thermal emission mass spectrometer. *Geological Review, 34*(6), 496.

DYMKOVA, D., GERYA, T., & BURG, J.-P. (2016). 2D thermomechanical modelling of continent–arc–continent collision. *Gondwana Research, 32*, 138-150.
ENGLAND, P. C., & RICHARDSON, S. (1977). The influence of erosion upon the mineral fades of rocks from different metamorphic environments. *Journal of the Geological Society, 134*(2), 201-213.
FEDO, C. M., SIRCOMBE, K. N., & RAINBIRD, R. H. (2003). Detrital zircon analysis of the sedimentary record. *Reviews in mineralogy and geochemistry, 53*(1), 277-303.
GILDER, S., & COURTILLOT, V. (1997). Timing of the North-South China collision from new middle to late Mesozoic paleomagnetic data from the North China Block. *Journal of Geophysical Research: Solid Earth, 102*(B8), 17713-17727.
GOMI, T., & SIDLE, R. C. (2003). Bed load transport in managed steep-gradient headwater streams of southeastern Alaska. *Water Resources Research, 39*(12).
HAY, D. C., & DEMPSTER, T. J. (2009). Zircon behaviour during low-temperature metamorphism. *Journal of petrology, 50*(4), 571-589.
HOLLAND, T. J. B., & POWELL, R. (2011). An improved and extended internally consistent thermodynamic dataset for phases of petrological interest, involving a new equation of state for solids *J. Metamorph. Geol.* (Vol. 29, pp. 333-383).
HONG, Z. (2008). The Chronological Study on U–Pb Dating of Modern River Detrital Zircon in North Piedmont of Qinling and Its Geological Indication. *Master's Degree Thesis of Northwest University, Xi'an, China*, 1-138.
HU, J., CUI, J., MENG, Q., & ZHAO, C. (2004). The U–Pb Age of zircons separated from the Zhashui granite in Qinling Orogen and its significance. *Geological Review, 50*(3), 323-329.
HUJUN, G., LAIMIN, Z., BOYA, S., BEN, L., & BO, G. (2009). Zircon U-Pb ages and Hf isotope characteristics and their geological significance of the Shahewan, Caoping and Zhashui granitic plutons in the South Qinling orogen. *Acta Petrologica Sinica, 25*(2), 248-264.
JANOTS, E., BERGER, A., GNOS, E., WHITEHOUSE, M., LEWIN, E., & PETTKE, T. (2012). Constraints on fluid evolution during metamorphism from U–Th–Pb systematics in Alpine hydrothermal monazite. *Chemical Geology, 326*, 61-71.
JANOTS, E., ENGI, M., BERGER, A., ALLAZ, J., SCHWARZ, J. O., & SPANDLER, C. (2008). Prograde metamorphic sequence of REE minerals in pelitic rocks of the Central Alps: implications for allanite–monazite–xenotime phase relations from 250 to 610 C. *Journal of Metamorphic Geology, 26*(5), 509-526.
JIANG, S., NIE, F., FANG, D., LIU, Y., ZHANG, W., XU, D., & ZHANG, Z. (2009). Geochronology of major gold and silver deposits in Weishancheng area, Tongbai County, Henan Province. *Mineral Deposits, 1*, 007.
KELSEY, D. E., & HAND, M. (2015). On ultrahigh temperature crustal metamorphism: phase equilibria, trace element thermometry, bulk composition, heat sources, timescales and tectonic settings. *Geoscience Frontiers, 6*(3), 311-356.
KRÖNER, A., ZHANG, G. W., & SUN, Y. (1993). Granulites in the Tongbai area, Qinling belt, China: geochemistry, petrology, single zircon geochronology, and implications for the tectonic evolution of eastern Asia. *Tectonics, 12*(1), 245-255.
LAI, S. C., & QIN, J. F. (2010). Zircon U–Pb dating and Hf isotopic composition of the diabase dike swarm from Sanchazi area, Mianlue suture: chronology evidence for the Paleo-Tethys oceanic crust subduction. *J. Earth Sci. Environ, 32*, 27-33.
LENZI, M. A., MAO, L., & COMITI, F. (2004). Magnitude-frequency analysis of bed load data in an Alpine boulder bed stream. *Water Resources Research, 40*(7).
LI, H.-Y., HE, B., XU, Y.-G., & HUANG, X.-L. (2010). U–Pb and Hf isotope analyses of detrital zircons from Late Paleozoic sediments: insights into interactions of the North China Craton with surrounding plates. *Journal of Asian Earth Sciences, 39*(5), 335-346.
LI, Y., ZHOU, H.-W., LI, Q.-L., XIANG, H., ZHONG, Z.-Q., & BROUWER, F. M. (2014). Palaeozoic polymetamorphism in the North Qinling orogenic belt, Central China: Insights from petrology and in situ titanite and zircon U-Pb geochronology. *Journal of Asian Earth Sciences, 92*, 77.
LI, Y., ZHOU, H. W., ZHONG, Z. Q., XIANG, H., ZENG, W., QI, D. M., & ZHANG, L. (2012). Two Eopaleozoic metamorphic events in North Qinling: petrology and zircon U–Pb

geochronology evidences from basic rocks in the Songshugou area. *Earth Science, 37*(Suppl 1), 111-124.

LIAO, X., LIU, L., WANG, Y., CAO, Y., CHEN, D., & DONG, Y. (2016). Multi-stage metamorphic evolution of retrograde eclogite with a granulite-facies overprint in the Zhaigen area of the North Qinling Belt, China. *Gondwana Research, 30*, 79-96. doi:http://dx.doi.org/10.1016/j.gr.2015.09.012

LIU, J., & ZHANG, L. (2013). Neoproterozoic low to negative δ 18 O volcanic and intrusive rocks in the Qinling Mountains and their geological significance. *Precambrian Research, 230*, 138-167.

LIU, L., CHEN, D. L., SUN, Y., ZHANG, A. D., & LUO, J. H. (2003). *Discovery of relic majoritic garnet in felsic metamorphic rocks of Qinling complex, north Qinling orogenic belt, China.* Paper presented at the Alice Wain Memorial Western Norway Eclogite Field Symposium. Selje, Western Noway, Abstract.

LIU, L., LIAO, X., WANG, Y., WANG, C., SANTOSH, M., YANG, M., . . . CHEN, D. (2016). Early Paleozoic tectonic evolution of the North Qinling Orogenic Belt in Central China: Insights on continental deep subduction and multiphase exhumation. *Earth-Science Reviews, 159*, 58-81.

LIU, L., LIAO, X. Y., ZHANG, C. L., CHEN, D. L., GONG, X. K., & KANG, L. (2013). Multi-metamorphic timings of HP-UHP rocks in the North Qinling and their geological implications. *Acta Petrologica Sinica, 29*(5), 1634-1656.

LIU, L., YANG, J., CHEN, D., WANG, C., ZHANG, C., YANG, W., & CAO, Y. (2010). Progress and controversy in the study of HP-UHP metamorphic terranes in the West and Middle Central China orogen. *Journal of Earth Science, 21*, 581-597.

LIU, X. C., JAHN, B. M., HU, J., LI, S. Z., LIU, X., & SONG, B. (2011). Metamorphic patterns and SHRIMP zircon ages of medium-to-high grade rocks from the Tongbai orogen, central China: implications for multiple accretion/collision processes prior to terminal continental collision. *Journal of Metamorphic Geology, 29*(9), 979-1002.

LU, S., CHEN, Z., & XIANG, Z. (2006). U-Pb ages of detrital zircons from the para-metamorphic rocks of the Qinling Group and their geological significance. *Earth Science Frontiers, 13*(6), 303.

LU, S., LI, H., CHEN, Z., HAO, G., ZHOU, H., GUO, J., . . . XIANG, Z. (2003). Meso-Neoproterozoic geological evolution in the Qinling orogeny and its response to the supercontinental events of Rodinia. *Geol Publish House, Beijing*, 1-194.

LU, Y. H., ZHAO, Z. F., & ZHENG, Y. F. (2016). Geochemical constraints on the source nature and melting conditions of Triassic granites from South Qinling in central China. *LITHOS, 264*, 141-157. doi:http://dx.doi.org/10.1016/j.lithos.2016.08.018

LUX, D. R., DEYOREO, J. J., GULDOTTI, C. V., & DECKER, E. R. (1986). Role of plutonism in low-pressure metamorphic belt formation.

MAO, L., & LENZI, M. A. (2007). Sediment mobility and bedload transport conditions in an alpine stream. *Hydrological processes, 21*(14), 1882-1891.

MATTAUER, M., MATTE, P., MALAVIEILLE, J., TAPPONNIER, P., MALUSKI, H., QIN, X. Z., . . . QIN, T. Y. (1985). Tectonics of the Qinling belt: build-up and evolution of eastern Asia. *Nature, 317*(6037), 496-500.

MENG, Q.-R., & ZHANG, G.-W. (1999). Timing of collision of the North and South China blocks: controversy and reconciliation. *Geology, 27*(2), 123-126.

MENG, Q.-R., & ZHANG, G.-W. (2000). Geologic framework and tectonic evolution of the Qinling orogen, central China. *Tectonophysics, 323*(3), 183-196.

MORRISSEY, L. J., HAND, M., & KELSEY, D. E. (2015). Multi-stage metamorphism in the Rayner–Eastern Ghats Terrane: P–T–t constraints from the northern Prince Charles Mountains, east Antarctica. *Precambrian Research*. doi:10.1016/j.precamres.2015.06.003

NUTMAN, A. P., BUCKMAN, S., HIDAKA, H., KAMIICHI, T., BELOUSOVA, E., & AITCHISON, J. (2013). Middle Carboniferous-Early Triassic eclogite–blueschist blocks within a serpentinite mélange at Port Macquarie, eastern Australia: Implications for the evolution of Gondwana's eastern margin. *Gondwana Research, 24*(3), 1038-1050.

PATON, C., HELLSTROM, J., PAUL, B., WOODHEAD, J., & HERGT, J. (2011). Iolite: Freeware for the visualisation and processing of mass spectrometric data. *Journal of Analytical Atomic Spectrometry, 26*(12), 2508-2518.

PATTISON, D. R. M., & TINKHAM, D. K. (2009). Interplay between equilibrium and kinetics in prograde metamorphism of pelites: an example from the Nelson aureole, British Columbia. *Journal of Metamorphic Geology, 27*(4), 249-279.
PAYNE, J. L., HAND, M., BAROVICH, K. M., & WADE, B. P. (2008). Temporal constraints on the timing of high-grade metamorphism in the northern Gawler Craton: implications for assembly of the Australian Proterozoic. *An International Geoscience Journal of the Geological Society of Australia, 55*(5), 623-640. doi:10.1080/08120090801982595
PEARCE, M. A., WHITE, A. J. R., & GAZLEY, M. F. (2015). TCInvestigator: automated calculation of mineral mode and composition contours for thermocalc pseudosections. *Journal of Metamorphic Geology, 33*(4), 413-425. doi:10.1111/jmg.12126
POWELL, R., WHITE, R., GREEN, E., HOLLAND, T. J. B., & DIENER, J. F. A. (2014). On parameterizing thermodynamic descriptions of minerals for petrological calculations. *Journal of Metamorphic Geology, 32*(3), 245-260.
PRICE, J. R., VELBEL, M. A., & PATINO, L. C. (2005). Rates and time scales of clay-mineral formation by weathering in saprolitic regoliths of the southern Appalachians from geochemical mass balance. *Geological Society of America Bulletin, 117*(5-6), 783-794.
QIAN, J. H., XIUQING, Y., LIANG, L., YUTING, C., DANLING, C., & WENQIANG, Y. (2013). Zircon U-Pb dating, mineral inclusions, Lu-Hf isotopic data and their geological significance of garnet amphibolite from Songshugou, North Qinling. *Acta Petrologica Sinica, 29*(9), 3087-3098.
RATSCHBACHER, L., HACKER, B. R., CALVERT, A., WEBB, L. E., GRIMMER, J. C., MCWILLIAMS, M. O., . . . HU, J. (2003). Tectonics of the Qinling (Central China): tectonostratigraphy, geochronology, and deformation history. *Tectonophysics, 366*(1), 1-53.
RUBATTO, D., CHAKRABORTY, S., & DASGUPTA, S. (2013). Timescales of crustal melting in the Higher Himalayan Crystallines (Sikkim, Eastern Himalaya) inferred from trace element-constrained monazite and zircon chronology. *Contributions to Mineralogy and Petrology, 165*(2), 349-372.
RUBATTO, D., WILLIAMS, I. S., & BUICK, I. S. (2001). Zircon and monazite response to prograde metamorphism in the Reynolds Range, central Australia. *Contributions to Mineralogy and Petrology, 140*(4), 458-468.
SCHNEIDER, J. M., RICKENMANN, D., TUROWSKI, J. M., BUNTE, K., & KIRCHNER, J. W. (2015). Applicability of bed load transport models for mixed-size sediments in steep streams considering macro-roughness. *Water Resources Research, 51*(7), 5260-5283.
SEYDOUX-GUILLAUME, A.-M., MONTEL, J.-M., BINGEN, B., BOSSE, V., DE PARSEVAL, P., PAQUETTE, J.-L., . . . WIRTH, R. (2012). Low-temperature alteration of monazite: Fluid mediated coupled dissolution–precipitation, irradiation damage, and disturbance of the U–Pb and Th–Pb chronometers. *Chemical Geology, 330*, 140-158.
SHI, Y., YU, J.-H., & SANTOSH, M. (2013). Tectonic evolution of the Qinling orogenic belt, Central China: New evidence from geochemical, zircon U–Pb geochronology and Hf isotopes. *Precambrian Research, 231*, 19-60. doi:10.1016/j.precamres.2013.03.001
SIRCOMBE, K. N. (1999). Tracing provenance through the isotope ages of littoral and sedimentary detrital zircon, eastern Australia. *Sedimentary Geology, 124*(1), 47-67.
SMITH, H. A., & BARREIRO, B. (1990). Monazite U-Pb dating of staurolite grade metamorphism in pelitic schists. *Contributions to Mineralogy and Petrology, 105*(5), 602-615.
SONG, C., ZHANG, G. W., WANG, Y. S., LI, J. H., CHEN, Z. C., & CAI, Z. C. (2009). The constraints of strain partitioning and geochronology in Luonan-Luanchuan tectonic belts on Qinling orogenic belt. *Science in China Series D: Earth Sciences, 52*(3), 300-312.
SPEAR, F. S. (1993). Metamorphic phase equilibria and pressure-temperature-time paths. *Monograph, Mineralogical Society of America, Washington, D.C.*
SPEAR, F. S., & PYLE, J. M. (2002). Apatite, monazite, and xenotime in metamorphic rocks. *Reviews in mineralogy and geochemistry, 48*(1), 293-335.
SPEAR, F. S., PYLE, J. M., & CHERNIAK, D. (2009). Limitations of chemical dating of monazite. *Chemical Geology, 266*(3), 218-230.
STÜWE, K. (2007). *Geodynamics of the lithosphere: an introduction*: Springer Science & Business Media.

SU, L., SHUGUANG, S., BIAO, S., DINGWU, Z., & JIANRONG, H. (2004). SHRIMP zircon U-Pb ages of garnet pyroxenite and Fushui gabbroic complex in Song-shugou region and constraints on tectonic evolution of Qinling Orogenic belt. *Chinese Science Bulletin, 49*(12), 1307-1310.

SUN, W., LI, S., CHEN, Y., & LI, Y. (2000). Zircon U–Pb dating of granitoids from South Qinling, Central China and their geological significance. *Geochimica, 29*(3), 209-216.

SUN, W., LI, S., SUN, Y., ZHANG, G., & LI, Q. (2002a). Mid-paleozoic collision in the north Qinling: Sm–Nd, Rb–Sr and 40 Ar/39 Ar ages and their tectonic implications. *Journal of Asian Earth Sciences, 21*(1), 69-76.

SUN, Y., LU, X., & HAN, S. (1996). Composition and formation of Palaeozoic Erlangping ophiolitic slab, North Qinling: evidence from geology and geochemistry. *中国科学D 辑(英文版)*, S1.

SUZUKI, K., & KATO, T. (2008). CHIME dating of monazite, xenotime, zircon and polycrase: protocol, pitfalls and chemical criterion of possibly discordant age data. *Gondwana Research, 14*(4), 569-586.

SYMMES, G. H., & FERRY, J. M. (1995). Metamorphism, fluid flow and partial melting in pelitic rocks from the Onawa contact aureole, central Maine, USA. *Journal of petrology, 36*(2), 587-612.

TANG, L., SANTOSH, M., & DONG, Y. (2015). Tectonic evolution of a complex orogenic system: Evidence from the northern Qinling belt, Central China. *Journal of Asian Earth Sciences*. doi:10.1016/j.jseaes.2015.03.033

TANG, L., SANTOSH, M., DONG, Y., TSUNOGAE, T., ZHANG, S., & CAO, H. (2016). Early Paleozoic tectonic evolution of the North Qinling orogenic belt: Evidence from geochemistry, phase equilibrium modeling and geochronology of metamorphosed mafic rocks from the Songshugou ophiolite. *Gondwana Research*. doi:10.1016/j.gr.2014.10.006

TAO, W., XIAOXIA, W., GUOWEI, Z., XIANZHI, P., & CHENGLI, Z. (2003). Remnants of a Neoproterozoic collisional orogenic belt in the core of the Phanerozoic Qinling orogenic belt (China). *Gondwana Research, 6*(4), 699-710.

TAYLOR, R. J., KIRKLAND, C. L., & CLARK, C. (2016). Accessories after the facts: Constraining the timing, duration and conditions of high-temperature metamorphic processes. *LITHOS, 264*, 239-257.

THOMPSON, C., & CROKE, J. (2008). Channel flow competence and sediment transport in upland streams in southeast Australia. *Earth Surface Processes and Landforms, 33*(3), 329-352.

TUCKER, N. M., HAND, M., KELSEY, D. E., & DUTCH, R. A. (2015). A duality of timescales: Short-lived ultrahigh temperature metamorphism preserving a long-lived monazite growth history in the Grenvillian Musgrave–Albany–Fraser Orogen. *Precambrian Research, 264*, 204-234. doi:10.1016/j.precamres.2015.04.015

VERNON, R. H., & CLARKE, G. L. (2008). *Principles of metamorphic petrology*: Cambridge University Press.

WANG, H., WU, Y.-B., GAO, S., LIU, X.-C., LIU, Q., QIN, Z.-W., . . . YANG, S.-H. (2013). Continental origin of eclogites in the North Qinling terrane and its tectonic implications.(Report). *Precambrian Research, 230*, 13.

WANG, H., WU, Y.-B., GAO, S., ZHENG, J.-P., LIU, Q., LIU, X.-C., . . . GONG, H.-J. (2014). Deep subduction of continental crust in accretionary orogen: Evidence from U-Pb dating on diamond-bearing zircons from the Qinling orogen, central China.(Author abstract). *LITHOS, 190 191*, 420.

WANG, H., WU, Y. B., GAO, S., LIU, X. C., GONG, H. J., LI, Q. L., . . . YUAN, H. L. (2011). Eclogite origin and timings in the North Qinling terrane, and their bearing on the amalgamation of the South and North China Blocks. *Journal of Metamorphic Geology, 29*(9), 1019-1031. doi:10.1111/j.1525-1314.2011.00955.x

WANG, J., DENG, Q., WANG, Z.-J., QIU, Y.-S., DUAN, T.-Z., JIANG, X.-S., & YANG, Q.-X. (2013). New evidences for sedimentary attributes and timing of the “Macaoyuan conglomerates” on the northern margin of the Yangtze block in southern China. *Precambrian Research, 235*, 58-70.

WANG, L., GRIFFIN, W. L., YU, J. H., & O'REILLY, S. Y. (2013). U–Pb and Lu–Hf isotopes in detrital zircon from Neoproterozoic sedimentary rocks in the northern Yangtze Block: implications for Precambrian crustal evolution. *Gondwana Research, 23*(4), 1261-1272.

WANG, L. J., YU, J. H., GRIFFIN, W. L., & O'REILLY, S. Y. (2012). Early crustal evolution in the western Yangtze Block: evidence from U–Pb and Lu–Hf isotopes on detrital zircons from sedimentary rocks. *Precambrian Research, 222*, 368-385.

WHITE, R., POWELL, R., & JOHNSON, T. (2014a). The effect of Mn on mineral stability in metapelites revisited: New a–x relations for manganese-bearing minerals. *Journal of Metamorphic Geology, 32*(8), 809-828.

WHITE, R. W., POWELL, R., HOLLAND, T. J. B., JOHNSON, T. E., & GREEN, E. C. R. (2014b). New mineral activity–composition relations for thermodynamic calculations in metapelitic systems. *Journal of Metamorphic Geology, 32*(3), 261-286.

WING, B. A., FERRY, J. M., & HARRISON, T. M. (2003). Prograde destruction and formation of monazite and allanite during contact and regional metamorphism of pelites: petrology and geochronology. *Contributions to Mineralogy and Petrology, 145*(2), 228-250.

XIANG, H., ZHANG, L., ZHONG, Z., SANTOSH, M., ZHOU, H., ZHANG, H., . . . ZHENG, S. (2012). Ultrahigh-temperature metamorphism and anticlockwise P-T-t path of Paleozoic granulites from north Qinling-Tongbai Orogen, central China. *Gondwana Research, 21*(2), 559-576. doi:10.1016/j.gr.2011.07.002

YAN, Q. R., WANG, Z. Q., YAN, Z., WANG, T., CHEN, J. L., XIANG, Z. J., . . . JIANG, C. F. (2008). Origin, age and tectonic implications of metamafic rocks in the Kuanping Group of the Qinling orogenic belt, China. *Geological Bulletin of China, 27*(9), 1475-1492.

YAN, Z., FU, C., WANG, Z., YAN, Q., CHEN, L., & CHEN, J. (2016). Late Paleozoic subduction–accretion along the southern margin of the North Qinling terrane, central China: Evidence from zircon U-Pb dating and geochemistry of the Wuguan Complex. *Gondwana Research, 30*, 97-111. doi:http://dx.doi.org/10.1016/j.gr.2015.05.005

YAN, Z., WANG, Z., CHEN, J., YAN, Q., & WANG, T. (2010). Detrital record of Neoproterozoic arc-magmatism along the NW margin of the Yangtze Block, China: U–Pb geochronology and petrography of sandstones. *Journal of Asian Earth Sciences, 37*(4), 322-334.

YAN, Z., WANG, Z., CHEN, J., YAN, Q., WANG, T., & ZHANG, Y. (2009). Geochemistry and SHRIMP zircon U–Pb dating of amphibolites from the Danfeng Group in the Wuguan area, North Qinling terrane and their tectonic significance. *Acta Geologica Sinica, 84*, 1633-1646.

YANG, C. H., WEI, C. J., ZHANG, S. G., LI, H. M., WAN, Y. S., & LI, R. S. (1999). U–Pb zircon dating of granulite facies rocks from the Foping area in the southern Qinling mountains. *Geological Review, 45*(2), 173-179.

YANG, J., LIU, F., WU, C., XU, Z., SHI, R., CHEN, S., . . . WOODEN, J. (2005). Two Ultrahigh-Pressure Metamorphic Events Recognized in the Central Orogenic Belt of China: Evidence from the U-Pb Dating of Coesite-Bearing Zircons. *International Geology Review, 47*(4), 327-343. doi:10.2747/0020-6814.47.4.327

YANG, J., XU, Z., DOBRZHINETSKAYA, L. F., GREEN, H. W., PEI, X., SHI, R., . . . LI, H. (2003). Discovery of metamorphic diamonds in central China: an indication of a >4000-km-long zone of deep subduction resulting from multiple continental collisions. *Terra Nova, 15*(6), 370-379. doi:10.1046/j.1365-3121.2003.00511.x

YANG, W., YANG, J., WANG, X., & DU, Y. (2014). Uplift-denudation history of the Qinling orogen: Constrained from the detrital-zircon U–Pb geochronology. *Journal of Asian Earth Sciences, 89*, 54-65.

YANG, Z., DONG, Y., LIU, X., & ZHANG, J. (2006). LA-ICP-MS zircon U-Pb dating of gabbro in the Guanzizhen ophiolite, Tianshui, West Qinling. *Geological Bulletin of China, 25*, 1321-1325.

YIN, C., LIN, S., DAVIS, D. W., XING, G., DAVIS, W. J., CHENG, G., . . . LI, L. (2013). Tectonic evolution of the southeastern margin of the Yangtze Block: Constraints from SHRIMP U-Pb and LA-ICP-MS Hf isotopic studies of zircon from the eastern Jiangnan Orogenic Belt and implications for the tectonic interpretation of South China. *Precambrian Research, 236*, 145-156.

YOU, Z. D., SUO, S. T., HAN, Y. J., ZHONG, Z. Q., & CHEN, N. S. (1991). The Metamorphic Progresses and Tectonic Analyses in the Core Complex of an Orogenic Belt: An Example From the Eastern Qinling Mountains. *China University of Geosciences, Wuhan*, 1-326.

YU, S., JINHAI, Y., XISHENG, X., JIANSHENG, Q., & LIHUI, C. (2009). Geochronology and geochemistry of the Qinling Group in the eastern Qinling Orogen. *Acta Petrologica Sinica, 25*(10), 2651-2670.

YU, S., LI, S., ZHAO, S., CAO, H., & SUO, Y. (2015). Long history of a Grenville orogen relic the North Qinling Terrane evolution of the Qinling orogenic belt from Rodinia to Gondwana. *Precambrian Research, 271*, 98-117. doi:10.1016/j.precamres.2015.09.020

YUSHENG, W., DUNYI, L., CHUNYAN, D., & XIAOYAN, Y. (2011). SHRIMP zircon dating of meta-sedimentary rock from the Qinling Group in the north of Xixia, North Qinling Orogenic Belt: constraints on complex histories of source region and timing of deposition and metamorphism. *Acta Petrologica Sinica, 27*(4), 1172-1178.

ZHAI, X., DAY, H. W., HACKER, B. R., & YOU, Z. (1998). Paleozoic metamorphism in the Qinling orogen, Tongbai Mountains, central China. *Geology, 26*(4), 371-374. doi:10.1130/0091-7613(1998)026<0371:pmitqo>2.3.co;2

ZHANG, C. L., ZHANG, G. W., & LU, X. X. (1994). Characteristics and origin of Kuanping granite body in the East Qinling. *Northwest Geoscience, 15*(1), 27-34.

ZHANG, G. W., ZHANG, B. R., YUAN, X. C., & XIAO, Q. H. (2001). Qinling Orogenic Belt and Continental Dynamics. *Science Press, Bejing*, 1-855.

ZHANG, H., YE, R. S., LIU, B. X., WANG, Y., ZHANG, Y. S., SIEBEL, W., & CHEN, F. (2016). Partial melting of the South Qinling orogenic crust, China: Evidence from Triassic migmatites and diorites of the Foping dome. *LITHOS, 260*, 44-57. doi:http://dx.doi.org/10.1016/j.lithos.2016.05.007

ZHANG, J. X., YU, S. Y., & MENG, F. C. (2011). Polyphase Early Paleozoic metamorphism in the northern Qinling orogenic belt. *Acta Petrologica Sinica, 27*, 1179-1190.

ZHANG, R., LIOU, J., & ERNST, W. G. (2007). Ultrahigh-Pressure Metamorphic Belts in China: Major Progress in the Past Several Years. *International Geology Review, 49*(6), 504-519. doi:10.2747/0020-6814.49.6.504

ZHANG, Z., & ZHANG, Q. (1995). Geochemistry of metamorphosed late Proterozoic Kuanping ophiolite in the northern Qinling, China. *Acta Petrologica Sinica (in Chinese), 11*.

ZHAO, S., LI, S., LIU, X., SANTOSH, M., SOMERVILLE, I. D., CAO, H., . . . GUO, L. (2015). The northern boundary of the Proto-Tethys Ocean: Constraints from structural analysis and U–Pb zircon geochronology of the North Qinling Terrane. *Journal of Asian Earth Sciences, 113, Part 2*, 560-574. doi:http://dx.doi.org/10.1016/j.jseaes.2015.09.005

ZHU, X., CHEN, F., LI, S., YANG, Y., NIE, H., SIEBEL, W., & ZHAI, M. (2011). Crustal evolution of the North Qinling Terrain of the Qinling Orogen, China: evidence from detrital zircon U/Pb ages and Hf isotopic composition. *Gondwana Research, 20*(1), 194-204. doi:10.1016/j.gr.2010.12.009

ZHU, X., CHEN, F., NIE, H., SIEBEL, W., YANG, Y., XUE, Y., & ZHAI, M. (2014). Neoproterozoic tectonic evolution of South Qinling, China: evidence from zircon ages and geochemistry of the Yaolinghe volcanic rocks. *Precambrian Research, 245*, 115-130.

APPENDIX A: Sample Petrography

QL-2

Matrix minerals consists of; biotite (~70–100 µm), muscovite (~100–300 µm), quartz (~50–400 µm) and plagioclase (50–100 µm).Biotite and muscovite define a pervasive fabric. Poikiloblastic cordierite (1100–2500 µm) contains abundant inclusions of matrix minerals, but is completely pinitized (<10 µm) (Appendix Fig. 1, c, d). The longest axis of cordierite grains are commonly aligned to the pervasive foliation. Inclusions in cordierite are variously oriented matrix minerals, some of which align parallel to the dominant foliation. Some cordierite grains are partially mantled by coarse quartz (Appendix Fig. 1, c). Less common muscovite grains occur oblique to perpendicular to the main foliation (Appendix Fig. 1, d). Accessory minerals include zircon and monazite. Rutile is uncommon and occurs mainly in the matrix, but also less commonly as inclusions in cordierite. The interpreted peak assemblage is cordierite + biotite + muscovite + quartz + plagioclase + rutile and the muscovite oriented at an oblique angle to the main foliation is interpreted as retrograde.

QL-3

Matrix minerals consist of; biotite (50–100 µm), muscovite (50–300 µm), quartz (30–100 um), coarse rutile (40–300 µm), chlorite (<50 µm) and plagioclase (<100 µm). Biotite, chlorite and muscovite define a pervasive foliation. Poikiloblastic cordierite (~1100 µm) contains abundant inclusions of matrix minerals, but is completely pinitized. The foliation defined by biotite, chlorite and muscovite wraps around cordierite poikiloblasts. Cordierite contains abundant inclusions of matrix minerals. The inclusions are oriented parallel to the external/matrix foliation as well as oblique to it. In the matrix, less commonly biotite occurs oblique to the main fabric. Large (up to 400 µm) muscovite grains perpendicular to the main fabric occur in cordierite. Fine grained chlorite occurs at the boundary between cordierite and the matrix. The interpreted peak assemblage is cordierite + biotite + muscovite + plagioclase + quartz + rutile. Obliquely and perpendiculariy oriented muscovite and biotite, as well as chlorite, are interpreted as retrograde origin.

2QS2

The matrix consists of; biotite (50–200 µm), muscovite (100–700 µm), quartz (50–100 µm), rutile (10–150 µm), feldspar (<50 µm) and chlorite (~100 µm). Multiple fabrics (up to 4, by muscovite) are commonly defined by muscovite. Both biotite and muscovite form the main fabric. Poikiloblastic cordierite (2000–10,000 µm) is wholly pinitized and contains abundant inclusions of matrix minerals and rutile. Cordierite has no preferred orientation. Bands of aggregate muscovite strongly wrap around cordierite. Muscovite is commonly observed with orientations oblique to perpendicular to other fabrics. Poikiloblastic andalusite porphyroblasts occur in close proximity to cordierite, but separated from cordierite commonly by matrix chlorite and rutile. Fine-grained (<30 µm) inclusions in andalusite are biotite and quartz with larger (up to 80 µm) rutile. The peak assemblage is interpreted to be cordierite + andalusite + biotite + muscovite + chlorite + quartz + plagioclase + rutile. Obliquely and perpendicularly oriented muscovite and biotite are interpreted as retrograde origin.

4QS4

The matrix consists of; biotite (50–200 µm), muscovite (50–300 µm), quartz (30–100 µm), and feldspar (<100 µm). Biotite and muscovite define a pervasive fabric. Poikiloblatic cordierite (~1000–2000 µm) and andalusite (up to 700 µm) are abundant. Fresh cordierite is preserved; however it is commonly pinitized. Cordierite contains inclusions of matrix grains commonly oriented parallel to the main matrix fabric. The long axis of cordierite grains is commonly aligned with the surrounding matrix foliation. Cordierite is partially to completely mantled by poikiloblastic andalusite, which contains inclusions of ilmenite (predominantly: up to 100 µm) as well as quartz and biotite which are finer grained compared to the matrix grains. Matrix ilmenite occurs as a common contact with andalusite often on its margins (some as large as 200 µm) and as common inclusions in its core regions. The fabric defined by matrix biotite and muscovite warp cordierite and andalusite poikiloblasts. Andalusite poikolblasts are commonly surrounded by dense aggregates of biotite. Some muscovite grains occur oblique to perpendicular to the main fabric. The peak assemblage is interpreted to be cordierite + andalusite + biotite + muscovite + quartz + plagioclase + ilmenite. Obliquely and perpendicularly oriented muscovite is interpreted to be retrograde in origin.

Appendix Figure 1: (A) Atoll of cordierite, showing an inclusion filled core consisting dominantly of biotite and quartz; (B) Poikiloblastic cordierite with coarse cross-cutting muscovite (mu2), inclusions of biotite, quartz and muscovite; (C) Poikiloblastic cordierite locally mantled by chlorite; (D) Cross polarised light (XPL) image: comparison between pinitised cordierite and matrix. A second generation of muscovite (mu_2) is perpendicular to main fabric. Localised radial orientation of mu_3 occurs in the matrix. More closely, the occurrence of chlorite at the margins of cordierite is observed; (E) Cordierite separated from andalusite by chlorite. Andalusite contains abundant (relatively coarse with respect to adjacent external grains) ilmenite inclusions; (F) Multiple orientations of late stage chlorite which is perpendicular to the main fabric; (G) Cross polarised light (XPL) image: biotite mantles andalusite which surrounds poikiloblastic. Cordierite contains abundant matrix minerals; (H) Andalusite surrounds cordierite and is mantled by biotite;

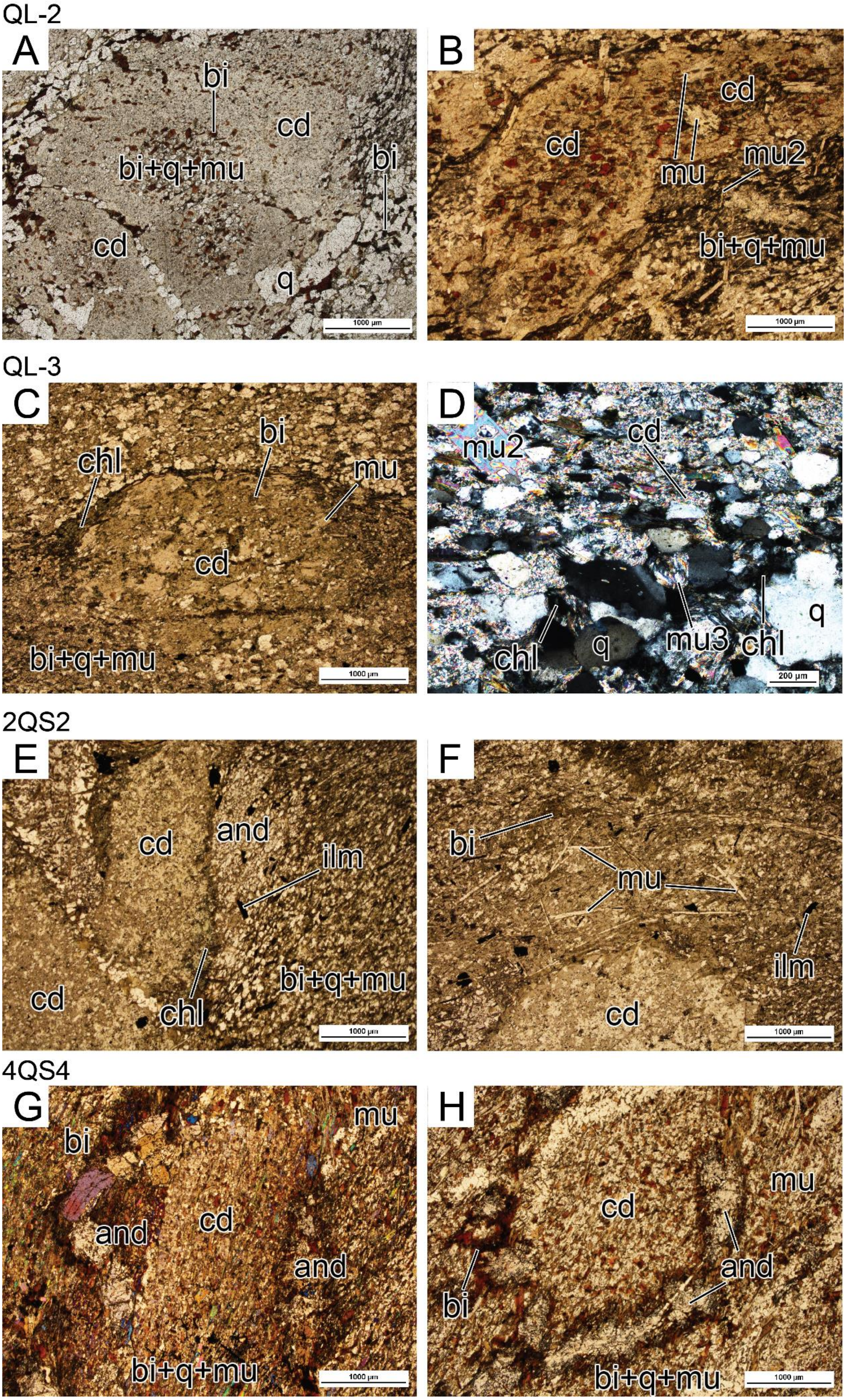
QL-2
A
bi
cd
bi+q+mu
bi
cd
q
1000 µm
B
cd
cd
mu
mu2
bi+q+mu
1000 µm
QL-3
C
bi
chl
mu
cd
bi+q+mu
1000 µm
D
mu2
cd
q
chl
q
mu3
chl
200 µm
2QS2
E
cd
and
ilm
bi+q+mu
cd
chl
1000 µm
F
bi
mu
ilm
cd
1000 µm
4QS4
G
mu
bi
and
cd
and
bi+q+mu
1000 µm
H
mu
cd
and
bi
bi+q+mu
1000 µm

APPENDIX B: Geomorphological analysis of schist boulder provenance

The probable source and total displacement of schist samples occurring as boulders in mountain stream settings within the NQB are constrained by the integration of several key observations and data. These include: (i) the known origin of the streams and drainage divide of the river system with respect to the known geology (Fig. 1c); (ii) the hydrological processes influencing bedload transport and (iii) weathering rates of comparable rock-types. The conclusions derived from this analysis are discussed further in subsequent sections outlining U–Pb zircon geochronology of the schists, and comparison between monazite ages from the schists and known tectono-thermal events within the framework of the QOB.

(i) Both sample locations are within northward flowing streams, Fig.1c. To the west, the drainage divide for north-flowing drainage systems occurs in the northernmost SQB (Fig.1c). The headwaters of rivers that flow past sample locations 1a and 1b are located within the Middle–Upper Devonian Liuling Group sediments, intruded by Early–Mesozoic to Late–Triassic dikes and granitoids respectively (Zhang et al., 2016). The headwaters of rivers that flow past sample location 2 occur within the Mesoproterozoic–Early Neoproterozoic Qinling Group, which is intruded by Palaeozoic granitoids (e.g. Dong et al., 2013).

(ii) Lenzi et al. (2004) reports two groups of colour-marked samples up to boulder size (diameter (D) = >5 cm to <90 cm) which were monitored in the instance of a single flood event in an alpine stream setting. Distances transported range between 1 m and 170 m. Of relevance to the schist boulders of this study, which range in size between ~8×12 cm to ~25×15 cm (Table 2), the majority of samples with D = >10 cm in Lenzi et al. (2004) were not displaced more than 100 m and samples for the class size of 15.2 cm did not move more than 24 m. Mao and Lenzi (2007) discuss a decrease in particle displacement with increasing sediment size, at conditions greater than D = 10 cm and displacement about < 100 m. Similarly, Church and Hassan (1992) concur with superficial bedload mobility being a result of size dependence. Through experimental field data of mixed bedload grain size, it is common that tracer clasts become trapped amongst coarser clasts and in areas of bedload roughness e.g. step-pools and rapids (e.g. Church & Hassan, 1992; Lenzi et al., 2004; Schneider et al., 2015). Material larger than coarse gravel requires ‘event’ scale floods (such as >1:10 to 1:50 year return period) to cause mobility (Gomi & Sidle, 2003; Mao & Lenzi, 2007; Thompson & Croke, 2008). Whereas it is not possible to constrain exactly how long boulders examined in this study have been in the streams, and therefore the total distance travelled, the published empirical studies cited here can be used to argue that mobility of the schist boulders was most likely limited by entrapment amongst coarse bedload material (granites ≥30 cm to 2 m, occupying ≥99% of bedload, Fig. 2) to ≤10 km, rather substantially greater than this estimate.

(iii) On the basis that schist samples in this study are effectively unweathered (except for pinitised cordierite), inferences can be made to the likely residence time and approximate distance travelled in stream settings. Although empirical data on weathering rates of minerals is scarce, weathering to clay assemblages is thought to occur between 2 k.y. to 2 m.y. with mean values of 50 k.y. to 1 m.y (e.g. Price et al., 2005). It is therefore reasonable to infer that samples in this study do not have a long residence time in the streams, and in combination with (i) and (ii), have probably travelled a maximum distance of the order of ~10 km.

APPENDIX C: Whole-rock geochemistry

Whole-rock geochemical analyses for samples QL-1, QL-2, QL-3, 2QS2, 4QS4 and CQ38S1 (Table below) were undertaken by Wavelength Dispersive X-ray Fluorescence spectrometry at the Department of Earth and Environment, Franklin and Marshall College, Lancaster PA, USA. Major elements were analysed on fused disks prepared using a lithium tetraborate flux.

Appendix Table 1: Whole rock geochemistry (in wt. %). Fe_2O_3T is total iron represented as ferric iron.

Sample	CQ38S1	QL – 1	QL – 2	QL – 3	2QS2	4QS4
SiO_2	63.58	56.11	65.15	69.19	62.46	64.53
TiO_2	0.80	0.95	0.80	0.80	0.81	0.77
Al_2O_3	16.08	20.47	17.17	15.57	19.62	18.41
Fe_2O_3T	8.71	8.25	7.14	6.05	7.51	7.21
MnO	0.26	0.08	0.11	0.06	0.11	0.09
MgO	3.74	6.30	3.59	2.83	3.68	3.40
CaO	1.03	0.50	0.90	0.42	0.51	0.35
Na_2O	1.10	3.20	1.61	1.45	0.69	1.16
K_2O	4.25	3.59	3.37	3.42	4.37	3.82
P_2O_5	0.20	0.27	0.19	0.17	0.20	0.16
Total	**99.75**	**99.72**	**100.03**	**99.96**	**99.96**	**99.90**
LOI	2.42	3.92	3.52	2.94	3.75	2.46
FeO	6.62	6.61	5.28	4.02	4.79	5.56
Fe_2O_3	1.35	0.90	1.27	1.58	2.19	1.03

APPENDIX D: Representative electron microprobe analyses

Sample:	CQ38S1					
Mineral	st	ilm	mu	bi	g rim	g core
SiO2	27.6786	1.21061	45.3252	36.0075	37.2831	37.0309
TiO2	0.608093	50.1885	0.254759	1.4877	0.111521	0.091737
Al2O3	55.2939	0.530516	38.275	19.6931	21.2664	20.962
Cr2O3	0.066885	0	0.104859	0.070088	0.030462	0.03145
FeO	11.7708	45.8159	0.900055	17.6698	31.5417	25.6581
MnO	0.299848	1.36819	0	0.083247	5.94249	12.2753
MgO	1.56854	0.565523	0.505744	10.8356	2.34601	1.54949
ZnO	0.714084	0.049936	0	0.001314	0	0
CaO	0	0.121904	0	0	2.62334	3.00703
Na2O	0.007822	0.021174	1.45	0.334448	0.012995	0.048333
K2O	0	0	8.51618	9.02077	0	0.001889
Cl	0.00236	0	0.006156	0.036031	0.001791	0.000694
F	0	0.133829	0	0.291828	0.024479	0.059061
Total	98.010399	99.949733	95.336564	95.40042	101.17358	100.69096
No. Oxygens	46	3	11	11	12	12
Si	7.6209034	0.0302256	2.9824993	2.6996057	2.9768675	2.983139
Ti	0.1259286	0.9424678	0.0126085	0.0838908	0.0066972	0.0055583
Al	17.941951	0.0156099	2.9681504	1.7400092	2.0011128	1.9900869
Cr	0.0145591	0	0.005455	0.0041543	0.0019229	0.002003
Fe3+	0	0.0294627	0	1.107751	0.0254237	0.0231186
Fe2+	2.7100136	0.9270479	0.0495237	0	2.0804666	1.705252
Mn2+	0.0699201	0.0289305	0	0.0052858	0.4018414	0.8374909
Mg	0.6438472	0.0210497	0.0496131	1.2111145	0.2792558	0.1860899
Zn	0.1451523	0.0009204	0	7.273E-05	0	0
Ca	0	0.0032607	0	0	0.2244006	0.2595188
Na	0.0041753	0.0010249	0.1849767	0.0486121	0.0020116	0.0075485
K	0	0	0.7148163	0.8627004	0	0.0001941
Cl	0.0011013	0	0.0006865	0.0045782	0.0002424	9.475E-05
F	0	0.0105657	0	0.0691848	0.0061804	0.0150448

Sample:	QL-1		
Mineral	bi	ru	pl
SiO2	35.139	0.089354	66.6655
TiO2	2.06096	96.5431	0.007335
Al2O3	19.5927	0.05455	20.7273
Cr2O3	0.020089	0.169153	0
FeO	15.5775	0.767925	0.12153
MnO	0.028674	0	0.000707
MgO	11.2383	0	0.000999
ZnO	0	0	0.042763
CaO	0.01092	0.009277	1.25729
Na2O	0.215429	0.015365	11.226
K2O	8.92238	0.100587	0.034238
Cl	0.013744	0.001017	0
F	0.384282	0.020438	0
Total	93.039073	97.761931	100.08366
No. Oxygens	11	2	8
Si	2.6773187	0.0012122	2.9244271
Ti	0.118106	0.9851102	0.000242
Al	1.7592803	0.0008722	1.0715501
Cr	0.0012101	0.0018142	0
Fe3+	0	0.0259134	0
Fe2+	0.9924567	-0.0172019	0.0044579
Mn2+	0.0018503	0	2.627E-05
Mg	1.2765451	0	6.533E-05
Zn	0	0	0.0013849
Ca	0.0008914	0.0001348	0.0590877
Na	0.0318217	0.0004041	0.9547134
K	0.8671623	0.0017407	0.0019158
Cl	0.0017748	2.338E-05	0
F	0.0925842	0.0008768	0

Sample:	2QS2				
Mineral	and	mu	bi	ilm	chl
SiO2	36.2429	45.6512	35.6794	0.014576	24.6813
TiO2	0.037449	0.820912	1.73575	47.0519	0.068916
Al2O3	62.8131	35.556	19.8458	0.030597	22.7076
Cr2O3	0.047761	0.021611	0.005323	0.063685	0.006434
FeO	1.13568	2.34495	17.9911	46.5778	23.2345
MnO	0.008894	0.010112	0.168842	3.91266	0.329154
MgO	0.068651	0.565773	10.6362	0.035567	15.7435
ZnO	0	0	0.034132	0	0.020656
CaO	0	0	0.017558	0.003923	0
Na2O	0.00799	1.04356	0.155918	0	0.01093
K2O	0	9.70577	9.40378	0.002572	0
Cl	0.009307	0.005259	0.013458	0.007006	0.015798
F	0	0	0.491947	0.066262	0.044669
Total	100.36963	95.72396	95.969035	97.737067	86.841084
No. Oxygens	5	11	11	3	14
Si	0.9810656	3.0353886	2.6683598	0.0003746	2.5999276
Ti	0.0007624	0.0410535	0.0976351	0.9096047	0.0054602
Al	2.0038049	2.7861538	1.749144	0.0009268	2.8189966
Cr	0.0010221	0.001136	0.0003147	0.0012941	0.0005358
Fe3+	0	0	0	0.1722142	0
Fe2+	0.025706	0.1303764	1.1250912	0.8288589	2.0465847
Mn2+	0.0002039	0.0005694	0.0106941	0.0851715	0.0293651
Mg	0.0027704	0.0560827	1.1858731	0.0013629	2.4724038
Zn	0	0	0.0018845	0	0.0016064
Ca	0	0	0.0014068	0.000108	0
Na	0.0004193	0.1345203	0.0226064	0	0.0022321
K	0	0.8231919	0.8970948	8.433E-05	0
Cl	0.000427	0.0005926	0.0017058	0.0003052	0.0028204
F	0	0	0.116338	0.0053855	0.0148791

Sample:	4QS4						
Mineral	and	cd	bi	mu	pl	ru	ilm
SiO2	35.7492	47.5598	35.878	44.3263	65.1351	0.13422	0.026895
TiO2	0.059977	0.016623	2.43789	1.01804	0.032687	95.9128	51.8048
Al2O3	63.393	33.3856	19.8882	35.9782	22.3909	0.081702	0.61186
Cr2O3	0.107771	0	0.089075	0.091425	0.006982	0.363494	0.028252
FeO	0.639067	8.80295	19.3259	1.42474	0.073601	0.960955	45.2864
MnO	0	0.375943	0.082554	0	0	0.00153	0.81224
MgO	0.072857	8.0097	9.19833	0.541505	0.010731	0	0.163735
ZnO	0.005968	0	0.034367	0.027945	0.020167	0.000688	0
CaO	0	0.001866	0.036682	0.006737	2.58083	0.012712	0.202402
Na2O	0	0.258273	0.223503	0.699763	10.6293	0	0
K2O	0	0	9.00036	9.81573	0.072583	0.004331	0
Cl	0.005572	0.000427	0.012979	0.026471	0.003043	0	0.002233
F	0	0	0.31793	0	0	0	0.086337
Total	100.03215	98.411086	96.388976	93.950882	100.95524	97.472432	98.988298
No. Oxygens	5	18	11	11	8	2	3
Si	0.969172	4.9189872	2.6817453	2.9935388	2.8455875	0.0018266	0.000683
Ti	0.001223	0.0012931	0.1370551	0.0517107	0.001074	0.9817319	0.9895472
Al	2.0253773	4.0693491	1.7519225	2.863472	1.152812	0.0013103	0.0183129
Cr	0.0023098	0	0.0052637	0.0048813	0.0002411	0.0039108	0.0005672
Fe3+	0	0	0	0	0	0.0277371	0
Fe2+	0.0144872	0.7613197	1.2079034	0.0804567	0.0026887	-0.0168018	0.9617132
Mn2+	0	0.0329304	0.005226	0	0	1.763E-05	0.0174702
Mg	0.0029446	1.235028	1.0249984	0.0545194	0.0006989	0	0.0061993
Zn	0.0001194	0	0.0018965	0.0013933	0.0006504	6.912E-06	0
Ca	0	0.0002068	0.0029374	0.0004874	0.120792	0.0001853	0.005507
Na	0	0.0517873	0.0323878	0.0916184	0.900264	0	0
K	0	0	0.8581401	0.8455806	0.0040448	7.518E-05	0
Cl	0.000256	7.485E-05	0.0016442	0.0030298	0.0002253	0	9.611E-05
F	0	0	0.0751445	0	0	0	0.0069334

APPENDIX E: Additional garnet transect—electron microprobe analysis

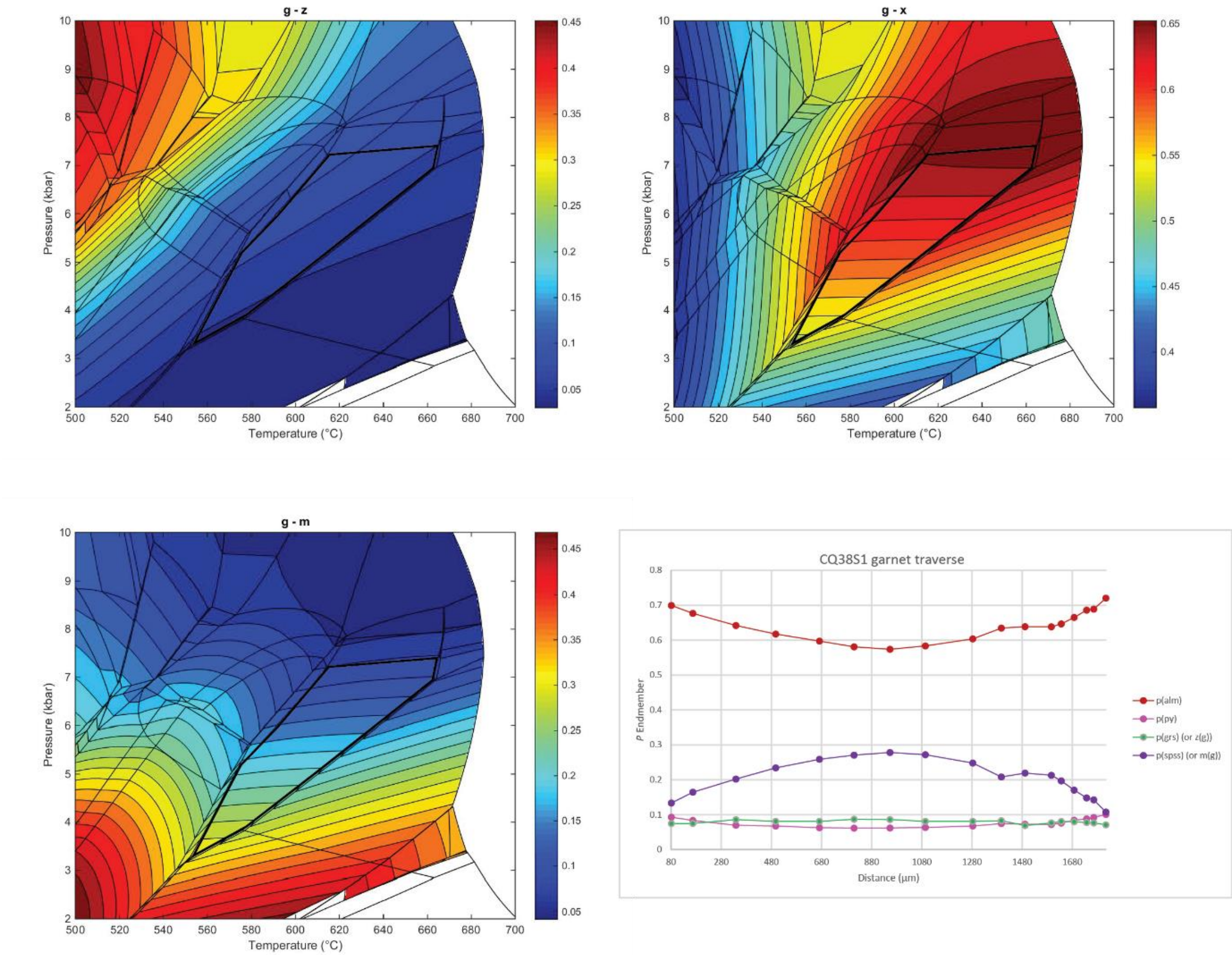

Appendix Figure 2: Chemical zoning profile from a single garnet grain for sample CQ38S1. Zonation is defined by enrichment of alamandine in the rim and lower in the core, conversely, spessartine is enriched in the core and lower towards the rim. TC Investigator outputs for g(z), g(x) and g(m) are coupled with this garnet transect.

APPENDIX F: U–Pb geochronology zircon standard analyses

Analysis	^{207}Pb/^{206}Pb	2σ	^{207}Pb/^{235}U	2σ	^{206}Pb/^{236}U	2σ	%Conc.	^{207}Pb/^{2006}Pb Age (Ma)	2σ	^{206}Pb/^{238}U Age (Ma)	2σ	^{207}Pb/^{235}U age (Ma)	2σ
QL-3													
GJ_01	0.0666	0.0067	0.873	0.083	0.0978	0.003	99.34	560	190	601	18	605	45
GJ_02	0.0578	0.0051	0.74	0.064	0.0978	0.003	108.70	400	170	600	20	552	35
GJ_03	0.0613	0.005	0.839	0.07	0.0974	0.003	98.68	580	160	599	17	607	37
GJ_04	0.0559	0.0048	0.78	0.066	0.0979	0.004	103.62	440	170	601	21	580	37
GJ_05	0.06	0.0048	0.812	0.065	0.0978	0.003	98.85	550	150	602	19	609	35
GJ_06	0.0596	0.0049	0.805	0.065	0.0981	0.004	101.00	490	170	604	21	598	38
GJ_07	0.0607	0.0058	0.794	0.071	0.0967	0.003	103.48	470	180	594	20	574	41
GJ_08	0.0571	0.0049	0.802	0.066	0.1	0.003	102.68	410	160	613	20	597	37
GJ_09	0.0575	0.0048	0.769	0.066	0.0964	0.003	103.85	440	160	593	17	571	38
GJ_10	0.0615	0.0052	0.831	0.069	0.0987	0.003	98.70	530	160	606	19	614	39
GJ_11	0.0617	0.0054	0.85	0.073	0.0988	0.003	98.06	580	170	606	19	618	39
GJ_12	0.0597	0.0057	0.794	0.069	0.1	0.004	107.33	400	170	615	21	573	39
GJ_13	0.063	0.0058	0.819	0.072	0.0977	0.003	97.88	580	170	600	16	613	41
GJ_14	0.057	0.0056	0.766	0.069	0.0975	0.003	107.32	350	180	601	19	560	39
GJ_15	0.06	0.0053	0.793	0.064	0.0987	0.003	105.01	460	170	608	20	579	37
GJ_16	0.0611	0.0052	0.816	0.069	0.0973	0.003	100.51	570	160	597	19	594	38
GJ_17	0.0633	0.0056	0.828	0.068	0.0973	0.003	99.33	610	180	597	20	601	38
GJ_18	0.0634	0.0057	0.888	0.08	0.098	0.004	96.02	650	180	603	20	628	43
GJ_19	0.0635	0.0055	0.813	0.068	0.096	0.003	100.00	570	170	592	18	592	39
GJ_20	0.065	0.0047	0.855	0.057	0.0969	0.003	95.51	700	140	595	16	623	32
GJ_21	0.0617	0.0054	0.834	0.07	0.0987	0.003	101.16	560	160	608	20	601	38
GJ_22	0.064	0.0058	0.844	0.072	0.0973	0.003	99.01	610	180	598	19	604	40
GJ_23	0.063	0.0052	0.88	0.073	0.0999	0.003	99.51	620	170	613	20	616	40
GJ_24	0.0576	0.0046	0.795	0.062	0.0984	0.004	103.25	470	160	604	21	585	36
GJ_25	0.0606	0.0054	0.818	0.073	0.095	0.003	100.52	500	170	584	19	581	40
GJ_26	0.0596	0.0055	0.8	0.071	0.0989	0.004	103.24	470	170	606	22	587	40

GJ_27	0.0628	0.0059	0.856	0.077	0.0968	0.003	98.51	520	180	594	19	603	43
GJ_28	0.0578	0.0054	0.83	0.079	0.0974	0.004	100.50	460	180	598	20	595	42
GJ_29	0.0587	0.0057	0.797	0.075	0.0969	0.003	101.70	530	180	597	18	587	42
GJ_30	0.0563	0.0048	0.784	0.068	0.0971	0.003	101.53	450	160	596	17	587	38
GJ_31	0.0627	0.0051	0.855	0.066	0.0979	0.003	96.31	630	160	601	19	624	35
GJ_32	0.0666	0.0059	0.859	0.072	0.0985	0.004	99.84	670	180	608	21	609	41
GJ_33	0.0621	0.0054	0.861	0.074	0.0991	0.004	100.00	610	170	612	20	612	40
GJ_34	0.0602	0.0051	0.795	0.061	0.0947	0.003	98.81	550	170	582	20	589	35
GJ_35	0.0585	0.0054	0.803	0.074	0.0995	0.003	105.50	450	180	614	19	582	43
GJ_36	0.059	0.0055	0.823	0.074	0.1	0.003	101.66	510	180	613	19	603	41
GJ_37	0.0578	0.005	0.783	0.067	0.1008	0.003	108.01	400	170	620	19	574	39
GJ_38	0.0588	0.0056	0.819	0.075	0.0988	0.003	103.58	450	180	608	19	587	42
GJ_39	0.0669	0.0057	0.908	0.066	0.0984	0.003	92.27	730	170	609	18	660	33
GJ_40	0.0582	0.0051	0.808	0.064	0.0994	0.004	102.53	480	170	609	22	594	35
GJ_41	0.0598	0.0054	0.796	0.065	0.0981	0.004	103.61	510	170	602	20	581	36
GJ_42	0.0598	0.0052	0.827	0.069	0.0982	0.004	102.20	490	170	605	21	592	38
GJ_43	0.0616	0.0049	0.842	0.063	0.0974	0.003	94.79	640	150	600	20	633	34
GJ_44	0.0588	0.0055	0.799	0.07	0.0968	0.003	103.48	420	180	595	18	575	40
GJ_45	0.061	0.0053	0.815	0.069	0.1005	0.003	103.35	480	170	617	19	597	39
GJ_46	0.059	0.0051	0.788	0.066	0.0969	0.003	99.66	550	170	595	17	597	38
GJ_47	0.0629	0.0053	0.831	0.067	0.0967	0.003	99.00	610	170	594	19	600	37
GJ_48	0.0614	0.0048	0.841	0.062	0.0972	0.004	97.40	660	150	599	20	615	32
GJ_49	0.0604	0.0053	0.792	0.064	0.0973	0.003	101.02	510	170	597	20	591	38
GJ_50	0.0563	0.0051	0.762	0.065	0.0976	0.003	108.32	350	170	599	18	553	38
GJ_51	0.0618	0.0052	0.81	0.063	0.0971	0.004	98.51	560	170	596	21	605	37
GJ_52	0.0573	0.0054	0.771	0.069	0.0984	0.004	106.53	440	180	604	21	567	39
GJ_53	0.0617	0.0053	0.809	0.066	0.0968	0.003	100.67	560	170	598	17	594	36
GJ_54	0.0604	0.0058	0.815	0.075	0.0997	0.003	101.83	490	180	612	20	601	41
GJ_55	0.0593	0.0052	0.784	0.062	0.0964	0.004	100.34	550	160	592	21	590	35
2QS2													

GJ_01	0.0615	0.0057	0.835	0.084	0.0989	0.002	98.38	620	190	607	12	617	46
GJ_02	0.0588	0.0055	0.797	0.081	0.0981	0.002	101.52	520	200	603	13	594	46
GJ_03	0.0617	0.006	0.833	0.088	0.097	0.002	96.30	650	200	598	14	621	49
GJ_04	0.0617	0.0058	0.849	0.086	0.0994	0.002	97.60	630	200	610	13	625	45
GJ_05	0.0622	0.006	0.826	0.083	0.0969	0.003	96.28	680	190	596	15	619	45
GJ_06	0.0608	0.0059	0.836	0.091	0.0977	0.002	98.53	600	210	602	11	611	50
GJ_07	0.0629	0.0061	0.851	0.089	0.0987	0.002	98.06	650	200	606	14	618	48
GJ_08	0.0631	0.0062	0.876	0.091	0.0997	0.002	96.84	670	210	612	12	632	49
GJ_09	0.0625	0.0059	0.855	0.087	0.0973	0.002	94.77	720	190	598	14	631	48
GJ_10	0.0595	0.006	0.782	0.083	0.0974	0.002	102.22	480	200	599	13	586	48
GJ_11	0.0609	0.0058	0.801	0.084	0.0965	0.002	100.34	600	200	595	14	593	47
GJ_12	0.0555	0.0053	0.741	0.078	0.0969	0.002	105.67	420	190	596	12	564	45
GJ_13	0.0618	0.006	0.854	0.089	0.1	0.002	98.40	620	200	614	13	624	48
GJ_14	0.0577	0.0056	0.782	0.082	0.0972	0.002	102.22	470	190	598	12	585	45
GJ_15	0.0602	0.0056	0.814	0.084	0.0987	0.002	100.66	590	190	608	13	604	46
GJ_16	0.0615	0.0059	0.818	0.085	0.0972	0.002	98.68	550	200	597	13	605	47
GJ_17	0.0577	0.0056	0.784	0.082	0.0977	0.003	102.90	500	200	603	14	586	46
GJ_18	0.0618	0.006	0.812	0.082	0.0966	0.002	99.00	610	190	594	12	600	44
GJ_19	0.064	0.0065	0.858	0.093	0.0974	0.002	98.20	610	180	599	12	610	47
GJ_20	0.0611	0.0058	0.861	0.089	0.0982	0.002	97.42	620	200	604	13	620	49
GJ_21	0.0631	0.0058	0.84	0.084	0.0976	0.002	96.93	670	200	600	14	619	47
GJ_22	0.0625	0.0057	0.817	0.083	0.0962	0.002	96.10	660	190	591	14	615	45
GJ_23	0.0611	0.0059	0.805	0.082	0.0993	0.002	100.33	580	200	610	13	608	49
GJ_24	0.0543	0.0051	0.74	0.075	0.0984	0.002	107.65	380	190	605	13	562	45
GJ_25	0.058	0.0056	0.775	0.082	0.0973	0.002	102.75	490	200	598	13	582	47
4QS4													
GJ_01	0.062	0.0043	0.838	0.061	0.0974	0.003	97.24	620	140	599	19	616	34
GJ_02	0.058	0.0043	0.772	0.059	0.0982	0.003	103.60	480	140	605	18	584	34
GJ_03	0.0614	0.0045	0.825	0.06	0.0977	0.003	99.01	600	150	602	19	608	33
GJ_04	0.0614	0.0041	0.84	0.059	0.1	0.003	98.71	590	140	614	20	622	33

GJ_05	0.0604	0.0042	0.801	0.058	0.0966	0.003	100.34	550	150	594	18	592	34
GJ_06	0.0581	0.0041	0.788	0.058	0.0973	0.003	101.18	500	150	600	18	593	33
GJ_07	0.0614	0.0042	0.825	0.059	0.0969	0.003	97.70	580	140	596	19	610	33
GJ_08	0.0596	0.0041	0.813	0.059	0.097	0.003	98.52	540	140	598	18	607	32
GJ_09	0.0609	0.004	0.821	0.058	0.0974	0.003	98.68	590	140	599	17	607	31
GJ_10	0.0613	0.0041	0.844	0.058	0.0988	0.003	97.43	620	140	607	19	623	32
GJ_11	0.06	0.0038	0.812	0.057	0.0991	0.003	100.00	580	130	609	18	609	32
GJ_12	0.0609	0.0041	0.813	0.057	0.0983	0.003	99.83	590	140	604	19	605	32
GJ_13	0.0612	0.0043	0.801	0.058	0.0962	0.003	99.33	580	140	593	19	597	32
GJ_14	0.0564	0.0041	0.765	0.058	0.0996	0.003	106.78	420	140	614	19	575	33
GJ_15	0.0629	0.004	0.853	0.055	0.0983	0.003	96.79	660	130	604	18	624	30
GJ_16	0.0599	0.0038	0.827	0.057	0.0997	0.003	100.49	580	130	612	18	609	32
GJ_17	0.0637	0.0044	0.837	0.061	0.0953	0.003	95.45	670	140	588	18	616	33
GJ_18	0.0578	0.0039	0.773	0.056	0.0974	0.003	102.57	500	140	599	19	584	32
CQ38S1													
GJ_01	0.0603	0.0048	0.796	0.06	0.0966	0.002	100.17	550	160	595	12	594	33
GJ_02	0.0576	0.004	0.795	0.053	0.0984	0.002	102.54	500	140	606	13	591	30
GJ_03	0.0611	0.0047	0.814	0.057	0.0979	0.002	99.34	560	150	602	13	606	32
GJ_04	0.0578	0.0042	0.773	0.054	0.0973	0.002	103.82	470	150	598	12	576	31
GJ_05	0.0629	0.0047	0.836	0.06	0.098	0.002	98.53	630	150	604	11	613	33
GJ_06	0.0608	0.0046	0.827	0.059	0.0978	0.002	99.01	590	150	601	11	607	33
GJ_07	0.0594	0.0044	0.807	0.055	0.0979	0.002	100.67	530	160	602	12	598	31
GJ_08	0.0628	0.0043	0.867	0.057	0.0972	0.002	94.93	670	150	599	12	631	32
GJ_09	0.061	0.0045	0.802	0.057	0.0977	0.002	100.33	570	150	601	12	599	32
GJ_10	0.0625	0.0043	0.825	0.054	0.0974	0.002	97.40	650	140	599	11	615	30
GJ_11	0.0631	0.0046	0.842	0.056	0.0975	0.002	96.93	650	150	599	13	618	30
GJ_12	0.063	0.0044	0.842	0.055	0.0988	0.002	97.75	660	150	608	12	622	32
GJ_13	0.0569	0.0042	0.793	0.056	0.0981	0.002	102.73	460	140	603	12	587	31
GJ_14	0.0593	0.0042	0.814	0.055	0.0991	0.002	100.50	530	150	609	11	606	31
GJ_15	0.057	0.0046	0.767	0.058	0.0976	0.002	104.17	520	170	600	12	576	33

GJ_16	0.0605	0.0046	0.837	0.061	0.0973	0.002	98.36	550	150	598	12	608	34
GJ_17	0.063	0.0047	0.841	0.057	0.097	0.002	97.39	650	160	596	13	612	32
GJ_18	0.0592	0.0043	0.805	0.055	0.0992	0.002	102.69	540	150	610	11	594	31
GJ_19	0.0594	0.0042	0.807	0.052	0.0999	0.002	102.00	520	140	613	14	601	29
GJ_20	0.062	0.0045	0.82	0.056	0.0953	0.002	97.35	610	150	587	13	603	31
GJ_21	0.0596	0.0044	0.795	0.053	0.098	0.002	101.69	550	150	602	12	592	30
GJ_22	0.0594	0.0042	0.796	0.051	0.0971	0.002	101.18	560	150	598	13	591	29
GJ_23	0.0588	0.0044	0.78	0.055	0.0981	0.002	103.97	510	160	603	12	580	32
GJ_24	0.066	0.0049	0.88	0.061	0.0972	0.002	93.15	760	150	598	13	642	33
GJ_25	0.0587	0.0043	0.793	0.053	0.0974	0.002	101.18	490	150	599	11	592	30
GJ_26	0.0607	0.0046	0.813	0.056	0.0977	0.002	99.83	590	160	600	12	601	32
GJ_27	0.0592	0.0044	0.803	0.056	0.0985	0.002	100.50	570	150	605	13	602	32
GJ_28	0.0589	0.0047	0.806	0.06	0.0984	0.002	101.17	520	160	605	13	598	33
GJ_29	0.0574	0.0044	0.778	0.056	0.0994	0.002	103.91	490	150	611	12	588	33
GJ_30	0.0599	0.0042	0.847	0.057	0.1001	0.002	99.19	580	150	616	12	621	32
GJ_31	0.0625	0.0046	0.84	0.058	0.0981	0.002	97.89	620	150	603	12	616	32
GJ_32	0.0604	0.0044	0.811	0.056	0.0974	0.002	99.50	570	150	599	12	602	32
GJ_33	0.0577	0.0045	0.788	0.055	0.0983	0.002	102.20	500	150	604	14	591	32
GJ_34	0.0615	0.0045	0.834	0.058	0.0984	0.002	98.70	610	150	606	12	614	33
GJ_35	0.0632	0.0047	0.84	0.059	0.0964	0.002	95.80	660	150	593	12	619	33
GJ_36	0.0634	0.0046	0.854	0.058	0.0986	0.002	96.19	670	150	606	12	630	32
GJ_37	0.0608	0.0047	0.824	0.057	0.0985	0.002	99.34	590	150	606	14	610	31
GJ_38	0.0609	0.0049	0.805	0.06	0.0971	0.002	100.34	570	160	599	12	597	34
GJ_39	0.0622	0.0045	0.854	0.058	0.0965	0.002	96.12	660	150	595	13	619	31
GJ_40	0.0642	0.0047	0.861	0.062	0.0973	0.002	95.39	680	160	600	12	629	34
GJ_41	0.0598	0.0043	0.835	0.056	0.0997	0.002	100.33	570	150	614	12	612	30
GJ_42	0.059	0.0041	0.776	0.053	0.0968	0.002	101.71	540	150	595	13	585	29
GJ_43	0.0589	0.0043	0.818	0.055	0.0994	0.002	102.35	500	150	611	12	597	31
GJ_44	0.0595	0.0045	0.811	0.055	0.0992	0.002	100.00	550	150	610	13	610	31
GJ_45	0.0608	0.0047	0.808	0.06	0.096	0.002	98.17	540	160	591	12	602	34

GJ_46	0.0617	0.0046	0.833	0.06	0.0988	0.002	98.38	620	150	608	13	618	33
GJ_47	0.0637	0.0046	0.868	0.058	0.0973	0.002	94.64	690	150	600	13	634	32
GJ_48	0.0633	0.0045	0.829	0.057	0.0967	0.002	96.91	650	150	596	11	615	32
GJ_49	0.0597	0.0047	0.787	0.055	0.0957	0.002	100.86	540	160	589	13	584	32
GJ_50	0.0615	0.0044	0.809	0.056	0.0969	0.002	97.55	640	150	596	11	611	31
GJ_51	0.0558	0.0042	0.768	0.053	0.0987	0.002	104.29	420	150	608	13	583	32
GJ_52	0.0629	0.0047	0.853	0.057	0.0988	0.002	97.75	650	150	607	12	621	32
GJ_53	0.0597	0.0045	0.81	0.056	0.0974	0.002	100.50	540	160	599	13	596	31
GJ_54	0.0621	0.0047	0.823	0.058	0.0978	0.002	98.85	650	150	601	12	608	32
GJ_55	0.0568	0.0046	0.777	0.058	0.0979	0.002	103.09	450	160	601	12	583	33
GJ_56	0.0587	0.0046	0.773	0.056	0.0964	0.002	103.49	470	160	593	12	573	32
GJ_57	0.0604	0.0044	0.809	0.052	0.0975	0.002	99.67	570	140	599	12	601	28
GJ_58	0.0586	0.0045	0.818	0.057	0.0999	0.002	100.99	510	150	613	12	607	32

Analysis	**$^{207}Pb/^{206}Pb$**	**2σ**	**$^{207}Pb/^{235}U$**	**2σ**	**$^{206}Pb/^{236}U$**	**2σ**	**%Conc.**	**$^{207}Pb/^{2006}Pb$ Age (Ma)**	**2σ**	**$^{206}Pb/^{238}U$ Age (Ma)**	**2σ**	**$^{207}Pb/^{235}U$ age (Ma)**	**2σ**
QL-3													
PLES_01	0.0518	0.0031	0.401	0.023	0.0558	0.0011	102.64	290	120	350	6.8	341	17
PLES_02	0.0537	0.0032	0.407	0.023	0.05452	0.00096	98.30	350	120	342.1	5.9	348	16
PLES_03	0.0499	0.0034	0.38	0.025	0.0545	0.001	103.89	210	130	341.8	6.3	329	18
PLES_04	0.0517	0.0033	0.392	0.024	0.054	0.0012	100.83	250	120	338.8	7.3	336	17
PLES_05	0.0469	0.0037	0.352	0.026	0.0539	0.0011	110.85	70	140	339.2	6.8	306	19
PLES_06	0.0541	0.0038	0.411	0.028	0.0548	0.0011	99.74	330	140	344.1	6.9	345	20
PLES_07	0.0507	0.0036	0.39	0.026	0.0557	0.0013	104.52	220	130	349.1	7.8	334	19
PLES_08	0.0506	0.0038	0.372	0.027	0.0541	0.0012	104.75	210	140	339.4	7.1	324	21
PLES_09	0.0523	0.0039	0.399	0.028	0.0539	0.0011	98.06	340	140	338.3	6.8	345	20
PLES_10	0.0543	0.0038	0.404	0.025	0.0542	0.0013	99.01	320	140	341.6	8	345	18
PLES_11	0.0564	0.0043	0.411	0.029	0.0535	0.0011	95.07	370	150	335.6	6.8	353	21

PLES_12	0.0502	0.0033	0.373	0.024	0.053	0.0011	103.68	200	130	332.8	6.9	321	18
PLES_13	0.0574	0.0049	0.436	0.034	0.0538	0.0015	93.43	450	160	337.3	9.2	361	24
PLES_14	0.0487	0.004	0.355	0.027	0.0538	0.0012	111.02	130	150	337.5	7.5	304	20
PLES_15	0.053	0.0049	0.406	0.033	0.0543	0.0014	99.88	300	170	340.6	8.6	341	24
PLES_16	0.0536	0.0044	0.396	0.031	0.0535	0.0014	100.18	290	160	335.6	8.5	335	23
PLES_17	0.0551	0.0051	0.413	0.036	0.0527	0.0013	97.01	340	170	330.8	8	341	26
PLES_18	0.0557	0.0053	0.406	0.037	0.0525	0.0016	95.16	440	170	330.2	9.8	347	26
PLES_19	0.0503	0.0039	0.379	0.028	0.0537	0.0014	101.14	230	140	337.8	8.3	334	21
PLES_20	0.0515	0.0033	0.376	0.023	0.0535	0.0012	102.78	230	130	336.1	7.3	327	17
PLES_21	0.0527	0.0042	0.389	0.028	0.0539	0.0013	101.01	260	150	338.4	7.9	335	20
PLES_22	0.0488	0.0046	0.367	0.033	0.0536	0.0016	104.98	190	160	337	10	321	24
PLES_23	0.0543	0.0034	0.404	0.025	0.0527	0.0011	95.94	380	120	331	6.6	345	17
PLES_24	0.049	0.0037	0.358	0.025	0.0526	0.0011	106.14	140	130	330.1	6.5	311	19
PLES_25	0.054	0.0034	0.405	0.024	0.0546	0.0012	99.77	340	120	343.2	7.4	344	17
PLES_26	0.053	0.0032	0.388	0.023	0.054	0.001	102.29	300	120	339.6	6.3	332	17
PLES_27	0.0541	0.0033	0.408	0.023	0.0541	0.0012	97.28	350	120	339.5	7.1	349	17
PLES_28	0.0538	0.0038	0.394	0.026	0.0534	0.0011	100.12	320	140	335.4	6.7	335	19
2QS2													
PLES_01	0.0569	0.0052	0.432	0.044	0.0548	0.0011	94.94	430	190	343.7	6.4	362	31
PLES_03	0.054	0.005	0.416	0.042	0.054	0.0011	97.28	360	180	339.5	6.8	349	30
PLES_06	0.0566	0.0052	0.408	0.041	0.0541	0.001	96.78	430	190	339.7	6.1	351	30
PLES_08	0.0548	0.0051	0.405	0.041	0.0545	0.0011	99.16	390	180	342.1	6.7	345	30
PLES_04	0.0538	0.005	0.404	0.041	0.0539	0.0011	98.92	350	190	338.3	6.8	342	30
PLES_07	0.0516	0.0049	0.393	0.04	0.0549	0.0011	103.45	280	190	344.5	6.4	333	29
PLES_02	0.0519	0.0048	0.384	0.038	0.0546	0.0011	104.74	280	190	342.5	6.5	327	28
PLES_05	0.0503	0.0048	0.372	0.038	0.0547	0.0011	107.59	200	180	343.2	6.9	319	28
4QS4													
PLES_02	0.0534	0.0033	0.403	0.026	0.0536	0.0016	98.54	330	120	337	10	342	19
PLES_01	0.0529	0.0034	0.398	0.028	0.0537	0.0017	99.41	310	130	337	10	339	20
PLES_04	0.0518	0.0033	0.389	0.027	0.0541	0.0017	101.50	260	130	339	10	334	20

PLES_03	0.0516	0.0034	0.376	0.024	0.0539	0.0016	104.06	180	110	338.2	9.8	325	18
PLES_05	0.0513	0.0036	0.379	0.027	0.0533	0.0017	102.45	230	130	335	10	327	20
PLES_06	0.0499	0.0029	0.376	0.024	0.0539	0.0016	104.06	180	110	338.2	9.8	325	18
CQ38S1													
PLES_01	0.0505	0.0037	0.379	0.026	0.0538	0.0011	103.33	260	140	337.9	6.9	327	19
PLES_02	0.0524	0.0043	0.392	0.031	0.0536	0.001	98.10	260	160	336.5	6.3	343	21
PLES_03	0.0543	0.0039	0.398	0.027	0.05334	0.0009	99.38	340	150	334.9	5.5	337	19
PLES_04	0.0528	0.0038	0.4	0.027	0.0538	0.001	98.77	320	150	337.8	6.3	342	20
PLES_05	0.0549	0.0035	0.409	0.025	0.05394	0.0009	97.86	370	140	338.6	5.5	346	18
PLES_06	0.0537	0.0036	0.396	0.025	0.05367	0.00091	99.97	320	140	336.9	5.6	337	18
PLES_07	0.0537	0.0037	0.402	0.026	0.05419	0.00098	99.15	350	140	340.1	6	343	18
PLES_08	0.0535	0.0042	0.408	0.03	0.0548	0.0011	100.58	340	160	344	6.6	342	22
PLES_09	0.0502	0.0036	0.378	0.026	0.0531	0.0011	102.62	240	140	333.5	6.8	325	19
PLES_10	0.052	0.0039	0.399	0.028	0.0556	0.0011	102.35	270	150	349	6.5	341	21
PLES_11	0.055	0.0039	0.409	0.027	0.05303	0.00097	96.11	380	150	333.5	5.8	347	20
PLES_12	0.053	0.0037	0.393	0.026	0.0539	0.001	100.60	310	140	338	6.1	336	19
PLES_13	0.0524	0.0039	0.385	0.027	0.0536	0.0011	102.50	270	150	336.2	6.7	328	20
PLES_14	0.0519	0.0039	0.385	0.027	0.0535	0.0011	102.59	260	150	336.5	6.8	328	20
PLES_15	0.0516	0.0035	0.384	0.026	0.05406	0.00099	102.51	260	140	339.3	6.1	331	19
PLES_16	0.0538	0.0038	0.405	0.026	0.05461	0.00099	99.88	330	140	342.6	6	343	19
PLES_17	0.0553	0.0043	0.408	0.029	0.0536	0.0011	96.20	380	150	336.7	6.6	350	21
PLES_18	0.0569	0.004	0.424	0.028	0.0542	0.0011	93.64	460	150	339.9	6.8	363	19
PLES_19	0.057	0.0039	0.416	0.026	0.0536	0.0011	95.81	460	140	336.3	6.7	351	19
PLES_20	0.0518	0.0037	0.39	0.026	0.0548	0.0011	102.60	260	140	343.7	6.5	335	18

APPENDIX G: U–Pb geochronology monazite standard analyses

Analysis	$^{207}Pb/^{206}Pb$	2σ	$^{207}Pb/^{235}U$	2σ	$^{206}Pb/^{236}U$	2σ	%Conc.	$^{207}Pb/^{2006}Pb$ Age (Ma)	2σ	$^{206}Pb/^{238}U$ Age (Ma)	2σ	$^{207}Pb/^{235}U$ age (Ma)	2σ
QL-1													
MADEL_01	0.0573	0.0057	0.83	0.18	0.108	0.019	107.14	500	220	660	110	616	98
MADEL_02	0.0569	0.0056	0.68	0.14	0.087	0.015	102.47	480	220	540	91	527	87
MADEL_03	0.0568	0.0056	0.54	0.11	0.071	0.012	99.55	470	220	440	75	442	76
MADEL_04	0.057	0.015	0.69	0.25	0.088	0.013	102.26	470	580	542	76	530	150
MADEL_05	0.0562	0.0097	0.68	0.16	0.0897	0.0038	104.93	450	380	553	22	527	93
MADEL_06	0.057	0.0057	0.71	0.15	0.09	0.016	101.83	480	220	555	97	545	90
MADEL_07	0.057	0.015	0.64	0.23	0.082	0.012	101.80	480	600	509	72	500	140
MADEL_08	0.0563	0.0056	0.67	0.14	0.086	0.016	102.12	450	210	531	93	520	87
MADEL_09	0.0562	0.0064	0.658	0.074	0.0848	0.0016	102.30	460	250	524.8	9.7	513	44
MADEL_10	–	–	0.684	0.078	0.0862	0.0053	100.76	490	180	533	32	529	47
MADEL_11	0.057	0.015	0.68	0.24	0.084	0.012	100.19	490	590	521	73	520	150
MADEL_12	0.067	0.012	0.77	0.18	0.0852	0.0035	91.03	830	370	528	21	580	100
MADEL_13	0.0677	0.0071	0.76	0.17	0.084	0.015	91.39	810	210	520	91	569	91
MADEL_14	0.0565	0.0064	0.651	0.073	0.0827	0.0016	100.67	480	250	512.4	9.3	509	44
MADEL_15	–	–	0.666	0.076	0.0853	0.0051	101.54	480	180	527	31	519	47
MADEL_16	0.057	0.015	0.62	0.22	0.079	0.012	100.00	480	600	490	69	490	140
MADEL_17	0.0565	0.0097	0.63	0.14	0.0822	0.0034	103.04	460	380	509	20	494	88
MADEL_18	0.0564	0.0056	0.61	0.13	0.08	0.015	101.85	470	220	496	87	487	82
MADEL_19	0.0569	0.0065	0.652	0.073	0.0823	0.0016	100.10	480	260	509.5	9.4	509	44
MADEL_20	–	–	0.66	0.077	0.0837	0.0051	100.58	490	190	518	30	515	47
MADEL_21	0.0559	0.0096	0.63	0.14	0.0826	0.0034	102.81	430	380	512	20	498	88
MADEL_22	0.0571	0.0057	0.63	0.14	0.081	0.015	101.01	500	210	502	88	497	86
MADEL_23	0.0564	0.0018	0.672	0.083	0.086	0.011	101.72	468	69	531	64	522	50
MADEL_24	0.067	0.0077	0.77	0.087	0.0828	0.0016	89.10	810	240	513.2	9.5	576	49
MADEL_25	0.0552	0.0095	0.62	0.14	0.0824	0.0034	104.29	410	380	510	20	489	88
MADEL_26	0.059	0.006	0.7	0.15	0.088	0.016	103.02	510	160	546	95	530	68

MADEL_27	0.0585	0.0019	0.679	0.084	0.084	0.01	98.48	542	68	519	62	527	51
MADEL_28	0.0569	0.0065	0.651	0.072	0.0826	0.0016	100.73	480	250	511.7	9.4	508	44
MADEL_29	–	–	0.81	0.13	0.0868	0.0057	94.37	600	110	536	34	568	44
MADEL_30	0.0562	0.0097	0.66	0.15	0.0838	0.0035	100.78	450	390	519	21	515	92
MADEL_31	0.0562	0.0056	0.64	0.14	0.085	0.015	104.37	460	220	525	91	503	85
MADEL_32	0.0564	0.0018	0.648	0.08	0.083	0.01	101.38	467	71	514	62	507	50
MADEL_33	–	–	0.631	0.07	0.0806	0.005	100.40	480	180	499	30	497	43
MADEL_34	0.0564	0.0097	0.63	0.14	0.0824	0.0034	102.82	470	380	511	20	497	89
MADEL_35	0.0573	0.0057	0.64	0.14	0.082	0.015	101.80	500	220	510	89	501	84
MADEL_36	0.0566	0.0018	0.649	0.08	0.083	0.01	100.99	471	72	512	61	507	50
MADEL_37	–	–	0.639	0.077	0.081	0.005	100.20	490	190	502	30	501	48
MADEL_38	–	–	0.661	0.079	0.0846	0.0054	101.75	480	190	523	32	514	49
MADEL_39	0.085	0.023	1.02	0.36	0.087	0.013	42.78	1260	540	539	75	700	180
MADEL_40	0.0561	0.0018	0.686	0.09	0.088	0.012	102.65	451	72	543	68	529	55
MADEL_41	0.0569	0.0065	0.676	0.074	0.0853	0.0016	100.71	490	250	527.7	9.5	524	45
MADEL_42	–	–	0.667	0.08	0.0846	0.0054	101.16	500	180	524	32	518	48
MADEL_43	0.057	0.015	0.68	0.24	0.084	0.012	97.55	500	610	517	72	530	150
MADEL_44	0.057	0.0057	0.66	0.14	0.085	0.015	102.52	490	220	528	91	515	86
MADEL_45	0.0574	0.0018	0.633	0.078	0.08	0.01	99.40	510	69	494	59	497	49
MADEL_46	0.057	0.0065	0.66	0.073	0.084	0.0016	101.44	480	250	520.4	9.3	513	43
MADEL_47	–	–	0.651	0.078	0.0824	0.0052	100.00	490	190	510	31	510	47
MADEL_48	0.057	0.015	0.63	0.21	0.081	0.011	100.00	480	590	500	68	500	130
MADEL_49	0.0571	0.0098	0.66	0.15	0.084	0.0035	100.58	490	380	520	21	517	90
MADEL_50	0.0568	0.0065	0.673	0.073	0.0842	0.0016	99.69	480	250	521.4	9.5	523	45
MADEL_51	0.057	0.015	0.68	0.22	0.086	0.012	101.92	490	600	530	71	520	140
MADEL_52	0.0571	0.0065	0.641	0.069	0.0814	0.0015	99.92	490	250	504.6	9.1	505	44
MADEL_53	0.0574	0.0019	0.667	0.082	0.084	0.011	100.58	499	71	521	63	518	50
QL-2													
MADEL_01	0.0566	0.0012	0.686	0.025	0.0873	0.0036	101.89	466	47	540	21	530	15
MADEL_02	0.0566	0.001	0.679	0.037	0.0854	0.004	100.38	461	41	528	24	526	22

MADEL_03	0.0565	0.0021	0.666	0.046	0.0858	0.005	102.51	471	88	531	30	518	28
MADEL_04	0.05726	0.00078	0.675	0.059	0.0864	0.0086	102.10	494	30	535	51	524	37
MADEL_05	0.0564	0.0012	0.652	0.024	0.0829	0.0034	100.59	466	48	513	20	510	15
MADEL_06	0.0562	0.0014	0.672	0.05	0.0872	0.0054	103.06	449	56	539	32	523	30
MADEL_07	0.05691	0.00097	0.685	0.037	0.0849	0.004	99.06	493	38	525	24	530	22
MADEL_08	0.0566	0.0022	0.65	0.045	0.0838	0.0048	101.37	467	85	519	29	512	27
MADEL_09	0.05671	0.0008	0.675	0.059	0.0863	0.0086	102.10	470	31	534	50	523	36
MADEL_10	0.0575	0.0012	0.641	0.023	0.0814	0.0034	100.20	511	46	504	20	503	14
MADEL_11	0.0571	0.0014	0.674	0.05	0.0854	0.0053	100.76	485	55	528	32	524	30
MADEL_12	0.0563	0.001	0.646	0.035	0.0818	0.0039	100.20	447	41	507	23	506	21
MADEL_13	0.057	0.0022	0.653	0.045	0.0827	0.0048	100.59	482	85	512	28	509	28
MADEL_14	0.05672	0.00073	0.674	0.059	0.0861	0.0085	101.53	487	29	532	51	524	36
MADEL_15	0.0577	0.0014	0.659	0.049	0.0835	0.0052	100.39	519	53	516	31	514	30
MADEL_16	0.05745	0.00098	0.662	0.036	0.0816	0.0039	98.25	499	37	506	23	515	22
MADEL_17	0.05686	0.00085	0.669	0.059	0.0853	0.0084	101.73	475	33	528	50	519	36
MADEL_18	0.0572	0.0014	0.654	0.048	0.0831	0.0052	100.59	499	55	514	31	511	29
MADEL_19	0.05691	0.00096	0.654	0.035	0.0819	0.0039	99.22	483	36	507	23	511	21
MADEL_20	0.0568	0.0022	0.64	0.044	0.082	0.0047	101.39	475	84	509	28	502	27
MADEL_21	0.05741	0.00074	0.681	0.06	0.0859	0.0085	100.95	504	29	531	50	526	36
MADEL_22	0.0573	0.0012	0.639	0.023	0.0816	0.0034	101.00	501	46	506	20	501	14
MADEL_23	0.0571	0.0014	0.641	0.047	0.0815	0.005	100.60	484	57	505	30	502	29
MADEL_24	0.0566	0.001	0.64	0.034	0.081	0.0039	99.80	467	39	502	23	503	21
MADEL_25	0.0589	0.0023	0.674	0.047	0.0826	0.0048	97.90	556	84	512	28	523	28
MADEL_26	0.05662	0.00075	0.646	0.057	0.0824	0.0082	100.79	477	29	510	49	506	35
MADEL_27	0.0574	0.0012	0.665	0.024	0.0839	0.0035	100.39	498	45	519	21	517	15
MADEL_28	0.05691	0.00072	0.641	0.056	0.0825	0.0082	101.79	482	28	511	48	502	35
MADEL_29	0.0571	0.0012	0.664	0.024	0.0839	0.0036	100.58	483	48	519	21	516	15
MADEL_30	0.0565	0.0014	0.655	0.048	0.0841	0.0052	101.56	466	56	520	31	512	29
MADEL_31	0.0569	0.00074	0.617	0.054	0.0783	0.0077	99.59	480	28	486	46	488	34
MADEL_32	0.0568	0.0012	0.645	0.023	0.0814	0.0034	100.00	475	48	504	20	504	14

MADEL_33	0.05317	0.00092	0.615	0.034	0.0837	0.004	106.57	326	38	519	24	487	21
MADEL_34	0.0572	0.0022	0.685	0.047	0.0872	0.005	101.89	494	84	539	30	529	28
MADEL_35	0.05722	0.00076	0.578	0.051	0.0731	0.0072	98.06	493	29	455	44	464	33
MADEL_36	0.0564	0.0013	0.658	0.024	0.0846	0.0036	101.95	464	50	524	21	514	15
MADEL_37	0.05707	0.00069	0.785	0.069	0.0999	0.0099	104.24	492	27	614	58	589	39
MADEL_38	0.057	0.0014	0.694	0.051	0.0887	0.0055	102.43	481	55	547	33	534	31
MADEL_39	0.0527	0.0012	0.609	0.035	0.083	0.004	105.98	311	47	514	24	485	21
MADEL_40	0.0565	0.0021	0.652	0.044	0.0834	0.0048	101.18	474	83	516	28	510	27
MADEL_41	0.0572	0.0014	0.637	0.047	0.0811	0.005	100.60	490	53	503	30	500	29
MADEL_42	0.0522	0.0011	0.598	0.034	0.0834	0.004	108.63	284	45	516	24	475	21
MADEL_43	0.0573	0.0022	0.647	0.044	0.0818	0.0047	100.00	494	82	507	28	507	27
MADEL_44	0.0856	0.0017	0.98	0.055	0.0824	0.004	38.72	1317	38	510	23	693	28
QL-3													
MADEL_01	0.0574	0.0081	0.7	0.11	0.0873	0.0062	100.56	500	300	539	37	536	67
MADEL_02	0.057	0.017	0.67	0.17	0.086	0.012	102.12	480	650	531	72	520	100
MADEL_03	0.074	0.011	0.87	0.14	0.0875	0.0063	54.00	1000	290	540	37	634	78
MADEL_04	0.059	0.018	0.72	0.22	0.085	0.012	95.82	580	640	527	73	550	130
MADEL_05	0.0573	0.0012	0.665	0.07	0.085	0.01	101.35	493	47	524	60	517	42
MADEL_06	0.0565	0.0012	0.664	0.033	0.0852	0.0035	101.93	460	47	527	21	517	20
MADEL_07	0.0578	0.0081	0.66	0.11	0.0836	0.006	100.19	520	310	517	36	516	66
MADEL_08	0.057	0.017	0.6	0.16	0.078	0.011	100.63	480	650	483	63	480	100
MADEL_09	0.057	0.0011	0.663	0.069	0.085	0.01	101.75	481	44	524	59	515	42
MADEL_10	0.0576	0.0012	0.657	0.032	0.083	0.0034	100.39	513	46	514	20	512	20
MADEL_11	0.052	0.015	0.62	0.19	0.0845	0.0028	106.73	300	610	523	17	490	120
MADEL_12	0.0574	0.0081	0.65	0.1	0.0812	0.0058	99.02	500	310	503	35	508	65
MADEL_13	0.0568	0.0012	0.645	0.068	0.083	0.01	101.58	481	44	514	60	506	42
MADEL_14	0.0572	0.0012	0.655	0.032	0.0839	0.0035	101.37	500	46	519	21	512	20
MADEL_15	0.069	0.019	0.82	0.26	0.0855	0.0028	86.72	910	570	529	17	610	140
MADEL_16	0.0569	0.008	0.63	0.1	0.0805	0.0058	100.40	480	300	500	34	498	63
MADEL_17	0.057	0.017	0.59	0.17	0.078	0.011	102.55	460	660	482	63	470	110

MADEL_18	0.0572	0.0011	0.657	0.069	0.083	0.0096	100.00	502	43	514	57	514	42
MADEL_19	0.0567	0.0011	0.664	0.033	0.0851	0.0035	102.13	476	45	527	21	516	20
MADEL_20	0.069	0.019	0.79	0.25	0.0833	0.0027	87.46	840	560	516	16	590	140
MADEL_21	0.0564	0.008	0.64	0.1	0.081	0.0058	100.00	470	310	502	35	502	65
MADEL_22	0.057	0.017	0.59	0.17	0.078	0.011	102.77	470	660	483	67	470	110
MADEL_23	0.0572	0.0012	0.654	0.033	0.0838	0.0035	101.37	486	47	519	21	512	20
MADEL_24	0.053	0.015	0.61	0.19	0.0826	0.0027	106.46	340	610	511	16	480	120
MADEL_25	0.057	0.017	0.69	0.19	0.082	0.012	96.04	480	660	509	69	530	120
MADEL_26	0.0568	0.0012	0.649	0.032	0.0834	0.0034	101.57	476	45	517	20	509	19
MADEL_27	0.053	0.015	0.61	0.19	0.0834	0.0027	107.50	320	600	516	16	480	120
MADEL_28	0.0551	0.0078	0.65	0.11	0.0849	0.0062	103.14	410	320	525	37	509	66
MADEL_29	0.058	0.017	0.7	0.2	0.086	0.012	99.81	520	650	529	72	530	120
MADEL_30	0.0564	0.0012	0.66	0.069	0.085	0.01	102.13	455	48	527	61	516	43
MADEL_31	0.0549	0.0078	0.65	0.11	0.0855	0.0062	104.14	400	320	528	37	507	65
MADEL_32	0.057	0.017	0.66	0.16	0.085	0.012	101.74	470	670	526	71	517	98
MADEL_33	0.0568	0.0012	0.641	0.032	0.082	0.0035	101.20	489	47	508	21	502	20
MADEL_34	0.057	0.017	0.75	0.23	0.09	0.012	96.84	490	650	552	73	570	140
MADEL_35	0.0565	0.0012	0.69	0.036	0.0877	0.0039	102.07	474	47	543	23	532	21
MADEL_36	0.057	0.017	0.66	0.22	0.087	0.013	105.10	470	650	536	74	510	130
MADEL_37	0.0574	0.0013	0.68	0.035	0.0866	0.0038	101.52	503	48	535	22	527	21
MADEL_38	0.0526	0.0075	0.62	0.1	0.0847	0.0063	107.38	310	320	524	38	488	66
MADEL_39	0.0572	0.0012	0.628	0.033	0.0795	0.0035	99.60	502	47	493	21	495	20
MADEL_40	0.0531	0.0076	0.6	0.1	0.0814	0.0061	105.44	330	320	504	36	478	64
MADEL_41	0.09	0.013	1.06	0.18	0.0851	0.0064	37.11	1420	270	527	38	735	89
MADEL_42	0.057	0.017	0.61	0.21	0.079	0.012	101.88	490	660	489	71	480	130
MADEL_43	0.0581	0.0012	0.642	0.067	0.0812	0.0095	99.80	541	44	503	57	504	41
MADEL_44	0.056	0.017	0.61	0.19	0.081	0.012	105.21	460	650	505	69	480	120
MADEL_45	0.0567	0.0012	0.621	0.065	0.0789	0.0093	99.80	475	46	489	56	490	41
MADEL_46	0.057	0.017	0.65	0.19	0.082	0.012	99.02	480	650	505	70	510	120
MADEL_47	0.0572	0.0012	0.612	0.064	0.0776	0.0091	99.38	499	45	482	55	485	40

MADEL_48	0.057	0.016	0.67	0.21	0.0852	0.0028	101.35	480	620	527	17	520	130
MADEL_49	0.057	0.016	0.67	0.21	0.0843	0.0028	100.19	490	610	521	16	520	130
MADEL_50	0.057	0.016	0.65	0.2	0.0822	0.0027	99.80	500	610	509	16	510	130
CQ38S1													
MADEL_01	0.0567	0.0052	0.654	0.072	0.0833	0.0012	101.00	480	210	516.1	7.1	511	44
MADEL_02	0.0567	0.0052	0.656	0.071	0.0847	0.0013	102.20	480	200	524.3	8	513	44
MADEL_03	0.0567	0.0051	0.654	0.07	0.0832	0.0012	100.78	480	210	515	7.2	511	43
MADEL_04	0.0581	0.0053	0.666	0.073	0.0841	0.0013	100.23	520	200	520.2	7.8	519	43
MADEL_05	0.0568	0.0052	0.656	0.072	0.0848	0.0012	102.44	490	200	524.5	7.4	512	44
MADEL_06	0.0568	0.0052	0.657	0.072	0.0836	0.0013	100.88	480	200	517.5	7.6	513	44
MADEL_07	0.0566	0.0052	0.652	0.071	0.0836	0.0013	101.41	480	210	517.2	7.7	510	43
MADEL_08	0.0574	0.0053	0.662	0.071	0.0836	0.0012	100.54	500	200	517.8	7.1	515	44
MADEL_09	0.0571	0.0052	0.656	0.071	0.0837	0.0013	100.97	480	200	518	7.6	513	44
MADEL_10	0.0568	0.0052	0.658	0.07	0.0841	0.0012	101.58	490	200	521.1	7.2	513	44
MADEL_11	0.0569	0.0052	0.658	0.07	0.0833	0.0013	100.86	490	190	516.4	7.6	512	44
MADEL_12	0.0572	0.0052	0.661	0.072	0.0843	0.0012	101.09	510	210	521.6	7.1	516	43
MADEL_13	0.057	0.0052	0.657	0.071	0.083	0.0012	100.16	480	200	513.8	7.3	513	44
MADEL_14	0.0573	0.0053	0.661	0.071	0.0831	0.0013	99.92	500	210	514.6	7.7	515	44
MADEL_15	0.0567	0.0052	0.654	0.071	0.0837	0.0013	101.59	480	200	518.1	7.5	510	43
MADEL_16	0.0567	0.0052	0.658	0.071	0.0834	0.0013	100.43	480	200	516.2	7.5	514	43
MADEL_17	0.0572	0.0052	0.657	0.071	0.0834	0.0013	100.86	480	200	516.4	7.5	512	44
MADEL_18	0.0574	0.0052	0.659	0.07	0.084	0.0012	101.11	500	200	519.7	7.4	514	43
MADEL_19	0.057	0.0052	0.662	0.073	0.0837	0.0014	100.54	480	210	517.8	8.5	515	45
MADEL_20	0.0563	0.0052	0.65	0.07	0.0839	0.0012	102.34	460	200	519.9	7	508	43
MADEL_21	0.0573	0.0052	0.66	0.07	0.0828	0.0013	99.77	510	210	512.8	7.6	514	43
MADEL_22	0.0572	0.0052	0.657	0.071	0.084	0.0013	101.48	480	200	519.6	8	512	44
MADEL_23	0.0575	0.0052	0.662	0.072	0.0837	0.0012	100.45	500	200	518.3	7.5	516	44
MADEL_24	0.0568	0.0052	0.658	0.072	0.085	0.0013	102.61	480	200	526.4	7.8	513	44
MADEL_25	0.0571	0.0052	0.657	0.072	0.0839	0.0013	100.99	490	200	519.1	7.6	514	45
MADEL_26	0.0564	0.0051	0.652	0.07	0.0835	0.0013	101.57	460	200	517	7.5	509	43

MADEL_27	0.0568	0.0052	0.658	0.072	0.0829	0.0012	100.51	480	200	514.6	7.4	512	44
MADEL_28	0.0571	0.0052	0.658	0.073	0.0843	0.0014	102.01	490	200	522.3	8.2	512	44
MADEL_29	0.057	0.0052	0.657	0.071	0.084	0.0012	101.35	490	200	519.9	7	513	43
MADEL_30	0.057	0.0052	0.659	0.073	0.0837	0.0013	100.64	490	190	518.3	7.9	515	45
MADEL_31	0.0566	0.0052	0.653	0.071	0.0837	0.0013	101.77	490	210	518	7.5	509	43
MADEL_32	0.0577	0.0053	0.66	0.073	0.0832	0.0014	99.75	510	210	515.7	8.1	517	44
MADEL_33	0.0567	0.0052	0.657	0.072	0.0841	0.0014	101.78	460	200	521.1	8.2	512	45
MADEL_34	0.0573	0.0052	0.657	0.072	0.0832	0.0012	100.57	500	200	514.9	7.2	512	43
MADEL_35	0.0568	0.0052	0.657	0.073	0.0839	0.0013	101.25	490	200	519.4	7.5	513	45
MADEL_36	0.057	0.0052	0.659	0.072	0.0828	0.0012	99.75	490	210	512.7	7.1	514	44
MADEL_37	0.057	0.0052	0.656	0.071	0.0849	0.0013	102.58	480	200	525.2	8	512	44
MADEL_38	0.0569	0.0052	0.661	0.072	0.0849	0.0011	101.61	490	210	525.3	6.8	517	44
MADEL_39	0.0571	0.0052	0.655	0.071	0.0838	0.0014	100.95	490	200	518.9	8.4	514	43
MADEL_40	0.0568	0.0052	0.655	0.071	0.0841	0.0013	101.62	470	200	520.3	7.9	512	44
MADEL_41	0.0572	0.0052	0.662	0.072	0.0843	0.0017	101.32	500	190	521.8	9.8	515	44
MADEL_42	0.057	0.0052	0.659	0.072	0.0838	0.0013	100.86	490	200	518.4	7.5	514	45
MADEL_43	0.0565	0.0052	0.653	0.071	0.0835	0.0012	101.55	470	200	516.9	7.2	509	44
MADEL_44	0.0572	0.0052	0.66	0.072	0.0838	0.0012	100.54	490	200	518.8	7.4	516	45
MADEL_45	0.057	0.0052	0.657	0.072	0.0835	0.0013	100.90	480	200	516.6	7.9	512	44
MADEL_46	0.0572	0.0052	0.66	0.071	0.0841	0.0013	101.36	500	210	521	7.7	514	44
MADEL_47	0.0568	0.0052	0.653	0.072	0.0832	0.0013	101.04	490	190	515.3	7.7	510	44
MADEL_48	0.0568	0.0052	0.657	0.072	0.0836	0.0013	100.84	480	200	517.3	7.6	513	44
MADEL_49	0.0573	0.0052	0.661	0.072	0.0828	0.0012	99.51	500	200	512.5	7.2	515	44
MADEL_50	0.057	0.0052	0.655	0.071	0.0828	0.0013	100.37	480	200	512.9	7.5	511	44
MADEL_51	0.0578	0.0053	0.665	0.072	0.0837	0.0013	100.06	500	200	518.3	7.9	518	43
MADEL_52	0.0559	0.0051	0.647	0.07	0.0836	0.0014	102.27	450	200	517.5	8.2	506	43
MADEL_53	0.0576	0.0052	0.664	0.072	0.0842	0.0012	100.74	510	200	520.8	7	517	45
MADEL_54	0.0572	0.0052	0.657	0.071	0.0832	0.0012	100.68	490	200	515.5	7	512	44
MADEL_55	0.0534	0.0048	0.616	0.067	0.0838	0.0013	106.45	340	200	519.5	7.7	488	42
MADEL_56	0.0681	0.0062	0.778	0.085	0.0854	0.0013	90.46	870	190	528.3	8	584	48

MADEL_57	0.0532	0.0049	0.605	0.065	0.0833	0.0013	107.50	330	210	516	7.9	480	41
MADEL_58	0.0561	0.0051	0.658	0.071	0.0849	0.0012	102.34	440	200	525	7.5	513	44
MADEL_59	0.0572	0.0052	0.659	0.072	0.0829	0.0013	99.84	510	200	513.2	7.5	514	44
MADEL_60	0.0579	0.0053	0.664	0.071	0.084	0.0012	100.76	520	200	519.9	7.4	516	43
MADEL_61	0.0565	0.0051	0.652	0.07	0.0843	0.0013	102.35	470	210	522	7.9	510	44
MADEL_62	0.0572	0.0052	0.66	0.071	0.0842	0.0013	101.48	500	210	521.6	7.9	514	44
MADEL_63	0.0569	0.0053	0.655	0.07	0.0823	0.0013	99.59	480	200	509.9	7.8	512	43
MADEL_64	0.0568	0.0052	0.658	0.071	0.0845	0.0013	101.65	480	200	522.5	7.4	514	45
MADEL_65	0.0572	0.0052	0.66	0.072	0.0839	0.0012	100.99	490	200	519.1	7.3	514	44
MADEL_66	0.057	0.0052	0.656	0.071	0.0841	0.0013	101.30	480	210	520.7	7.6	514	44
MADEL_67	0.057	0.0052	0.66	0.071	0.0839	0.0012	100.99	490	200	519.1	7.1	514	43
MADEL_68	0.0571	0.0052	0.655	0.072	0.0832	0.0013	100.82	490	200	515.2	7.9	511	43
MADEL_69	0.0571	0.0052	0.659	0.072	0.0838	0.0013	100.86	500	190	518.4	7.8	514	44
MADEL_70	0.057	0.0051	0.659	0.072	0.0831	0.0012	99.73	500	200	514.6	7.4	516	43
MADEL_71	0.057	0.0052	0.654	0.072	0.0833	0.0013	100.94	480	200	515.8	7.6	511	43
MADEL_72	0.0569	0.0052	0.66	0.072	0.084	0.0012	101.09	480	200	519.6	7.2	514	44
MADEL_73	0.0571	0.0052	0.657	0.072	0.0833	0.0013	100.49	500	210	515.5	7.5	513	45
MADEL_74	0.0572	0.0052	0.659	0.071	0.0837	0.0013	100.82	520	200	518.2	8	514	44
MADEL_75	0.057	0.0052	0.658	0.071	0.0837	0.0013	101.05	500	200	518.4	7.7	513	43

Analysis	**$^{207}Pb/^{206}Pb$**	**2σ**	**$^{207}Pb/^{235}U$**	**2σ**	**$^{206}Pb/^{236}U$**	**2σ**	**%Conc.**	**$^{207}Pb/^{2006}Pb$ Age (Ma)**	**2σ**	**$^{206}Pb/^{238}U$ Age (Ma)**	**2σ**	**$^{207}Pb/^{235}U$ age (Ma)**	**2σ**
QL-1													
222_01	0.0557	0.0063	0.659	0.073	0.085	0.0016	102.30	440	250	525.8	9.3	514	45
222_02	--	--	0.588	0.072	0.0756	0.0047	100.21	450	180	470	28	469	46
222_03	0.056	0.015	0.51	0.18	0.0658	0.0094	97.86	440	590	411	57	420	120
222_04	0.0544	0.0094	0.75	0.17	0.0999	0.0041	107.54	380	390	613	24	570	98
222_05	0.0557	0.0055	0.54	0.11	0.071	0.013	101.61	450	220	443	77	436	75
222_06	0.0557	0.0018	0.54	0.066	0.0702	0.0087	99.54	441	70	437	53	439	43

222_07	0.0557	0.0063	0.666	0.074	0.0855	0.0016	102.05	440	250	528.6	9.3	518	45
222_08	--	--	0.573	0.071	0.0723	0.0045	97.83	470	190	450	27	460	46
222_09	0.055	0.014	0.5	0.17	0.0664	0.0095	100.98	400	600	414	57	410	120
222_10	0.0551	0.0095	0.6	0.14	0.0794	0.0032	102.93	410	390	492	19	478	88
222_11	0.0559	0.0055	0.53	0.11	0.069	0.012	100.23	450	220	431	75	430	75
222_12	0.0562	0.0018	0.545	0.067	0.0698	0.0087	98.64	460	72	435	53	441	44
222_13	0.0564	0.0064	0.66	0.073	0.0842	0.0015	101.46	470	250	521.5	9.1	514	45
222_14	--	--	0.549	0.068	0.0703	0.0044	98.65	470	190	438	27	444	45
222_15	0.055	0.015	0.5	0.17	0.0647	0.0092	98.54	430	590	404	56	410	120
222_16	0.0561	0.0097	0.57	0.13	0.0745	0.003	100.65	460	400	463	18	460	84
222_17	0.0561	0.0056	0.51	0.11	0.067	0.012	99.76	450	220	415	72	416	73
222_18	0.0555	0.0018	0.507	0.062	0.0654	0.0081	98.08	431	72	408	49	416	42
222_19	0.0549	0.0018	0.472	0.058	0.0618	0.0077	98.47	399	75	387	47	393	40
QL-2													
222_01	0.05522	0.00061	0.541	0.047	0.0711	0.007	100.91	417	24	443	42	439	31
222_02	0.0555	0.001	0.57	0.02	0.0744	0.0031	100.87	434	41	462	18	458	13
222_03	0.0559	0.0013	0.697	0.051	0.09	0.0056	103.54	443	54	556	33	537	30
222_04	0.05423	0.00082	0.512	0.028	0.0677	0.0032	100.48	376	34	422	19	420	19
222_05	0.0557	0.0021	0.528	0.036	0.0693	0.004	100.47	435	85	432	24	430	24
222_06	0.05556	0.00067	0.543	0.048	0.0712	0.007	100.68	427	27	443	42	440	31
222_07	0.0561	0.0012	0.572	0.021	0.0742	0.0031	100.43	456	46	462	18	460	13
222_08	0.0564	0.0014	0.601	0.044	0.0765	0.0047	99.37	467	54	475	28	478	28
222_09	0.05435	0.0009	0.518	0.028	0.0683	0.0032	100.71	378	37	426	19	423	19
222_10	0.0548	0.0021	0.545	0.037	0.0722	0.0041	101.58	391	86	449	25	442	24
222_11	0.05528	0.00073	0.527	0.046	0.0694	0.0069	100.70	415	30	433	41	430	31
222_12	0.0563	0.0012	0.564	0.02	0.0717	0.003	98.24	463	48	446	18	454	13
222_13	0.0554	0.0014	0.555	0.041	0.0726	0.0045	100.89	422	55	452	27	448	27
222_14	0.05401	0.00085	0.52	0.028	0.0691	0.0032	101.17	370	35	431	20	426	19
222_15	0.0561	0.0021	0.531	0.036	0.0693	0.004	100.00	456	84	432	24	432	24
QL-3													

222_01	0.053	0.015	0.51	0.16	0.0708	0.0023	105.00	310	610	441	14	420	110
222_02	0.0552	0.0078	0.531	0.086	0.0703	0.0051	101.15	410	310	438	31	433	58
222_03	0.056	0.017	0.6	0.2	0.072	0.01	93.75	430	660	450	61	480	130
222_04	0.0559	0.0012	0.571	0.059	0.0731	0.0085	99.34	444	46	455	51	458	38
222_05	0.0563	0.0011	0.558	0.028	0.0733	0.0031	101.11	460	45	456	19	451	18
222_06	0.053	0.015	0.53	0.17	0.0729	0.0024	105.35	330	620	453	14	430	110
222_07	0.054	0.0077	0.558	0.091	0.0733	0.0053	101.33	370	320	456	32	450	59
222_08	0.055	0.016	0.54	0.21	0.071	0.01	100.45	420	650	442	62	440	130
222_09	0.055	0.0012	0.563	0.059	0.075	0.0088	102.64	411	48	466	52	454	38
222_10	0.0566	0.0012	0.574	0.029	0.0744	0.0031	100.22	468	47	462	19	461	19
222_11	0.053	0.015	0.52	0.16	0.071	0.0023	105.24	310	610	442	14	420	110
222_12	0.054	0.0076	0.541	0.088	0.0726	0.0052	102.73	360	320	451	32	439	60
222_13	0.055	0.016	0.59	0.2	0.072	0.01	94.89	420	660	446	61	470	130
222_14	0.0547	0.0011	0.55	0.058	0.0732	0.0086	102.48	388	45	455	52	444	38
222_15	0.0555	0.0011	0.544	0.028	0.0715	0.003	101.13	420	44	446	18	441	18
CQ38S1													
222_01	0.0559	0.0051	0.546	0.059	0.0714	0.00098	100.59	450	200	444.6	6	442	39
222_02	0.056	0.0052	0.537	0.059	0.0721	0.001	103.22	450	200	449	6.2	435	39
222_03	0.0549	0.005	0.532	0.057	0.0715	0.001	102.96	400	210	445.8	6	433	38
222_04	0.0553	0.005	0.532	0.058	0.072	0.0011	103.73	420	210	448.1	6.4	432	38
222_05	0.0569	0.0053	0.573	0.062	0.0714	0.001	96.44	480	210	444.6	6	461	41
222_06	0.0591	0.0054	0.612	0.066	0.0721	0.001	92.96	560	190	449	6.3	483	42
222_07	0.0573	0.0052	0.562	0.061	0.0705	0.0011	97.12	490	200	439	6.4	452	40
222_08	0.0566	0.0052	0.572	0.062	0.0722	0.0011	97.86	470	200	449.2	6.3	459	40
222_09	0.0556	0.0051	0.537	0.058	0.07032	0.00096	100.71	420	200	438.1	5.8	435	39
222_10	0.0553	0.0051	0.554	0.061	0.0722	0.0011	100.29	410	210	449.3	6.3	448	40
222_11	0.0545	0.005	0.533	0.058	0.07158	0.00097	103.00	390	210	446	5.9	433	38
222_12	0.0568	0.0052	0.556	0.06	0.07149	0.00094	99.13	490	190	445.1	5.6	449	39
222_13	0.0573	0.0052	0.572	0.062	0.07209	0.00095	97.54	500	210	448.7	5.7	460	39
222_14	0.0543	0.005	0.543	0.059	0.0712	0.001	100.57	380	200	443.5	6	441	38

222_15	0.0561	0.0051	0.563	0.061	0.07217	0.00097	98.81	440	200	449.6	5.8	455	39
222_16	0.0538	0.0049	0.549	0.059	0.07155	0.00098	100.34	360	200	445.5	5.9	444	39
222_17	0.0551	0.0051	0.56	0.061	0.0723	0.0011	99.78	410	200	450	6.4	451	40
222_18	0.0558	0.0051	0.536	0.059	0.0717	0.001	102.43	430	210	446.6	6.1	436	39

Analysis	**$^{207}Pb/^{206}Pb$**	**2σ**	**$^{207}Pb/^{235}U$**	**2σ**	**$^{206}Pb/^{236}U$**	**2σ**	**%Conc.**	**$^{207}Pb/^{2006}Pb$ Age (Ma)**	**2σ**	**$^{206}Pb/^{238}U$ Age (Ma)**	**2σ**	**$^{207}Pb/^{235}U$ age (Ma)**	**2σ**
QL-1													
MtGt_01	—	—	0.605	0.076	0.077	0.0049	98.76	430	180	478	29	484	46
MtGt_02	0.06	0.016	0.38	0.13	0.0465	0.0067	88.79	560	580	293	41	330	100
MtGt_03	0.069	0.012	0.52	0.12	0.0564	0.0025	83.85	810	370	353	15	421	79
MtGt_04	0.0557	0.0058	0.36	0.077	0.0477	0.0086	96.77	410	220	300	53	310	58
MtGt_05	0.0521	0.002	0.379	0.047	0.0522	0.0065	100.92	264	79	328	40	325	35
MtGt_06	—	—	0.405	0.051	0.0523	0.0033	95.63	430	180	328	20	343	37
MtGt_07	0.062	0.016	0.4	0.14	0.0471	0.0068	87.35	650	580	297	42	340	100
MtGt_08	0.076	0.014	0.59	0.14	0.0564	0.0025	34.61	1020	370	353	15	464	87
MtGt_09	0.0609	0.0063	0.399	0.086	0.048	0.0086	88.82	600	220	302	53	340	63
MtGt_10	0.0547	0.0022	0.388	0.048	0.0511	0.0063	96.99	379	85	322	39	332	36
MtGt_11	—	—	0.427	0.053	0.0511	0.0032	88.92	600	190	321	20	361	38
MtGt_12	0.054	0.014	0.33	0.12	0.0453	0.0065	98.28	360	560	285	40	290	90
MtGt_13	0.205	0.036	2.46	0.57	0.0839	0.004	18.47	2810	320	519	24	1250	170
MtGt_14	0.0621	0.0064	0.395	0.085	0.0466	0.0084	86.69	680	220	293	52	338	62
MtGt_15	0.0548	0.0022	0.373	0.046	0.0487	0.006	95.34	384	84	307	37	322	34
MtGt_16	0.059	0.01	0.39	0.089	0.0494	0.0021	93.39	540	380	311	13	333	65
QL-2													
MtGt_01	0.0523	0.0015	0.55	0.05	0.0768	0.0076	107.19	287	58	477	46	445	33
MtGt_02	0.0539	0.0018	0.357	0.015	0.0485	0.002	98.71	344	69	305	12	309	12
MtGt_03	0.0581	0.002	0.394	0.03	0.0495	0.0031	92.58	511	73	312	19	337	22
MtGt_04	0.0533	0.0016	0.374	0.022	0.0496	0.0023	96.89	336	62	312	14	322	16

MtGt_05	0.0612	0.0029	0.414	0.031	0.0497	0.0029	89.43	630	100	313	18	350	22
MtGt_06	0.0543	0.0015	0.392	0.035	0.0519	0.0051	97.60	372	58	326	32	334	26
MtGt_07	0.0524	0.0017	0.353	0.015	0.0489	0.002	100.65	288	67	308	12	306	12
MtGt_08	0.0564	0.0022	0.391	0.031	0.0504	0.0032	95.48	412	78	317	19	332	22
MtGt_09	0.0563	0.0019	0.395	0.024	0.0505	0.0024	93.79	432	69	317	15	338	17
MtGt_10	0.0704	0.0034	0.498	0.037	0.0513	0.003	78.97	916	99	323	18	409	25
MtGt_11	0.0541	0.0013	0.372	0.033	0.0497	0.0049	97.51	367	51	313	30	321	24
MtGt_12	0.059	0.0018	0.403	0.017	0.0496	0.0021	91.23	546	69	312	13	342	12
MtGt_13	0.0637	0.0027	0.45	0.038	0.0509	0.0032	86.49	676	84	320	19	370	25
MtGt_14	0.057	0.0018	0.386	0.023	0.049	0.0023	93.05	440	64	308	14	331	17
MtGt_15	0.0597	0.003	0.408	0.031	0.0499	0.0029	90.75	540	100	314	18	346	22
QL-3													
MtGt_01	0.063	0.017	0.46	0.14	0.0537	0.0018	86.86	680	580	337	11	388	99
MtGt_02	0.0587	0.0085	0.437	0.071	0.053	0.0039	90.74	520	300	333	24	367	51
MtGt_03	0.074	0.022	0.54	0.21	0.0533	0.0078	77.91	970	600	335	48	430	130
MtGt_04	0.0808	0.0029	0.755	0.078	0.0659	0.0081	35.58	1155	83	411	49	570	46
MtGt_05	0.0616	0.0021	0.461	0.027	0.054	0.0023	88.51	639	74	339	14	383	18
MtGt_06	0.055	0.016	0.41	0.13	0.0538	0.0018	96.30	390	590	338	11	351	93
MtGt_07	0.079	0.012	0.596	0.099	0.0543	0.004	30.45	1120	300	341	24	465	63
MtGt_08	0.073	0.022	0.54	0.21	0.0553	0.008	78.86	970	630	347	49	440	140
MtGt_09	0.0691	0.005	0.56	0.13	0.0593	0.0083	82.08	856	83	371	50	452	64
MtGt_10	0.0669	0.0024	0.509	0.03	0.0557	0.0024	84.30	799	75	349	15	414	20
MtGt_11	0.055	0.015	0.39	0.12	0.0514	0.0018	96.71	360	570	323	11	334	90
MtGt_12	0.0584	0.0084	0.423	0.069	0.0523	0.0038	91.39	510	300	329	23	360	51
MtGt_13	0.076	0.023	0.27	0.28	0.0468	0.0082	28.92	1020	610	295	50	240	160
MtGt_14	0.0691	0.0027	0.539	0.06	0.0568	0.0067	82.60	847	80	356	41	431	39
MtGt_15	0.0604	0.0022	0.428	0.024	0.0521	0.0022	90.58	573	77	327	14	361	17
CQ38S1													
MtGt_01	0.0521	0.005	0.363	0.041	0.05085	0.00088	101.82	290	200	319.7	5.4	314	31
MtGt_02	0.0513	0.005	0.356	0.041	0.05149	0.00088	104.72	260	200	323.6	5.4	309	30

MtGt_03	0.0526	0.0051	0.359	0.04	0.05054	0.00085	101.53	290	200	317.8	5.2	313	30
MtGt_04	0.0616	0.0061	0.429	0.049	0.05104	0.0009	89.14	590	200	320.9	5.5	360	35
MtGt_05	0.0544	0.0052	0.382	0.043	0.05059	0.00087	96.98	380	210	318.1	5.3	328	32
MtGt_06	0.0627	0.0062	0.438	0.05	0.05142	0.00079	87.59	630	200	323.2	4.8	369	37
MtGt_07	0.0639	0.0062	0.382	0.043	0.0442	0.0013	85.09	740	190	279.1	8.3	328	31
MtGt_08	0.0535	0.0051	0.368	0.041	0.05074	0.00088	100.63	320	200	319	5.4	317	31
MtGt_09	0.0532	0.0052	0.368	0.042	0.05019	0.0008	99.25	330	200	315.6	4.9	318	31
MtGt_10	0.0512	0.005	0.36	0.041	0.05056	0.00084	101.57	240	200	317.9	5.1	313	30
MtGt_11	0.0535	0.0051	0.357	0.04	0.05011	0.00083	101.32	320	200	315.1	5.2	311	29
MtGt_12	0.055	0.0053	0.378	0.042	0.05021	0.0008	96.57	390	210	315.8	4.9	327	30
MtGt_13	0.0744	0.0078	0.528	0.065	0.05225	0.00095	77.04	980	200	328.2	5.9	426	42
MtGt_14	0.0543	0.0052	0.376	0.042	0.05067	0.00086	98.03	370	210	318.6	5.3	325	31
MtGt_15	0.0544	0.0052	0.385	0.043	0.05102	0.00085	97.48	390	200	320.7	5.2	329	32
MtGt_16	0.0543	0.0052	0.387	0.043	0.05105	0.00079	96.66	290	200	320.9	4.9	332	32
MtGt_17	0.0539	0.0052	0.393	0.044	0.05063	0.00085	95.30	350	210	318.3	5.2	334	32
MtGt_18	0.0521	0.0051	0.368	0.041	0.05052	0.00085	99.91	390	210	317.7	5.2	318	30

Analysis	**$^{207}Pb/^{206}Pb$**	**2σ**	**$^{207}Pb/^{235}U$**	**2σ**	**$^{206}Pb/^{236}U$**	**2σ**	**%Conc.**	**$^{207}Pb/^{2006}Pb$ Age (Ma)**	**2σ**	**$^{206}Pb/^{238}U$ Age (Ma)**	**2σ**	**$^{207}Pb/^{235}U$ age (Ma)**	**2σ**
QL-1													
AMBAT_01	0.0569	0.0065	0.729	0.08	0.0922	0.0017	102.34	480	250	568	10	555	47
AMBAT_02	–	–	0.695	0.085	0.0884	0.0056	101.87	460	190	546	33	536	52
AMBAT_03	0.057	0.015	0.61	0.21	0.079	0.011	101.46	470	600	487	67	480	140
AMBAT_04	0.0546	0.0094	1.07	0.25	0.1421	0.0059	115.81	390	380	857	33	740	120
AMBAT_05	0.0574	0.0057	0.59	0.13	0.076	0.014	99.79	510	220	472	82	473	80
AMBAT_06	0.0563	0.0018	0.654	0.08	0.083	0.01	100.39	450	72	514	61	512	49
AMBAT_07	0.0564	0.0064	0.704	0.078	0.0889	0.0016	101.42	470	250	548.7	9.6	541	46
AMBAT_08	–	–	0.674	0.083	0.0867	0.0055	102.49	450	190	536	32	523	50
AMBAT_09	0.057	0.015	0.63	0.22	0.079	0.011	100.20	490	600	491	68	490	140

AMBAT_10	0.0559	0.0097	0.87	0.2	0.1123	0.0047	107.19	440	380	686	27	640	110
AMBAT_11	0.0577	0.0057	0.57	0.12	0.073	0.013	99.12	510	220	451	78	455	78
AMBAT_12	0.0561	0.0018	0.65	0.08	0.084	0.01	101.57	447	73	518	62	510	50
AMBAT_13	0.0565	0.0064	0.667	0.073	0.0855	0.0016	101.83	470	250	528.5	9.7	519	45
AMBAT_14	–	–	0.663	0.082	0.0838	0.0053	100.39	490	190	519	31	517	50
AMBAT_15	0.057	0.015	0.58	0.2	0.074	0.011	99.78	480	570	459	64	460	130
AMBAT_16	0.0555	0.0096	1.09	0.25	0.1432	0.0059	115.07	430	380	863	33	750	120
AMBAT_17	0.057	0.0057	0.57	0.12	0.074	0.013	99.57	490	220	458	79	460	80
AMBAT_18	0.0558	0.0019	0.613	0.075	0.0795	0.0098	101.65	438	74	493	58	485	48
QL-2													
AMBAT_01	0.05688	0.00069	0.656	0.057	0.0842	0.0083	101.76	487	27	521	49	512	35
AMBAT_02	0.0571	0.0011	0.659	0.023	0.084	0.0035	100.97	491	44	520	21	515	14
AMBAT_03	0.0574	0.0013	0.641	0.047	0.081	0.005	99.80	503	52	502	30	503	29
AMBAT_04	0.05619	0.0008	0.624	0.033	0.0797	0.0037	100.41	458	31	494	22	492	21
AMBAT_05	0.056	0.0022	0.635	0.044	0.0827	0.0048	102.40	439	87	512	28	500	28
AMBAT_06	0.0568	0.00072	0.652	0.057	0.0837	0.0083	101.77	471	29	518	49	509	35
AMBAT_07	0.0564	0.0012	0.655	0.023	0.0835	0.0035	101.37	466	45	518	21	511	14
AMBAT_08	0.0575	0.0014	0.666	0.049	0.0846	0.0052	100.97	514	51	523	31	518	29
AMBAT_09	0.05542	0.00083	0.631	0.034	0.0807	0.0038	100.60	425	33	500	23	497	21
AMBAT_10	0.0566	0.0022	0.657	0.046	0.084	0.0048	101.57	469	87	519	28	511	28
AMBAT_11	0.05658	0.0006	0.649	0.057	0.0837	0.0083	101.97	476	23	518	49	508	35
AMBAT_12	0.056	0.0011	0.626	0.022	0.0808	0.0034	101.42	448	44	501	20	494	14
AMBAT_13	0.058	0.0014	0.641	0.047	0.0802	0.0049	99.00	527	53	497	30	502	29
AMBAT_14	0.05528	0.00082	0.626	0.034	0.0806	0.0038	101.21	415	33	500	23	494	21
AMBAT_15	0.057	0.0022	0.632	0.043	0.0806	0.0046	100.40	493	86	500	28	498	27
QL-3													
AMBAT_01	0.054	0.015	0.63	0.2	0.0838	0.0027	103.80	370	610	519	16	500	120
AMBAT_02	0.0563	0.008	0.65	0.1	0.083	0.006	101.38	460	310	514	35	507	65
AMBAT_03	0.058	0.017	0.63	0.25	0.082	0.012	101.60	510	650	508	70	500	150
AMBAT_04	0.0571	0.0012	0.695	0.073	0.088	0.01	101.87	486	48	546	61	536	45

AMBAT_05	0.0568	0.0012	0.669	0.033	0.0849	0.0036	100.96	479	46	525	21	520	21
AMBAT_06	0.054	0.015	0.62	0.2	0.0842	0.0027	106.33	360	610	521	16	490	120
AMBAT_07	0.0554	0.0078	0.65	0.11	0.0856	0.0062	103.52	420	310	529	37	511	66
AMBAT_08	0.057	0.017	0.64	0.25	0.083	0.012	102.60	480	640	513	72	500	150
AMBAT_09	0.0584	0.0012	0.692	0.072	0.086	0.01	100.00	547	46	534	60	534	44
AMBAT_10	0.0575	0.0013	0.657	0.033	0.0841	0.0036	101.56	496	48	520	21	512	20
AMBAT_11	0.054	0.015	0.62	0.19	0.0826	0.0027	104.29	370	610	511	16	490	120
AMBAT_12	0.0554	0.0078	0.66	0.11	0.0843	0.0061	101.76	420	310	521	36	512	66
AMBAT_13	0.063	0.019	0.7	0.28	0.083	0.012	94.81	680	600	512	71	540	160
AMBAT_14	0.0576	0.0013	0.652	0.068	0.083	0.0098	100.78	503	49	514	58	510	43
AMBAT_15	0.0569	0.0012	0.642	0.033	0.0821	0.0034	100.59	490	47	508	21	505	20
CQ38S1													
AMBAT_01	0.0556	0.0051	0.628	0.068	0.0829	0.0012	103.68	440	210	513.2	7	495	42
AMBAT_02	0.0578	0.0053	0.639	0.07	0.0833	0.0011	102.77	510	200	515.9	6.7	502	43
AMBAT_03	0.0556	0.0051	0.634	0.069	0.0834	0.0013	103.73	440	210	516.6	7.5	498	43
AMBAT_04	0.0568	0.0052	0.627	0.068	0.0819	0.0011	102.94	470	200	507.5	6.5	493	43
AMBAT_05	0.081	0.0074	0.96	0.1	0.0864	0.0012	43.80	1220	180	534.3	7.4	680	54
AMBAT_06	0.0785	0.0071	0.93	0.1	0.0849	0.0011	45.34	1160	180	526	6.8	665	53
AMBAT_07	0.0573	0.0052	0.652	0.071	0.0826	0.0011	100.47	500	200	511.4	6.5	509	44
AMBAT_08	0.057	0.0052	0.651	0.071	0.0827	0.0011	100.59	480	200	512	6.8	509	45
AMBAT_09	0.056	0.0051	0.635	0.069	0.0826	0.0011	102.34	450	210	511.7	6.8	500	42
AMBAT_10	0.0577	0.0053	0.658	0.071	0.0821	0.0012	98.97	530	200	508.7	7.3	514	43
AMBAT_11	0.0564	0.0051	0.64	0.069	0.0824	0.0011	101.65	480	210	510.3	6.4	502	43
AMBAT_12	0.0582	0.0053	0.662	0.072	0.083	0.0011	99.65	540	200	514.2	6.5	516	43
AMBAT_13	0.0581	0.0053	0.657	0.071	0.0834	0.0011	100.58	530	200	516	6.3	513	46
AMBAT_14	0.0561	0.0051	0.649	0.071	0.0826	0.0012	100.75	460	210	511.8	6.9	508	44
AMBAT_15	0.0558	0.0051	0.655	0.071	0.084	0.0011	101.54	440	210	519.9	6.7	512	43
AMBAT_16	0.0561	0.0051	0.666	0.072	0.0832	0.0011	99.48	440	200	515.3	6.4	518	43
AMBAT_17	0.0551	0.005	0.66	0.071	0.083	0.0011	99.75	410	200	513.7	6.6	515	43
AMBAT_18	0.0571	0.0052	0.633	0.069	0.0824	0.0011	102.70	500	200	510.4	6.9	497	43

APPENDIX H: U–Pb geochronology zircon results

Analysis	$^{207}Pb/^{206}Pb$	2σ	$^{207}Pb/^{235}U$	2σ	$^{206}Pb/^{236}U$	2σ	%Conc.	$^{207}Pb/^{2006}Pb$ Age (Ma)	2σ	$^{206}Pb/^{238}U$ Age (Ma)	2σ	$^{207}Pb/^{235}U$ age (Ma)	2σ
QL-3													
QL3_01	0.0573	0.0037	0.591	0.037	0.0754	0.0019	99.15	450	130	468	11	472	24
QL3_02	0.055	0.0037	0.56	0.035	0.0747	0.0019	103.33	350	130	465	12	450	23
QL3_03	0.0638	0.0045	1.163	0.077	0.1312	0.0035	101.27	740	140	796	20	786	35
QL3_04	0.057	0.0034	0.582	0.033	0.0744	0.0018	99.35	470	120	462	11	465	20
QL3_05	0.0651	0.0038	1.262	0.069	0.1448	0.0037	105.18	720	120	873	21	830	31
QL3_06	0.0757	0.0036	1.808	0.082	0.1782	0.0037	98.69	1070	100	1056	20	1053	30
QL3_07	0.0531	0.0061	0.495	0.054	0.0701	0.0025	100.00	240	210	436	15	436	36
QL3_08	0.0685	0.0049	1.234	0.083	0.1332	0.0043	100.25	750	150	804	24	802	38
QL3_09	0.0672	0.0032	1.527	0.069	0.1663	0.0032	105.43	853	99	991	18	940	28
QL3_10	0.0818	0.0036	2.63	0.11	0.2263	0.0046	104.96	1251	92	1313	24	1311	31
QL3_11	0.0522	0.004	0.557	0.039	0.0768	0.002	107.45	270	140	476	12	443	26
QL3_12	0.067	0.0029	1.322	0.057	0.1451	0.0033	102.11	846	95	872	19	854	25
QL3_13	0.1155	0.0055	5.43	0.23	0.3419	0.008	101.67	1861	85	1892	38	1890	37
QL3_14	0.177	0.0071	12.8	0.49	0.518	0.011	103.13	2617	67	2699	48	2662	36
QL3_15	0.0836	0.0041	2.58	0.12	0.2241	0.0049	101.40	1289	93	1307	26	1290	35
QL3_16	0.157	0.0068	10.17	0.4	0.471	0.011	102.85	2417	78	2486	48	2442	38
QL3_17	0.0647	0.0034	1.216	0.063	0.1349	0.0027	100.87	730	120	815	15	808	29
QL3_18	0.0685	0.0046	1.493	0.099	0.1559	0.0038	100.65	790	140	933	21	927	40
QL3_19	0.1555	0.0079	9.43	0.47	0.431	0.011	96.37	2395	88	2308	52	2370	48
QL3_20	0.0661	0.0037	1.245	0.063	0.1378	0.0033	101.09	760	120	831	19	822	28
QL3_21	0.0605	0.0056	0.749	0.067	0.0895	0.003	99.28	490	170	552	18	556	39
QL3_22	0.1255	0.0047	6.69	0.25	0.3819	0.0075	102.36	2034	67	2082	34	2077	33
QL3_23	0.0989	0.0043	3.94	0.16	0.2857	0.0056	101.00	1605	75	1621	28	1615	33
QL3_24	0.0667	0.0041	1.452	0.089	0.1518	0.0041	100.33	780	130	910	23	907	36

QL3_25	0.0696	0.0042	1.538	0.087	0.1594	0.0039	100.74	840	130	954	21	947	36
QL3_26	0.0617	0.0033	0.907	0.051	0.1067	0.0028	99.85	660	110	653	16	654	27
QL3_27	0.0637	0.0027	0.996	0.048	0.1157	0.0034	100.57	720	94	705	20	701	24
QL3_28	0.0593	0.0024	0.712	0.04	0.088	0.0033	99.82	585	90	544	19	545	22
QL3_29	0.0583	0.0041	0.539	0.035	0.0693	0.0019	99.54	480	140	431	11	433	23
QL3_30	0.063	0.0041	1.207	0.072	0.1402	0.0034	106.56	620	130	845	19	793	33
QL3_31	0.0553	0.0034	0.546	0.033	0.0711	0.0015	99.86	390	130	442.4	9.3	443	21
QL3_32	0.055	0.0039	0.494	0.036	0.0655	0.0019	100.24	400	140	411	11	410	23
QL3_33	0.0629	0.0036	1.192	0.061	0.136	0.003	103.27	670	120	821	17	795	28
QL3_34	0.0668	0.0034	1.242	0.057	0.1373	0.003	100.73	800	110	828	17	822	27
QL3_35	0.0548	0.0037	0.563	0.034	0.075	0.0017	102.87	330	130	466	10	453	22
QL3_36	0.0609	0.0063	0.577	0.056	0.0736	0.0031	98.50	480	190	459	19	466	35
QL3_37	0.074	0.0042	1.859	0.098	0.1803	0.0046	105.64	1010	120	1067	25	1066	35
QL3_38	0.07	0.004	1.534	0.086	0.1591	0.0035	100.53	900	120	951	19	946	35
QL3_39	0.064	0.0039	1.132	0.065	0.1251	0.0033	99.35	740	120	761	19	766	31
QL3_40	0.0557	0.0055	1.02	0.1	0.1355	0.0048	113.36	440	180	823	28	726	50
QL3_41	0.065	0.004	1.173	0.071	0.1311	0.0036	101.28	690	130	793	20	783	33
QL3_42	0.065	0.0034	0.832	0.062	0.0925	0.0046	92.99	800	100	570	26	613	30
QL3_43	0.0554	0.003	0.589	0.03	0.0762	0.0017	100.85	400	110	473	10	469	20
QL3_44	0.0548	0.0035	0.57	0.035	0.0761	0.0018	103.06	350	120	472	11	458	22
QL3_45	0.0516	0.0044	0.516	0.04	0.0741	0.0023	109.00	240	160	460	14	422	27
QL3_46	0.0679	0.004	1.413	0.073	0.1527	0.0034	102.69	830	120	915	19	891	30
QL3_47	0.0635	0.003	1.24	0.055	0.1402	0.0029	104.06	720	100	845	16	812	25
QL3_48	0.0568	0.0072	0.545	0.065	0.073	0.0031	108.85	210	210	455	19	418	44
QL3_49	0.0624	0.0038	1.126	0.065	0.1313	0.0032	104.61	640	130	794	18	759	31
QL3_50	0.0653	0.0034	1.189	0.059	0.1307	0.0029	100.51	720	120	793	16	789	27
QL3_51	0.0659	0.0045	1.1	0.072	0.1198	0.0027	97.85	790	140	729	15	745	35
QL3_52	0.0623	0.0039	1.172	0.069	0.1341	0.003	103.58	670	130	810	17	782	32
QL3_53	0.0901	0.0042	3	0.18	0.246	0.012	100.50	1410	100	1417	63	1396	59
QL3_54	0.0964	0.0053	3.65	0.19	0.2773	0.0066	102.94	1530	100	1575	33	1550	43

QL3_55	0.0644	0.0039	1.188	0.066	0.1325	0.003	101.01	720	130	802	17	794	31
QL3_56	0.064	0.0027	1.186	0.054	0.1323	0.0037	100.50	772	91	800	21	796	24
QL3_57	0.0626	0.003	1.131	0.05	0.1281	0.0027	100.91	680	98	777	16	770	23
QL3_58	0.0709	0.0042	1.592	0.09	0.1631	0.0044	101.14	910	120	972	24	961	36
QL3_59	0.0625	0.0041	1.178	0.073	0.1365	0.0035	103.52	660	140	824	20	796	34
QL3_60	0.0654	0.0034	1.214	0.057	0.1333	0.0026	100.50	770	110	808	15	804	27
QL3_61	0.0661	0.0031	1.223	0.055	0.1355	0.0022	100.61	807	99	820	12	815	24
QL3_62	0.0636	0.0027	1.1	0.046	0.1266	0.0022	101.86	725	89	768	12	754	22
QL3_63	0.0654	0.003	1.19	0.049	0.1315	0.0024	100.76	767	99	798	14	792	23
QL3_64	0.066	0.0028	1.235	0.05	0.1354	0.0024	100.00	796	86	818	14	818	22
QL3_65	0.0711	0.0059	1.5	0.11	0.1591	0.0046	102.59	790	170	950	26	926	46
QL3_66	0.0738	0.0049	1.71	0.1	0.168	0.0041	100.40	950	130	1003	23	999	36
QL3_67	0.0834	0.0055	2.73	0.17	0.245	0.0072	113.63	1240	130	1409	37	1352	46
QL3_68	0.1017	0.0061	4.4	0.23	0.3204	0.008	110.56	1620	110	1791	39	1715	46
QL3_69	0.066	0.0042	1.188	0.073	0.1313	0.0034	101.02	770	130	795	19	787	34
QL3_70	0.0897	0.0043	3.09	0.14	0.2498	0.0052	102.42	1404	92	1438	26	1428	36
QL3_71	0.064	0.0032	1.192	0.058	0.1348	0.003	102.51	730	110	816	17	796	26
QL3_72	0.0668	0.003	1.172	0.051	0.1302	0.0022	100.51	810	92	789	12	785	23
QL3_73	0.0966	0.0043	3.66	0.15	0.2768	0.006	101.55	1549	85	1573	30	1562	33
QL3_74	0.0615	0.0048	0.844	0.061	0.1046	0.0034	101.10	560	160	641	20	634	35
QL3_75	0.0539	0.0031	0.522	0.03	0.069	0.0014	100.44	330	120	429.9	8.5	428	19
QL3_76	0.0648	0.0035	1.174	0.058	0.1319	0.0031	101.66	710	120	798	18	785	27
QL3_77	0.0643	0.0028	1.108	0.044	0.1249	0.0021	99.61	743	92	758	12	761	20
QL3_78	0.0587	0.0047	0.665	0.058	0.0799	0.003	98.02	560	160	495	18	505	36
QL3_79	0.0589	0.0044	0.584	0.041	0.07	0.0021	92.96	530	140	436	13	469	27
QL3_80	0.0994	0.0046	3.92	0.18	0.2859	0.0065	100.75	1606	92	1618	33	1614	36
QL3_81	0.067	0.0035	1.516	0.073	0.1616	0.0032	103.42	830	110	967	18	935	30
QL3_82	0.1058	0.0066	4.41	0.26	0.302	0.01	98.03	1730	120	1696	52	1714	49
QL3_83	0.0636	0.0033	1.159	0.057	0.1304	0.003	101.41	690	110	789	17	778	27
QL3_84	0.0783	0.0055	2.1	0.14	0.1936	0.0065	105.28	1080	140	1137	35	1139	44

QL3_85	0.0641	0.0038	1.159	0.063	0.1332	0.0035	103.07	680	130	805	20	781	30
QL3_86	0.067	0.0049	1.187	0.091	0.1303	0.0048	99.62	760	150	788	27	791	41
QL3_87	0.066	0.0031	1.243	0.053	0.1353	0.0027	100.00	780	100	817	15	817	25
QL3_88	0.0544	0.0031	0.547	0.03	0.0729	0.0017	102.03	350	110	453	10	444	19
QL3_89	0.0665	0.0066	1.19	0.11	0.1322	0.0047	102.03	680	190	804	27	788	52
QL3_90	0.099	0.014	4.95	0.63	0.345	0.019	118.26	1610	240	1904	90	1850	99
QL3_91	0.0607	0.0068	1.11	0.12	0.1355	0.0047	103.80	530	210	820	27	790	55
QL3_92	0.0661	0.0051	1.18	0.088	0.1309	0.0039	99.12	750	150	792	22	799	40
QL3_93	0.0698	0.0041	1.438	0.086	0.1479	0.0041	99.22	870	120	892	23	899	35
QL3_94	0.0769	0.0038	1.949	0.091	0.1842	0.0041	97.59	1120	100	1093	22	1090	32
QL3_95	0.0619	0.0087	0.559	0.074	0.0662	0.003	97.63	430	250	412	18	422	50
QL3_96	0.0646	0.0054	1.268	0.086	0.138	0.0037	99.88	780	140	833	21	834	38
QL3_97	0.0543	0.0031	0.524	0.029	0.0692	0.0017	101.41	360	120	431	10	425	19
QL3_98	0.0986	0.0052	4.13	0.21	0.3011	0.0077	108.09	1570	100	1697	38	1642	42
QL3_99	0.065	0.0031	1.227	0.053	0.1344	0.0029	100.37	750	100	812	16	809	24
QL3_100	0.0545	0.0032	0.518	0.027	0.0693	0.0014	100.89	370	110	431.8	8.3	428	17
QL3_101	0.1158	0.0059	5.56	0.28	0.345	0.0081	101.11	1886	96	1907	40	1904	44
QL3_102	0.1159	0.0057	2.8	0.16	0.1727	0.005	53.66	1912	81	1026	27	1352	38
QL3_103	0.1196	0.0083	3.28	0.23	0.1991	0.007	60.47	1930	120	1167	37	1469	54
QL3_104	0.1692	0.0074	10.79	0.47	0.459	0.011	96.14	2536	73	2438	48	2507	43
QL3_105	0.169	0.0067	11.58	0.5	0.498	0.012	101.80	2554	67	2600	52	2572	37
QL3_106	0.0609	0.0042	0.621	0.039	0.0722	0.0022	92.42	620	140	451	13	488	25
QL3_107	0.058	0.0035	0.604	0.036	0.0757	0.0016	98.76	460	120	470.1	9.7	476	23
QL3_108	0.1116	0.0048	4.92	0.21	0.3219	0.005	97.35	1846	73	1797	24	1795	36
QL3_109	0.0669	0.0038	1.186	0.063	0.1316	0.0025	99.75	800	110	796	14	798	30
QL3_110	0.0699	0.0038	1.568	0.075	0.1601	0.0031	100.10	900	110	956	17	955	29
QL3_111	0.0669	0.0041	1.194	0.074	0.1314	0.0031	100.13	780	120	795	17	794	33
QL3_112	0.0714	0.0038	1.633	0.08	0.1638	0.0036	100.10	940	110	981	20	980	30
QL3_113	0.0665	0.0033	1.092	0.056	0.1175	0.0031	95.84	800	100	715	18	746	26
QL3_114	0.0548	0.0037	0.503	0.031	0.0667	0.0017	101.22	370	130	416	10	411	21

QL3_115	0.0658	0.0027	1.163	0.045	0.1282	0.0024	99.23	789	85	777	14	783	21
QL3_116	0.0642	0.0029	1.249	0.053	0.139	0.0026	102.20	743	96	838	15	820	24
QL3_117	0.0646	0.003	1.223	0.054	0.1356	0.0029	100.61	752	96	819	16	814	24
QL3_118	0.065	0.004	1.191	0.071	0.133	0.0034	100.88	710	130	804	19	797	33
QL3_119	0.0575	0.0084	0.527	0.074	0.0728	0.0029	112.16	200	250	452	17	403	51
QL3_120	0.056	0.0046	0.53	0.043	0.0684	0.002	100.00	410	160	426	12	426	28
QL3_121	0.0578	0.0045	0.579	0.044	0.0723	0.0019	96.99	470	150	451	12	465	27
QL3_122	0.0724	0.0044	1.694	0.099	0.1671	0.0045	99.60	940	130	994	25	998	37
QL3_123	0.1711	0.0067	10.38	0.36	0.444	0.01	92.57	2557	63	2367	47	2473	35
QL3_124	0.0732	0.0038	1.67	0.1	0.1629	0.0062	95.10	1020	100	970	34	991	36
QL3_125	0.0507	0.0052	0.462	0.044	0.0671	0.0021	105.82	190	180	418	13	395	28
QL3_126	0.061	0.0067	0.556	0.061	0.0682	0.0025	98.84	440	210	425	15	430	41
QL3_127	0.0659	0.0046	1.228	0.082	0.134	0.0034	99.75	760	140	809	20	811	37
QL3_128	0.0667	0.0031	1.296	0.055	0.1396	0.0029	99.76	824	99	842	16	844	25
QL3_129	0.0664	0.006	1.159	0.094	0.1293	0.0043	99.36	690	170	782	24	787	43
QL3_130	0.0641	0.0028	1.152	0.054	0.1289	0.0035	100.64	739	92	781	20	776	25
QL3_131	0.063	0.0029	1.124	0.051	0.1265	0.0025	100.52	700	100	768	14	764	24
QL3_132	0.0557	0.0027	0.532	0.024	0.0704	0.0016	101.25	420	110	438.4	9.5	433	17
QL3_133	0.064	0.0034	1.308	0.064	0.1462	0.0033	104.27	700	110	880	19	844	28
QL3_134	0.0662	0.0044	1.231	0.073	0.135	0.0034	100.62	740	140	817	19	812	33
QL3_135	0.0654	0.0029	1.262	0.052	0.1378	0.0028	100.73	799	89	833	16	827	24
QL3_136	0.0539	0.0037	0.508	0.034	0.068	0.0019	100.71	350	140	424	11	421	23
QL3_137	0.0522	0.0048	0.486	0.043	0.0677	0.0021	106.84	250	160	422	12	395	29
QL3_138	0.1427	0.0063	8.17	0.34	0.408	0.0093	97.57	2264	75	2209	42	2248	36
QL3_139	0.093	0.026	0.54	0.13	0.0628	0.0054	121.30	90	460	393	33	324	90
2QS2													
2QS2_01	0.0776	0.0071	1.95	0.2	0.1828	0.0045	94.82	1140	170	1081	25	1096	68
2QS2_02	0.159	0.012	8.65	0.78	0.3913	0.0061	87.17	2440	130	2127	28	2299	81
2QS2_03	0.1161	0.0094	2.62	0.25	0.1632	0.0049	51.21	1900	140	973	27	1299	71
2QS2_04	0.053	0.005	0.414	0.051	0.0569	0.0025	100.85	330	200	356	15	353	33

2QS2_05	0.0639	0.0066	1.16	0.13	0.1125	0.004	87.61	960	210	686	23	783	59
2QS2_06	0.114	0.0092	2.65	0.26	0.1656	0.0052	53.46	1850	150	989	29	1303	76
2QS2_07	0.0708	0.006	1.47	0.14	0.149	0.0035	98.25	930	180	898	19	914	57
2QS2_08	0.0738	0.007	1.64	0.17	0.1653	0.0066	100.41	960	190	984	37	980	68
2QS2_09	0.145	0.012	8.2	0.75	0.4119	0.0069	97.25	2290	140	2227	32	2256	81
2QS2_10	0.1113	0.0091	4.92	0.46	0.3258	0.007	100.28	1810	150	1815	34	1807	76
2QS2_11	0.0537	0.0049	0.498	0.051	0.0662	0.0019	100.73	340	190	413	11	410	35
2QS2_12	0.16	0.013	8.58	0.8	0.3928	0.0096	87.51	2450	140	2144	45	2302	84
2QS2_13	0.0871	0.007	2.12	0.2	0.1756	0.0046	76.84	1360	160	1045	25	1152	65
2QS2_14	0.0686	0.0055	0.959	0.089	0.101	0.0018	90.92	880	170	621	11	683	46
2QS2_15	0.0655	0.0059	1.16	0.12	0.1282	0.0028	99.49	760	200	777	16	781	57
2QS2_16	0.0504	0.0051	0.511	0.055	0.0742	0.0018	111.35	200	190	461	11	414	37
2QS2_17	0.095	0.0082	3.51	0.34	0.269	0.006	100.26	1530	170	1534	30	1530	75
2QS2_18	0.0586	0.0047	0.705	0.064	0.0874	0.0014	99.63	540	180	541	8.4	543	38
2QS2_19	0.0552	0.0063	0.515	0.066	0.0671	0.0025	99.29	380	230	419	15	422	43
2QS2_20	0.0748	0.0064	1.91	0.18	0.1825	0.0038	102.26	1060	180	1084	21	1081	64
2QS2_21	0.196	0.016	15.4	1.4	0.569	0.013	103.94	2790	140	2900	51	2849	88
2QS2_22	0.1223	0.0097	4.32	0.39	0.2573	0.0046	74.12	1990	140	1475	24	1694	73
2QS2_23	0.1086	0.0088	3.71	0.35	0.2474	0.0073	79.94	1780	150	1423	38	1572	74
2QS2_24	0.127	0.01	5.44	0.5	0.3158	0.0057	86.67	2040	140	1768	28	1897	78
2QS2_25	0.0558	0.0059	0.495	0.056	0.0632	0.0021	97.77	460	230	395	12	404	38
2QS2_26	0.178	0.015	12.2	1.1	0.5	0.013	99.43	2620	140	2605	55	2615	85
2QS2_27	0.0746	0.0078	1.16	0.13	0.129	0.0039	100.64	710	210	781	22	776	58
2QS2_28	0.1002	0.0083	3.88	0.37	0.28	0.0064	98.52	1620	160	1596	34	1607	78
2QS2_29	0.0603	0.0052	0.718	0.071	0.0867	0.0019	99.08	570	170	536	11	541	37
2QS2_30	0.0764	0.0081	1.82	0.21	0.1762	0.0078	95.87	1090	210	1045	43	1050	73
2QS2_31	0.0709	0.0062	1.32	0.13	0.1342	0.0048	95.52	950	180	811	27	849	57
2QS2_32	0.0723	0.0064	1.67	0.17	0.1682	0.0053	99.01	1010	180	1000	29	995	64
2QS2_33	0.0653	0.0054	1.21	0.11	0.1335	0.0028	100.87	800	160	808	16	801	52
2QS2_34	0.1001	0.0095	1.85	0.2	0.1349	0.0037	50.62	1610	190	815	21	1045	69

2QS2_35	0.0683	0.007	1.23	0.13	0.1354	0.0049	100.00	830	200	818	28	818	60
2QS2_36	0.1004	0.0085	3.73	0.35	0.2721	0.0059	95.40	1630	170	1555	31	1577	77
2QS2_37	0.0731	0.0062	1.44	0.14	0.1432	0.004	85.35	1010	170	862	22	905	54
2QS2_38	0.0772	0.0076	1.21	0.13	0.1153	0.0032	64.50	1090	190	703	19	801	58
2QS2_39	0.162	0.015	9.52	0.98	0.433	0.016	93.64	2470	160	2313	72	2388	92
2QS2_40	0.0781	0.0081	1.79	0.2	0.1754	0.0061	95.50	1090	220	1041	33	1034	74
2QS2_41	0.0909	0.0084	3.3	0.33	0.2639	0.0064	107.71	1400	180	1508	33	1471	81
2QS2_42	0.0674	0.0056	0.677	0.063	0.0734	0.0017	87.05	850	180	457	10	525	39
2QS2_43	0.152	0.012	4.2	0.39	0.204	0.0051	50.46	2370	140	1196	27	1670	76
2QS2_44	0.0923	0.0083	1.81	0.18	0.1423	0.0063	57.91	1480	160	857	36	1048	64
2QS2_45	0.0681	0.0055	1.34	0.12	0.1423	0.0025	99.65	870	170	857	14	860	54
4QS4													
4QS4_04	0.186	0.0086	13.67	0.76	0.526	0.017	100.85	2703	76	2726	72	2726	54
4QS4_06	0.2225	0.0096	11.04	0.57	0.357	0.01	65.64	2998	70	1968	48	2528	50
4QS4_21	0.1035	0.0046	3.96	0.21	0.2751	0.0082	93.15	1680	81	1565	41	1628	43
4QS4_18	0.1452	0.0077	3.72	0.23	0.1804	0.0072	46.31	2306	88	1068	39	1568	51
4QS4_13	0.0841	0.0077	2.52	0.24	0.216	0.0089	103.20	1220	190	1259	47	1265	68
4QS4_12	0.0938	0.0078	2.43	0.23	0.1839	0.0087	71.05	1530	170	1087	47	1248	71
4QS4_03	0.0888	0.0044	2.25	0.13	0.1857	0.0077	78.65	1396	97	1098	42	1195	40
4QS4_11	0.1113	0.0053	2.17	0.12	0.1413	0.0042	47.05	1811	89	852	24	1178	39
4QS4_31	0.0739	0.0039	1.79	0.1	0.1751	0.005	98.11	1060	100	1040	27	1043	37
4QS4_27	0.0754	0.0072	1.77	0.15	0.1721	0.0078	100.29	980	180	1022	43	1019	57
4QS4_26	0.0775	0.0039	1.69	0.1	0.1539	0.0056	82.97	1110	100	921	31	1003	40
4QS4_07	0.0712	0.0036	1.655	0.093	0.1666	0.0048	100.61	970	100	995	26	989	35
4QS4_02	0.0716	0.0042	1.65	0.11	0.166	0.007	100.51	960	120	989	39	984	42
4QS4_15	0.0699	0.0034	1.492	0.089	0.1556	0.0056	100.87	923	97	931	31	923	36
4QS4_22	0.0681	0.0036	1.477	0.086	0.1547	0.0045	100.65	890	110	927	26	921	35
4QS4_19	0.0675	0.0062	1.2	0.1	0.1307	0.0066	99.75	810	190	794	38	796	47
4QS4_28	0.0667	0.0036	1.171	0.075	0.1301	0.0041	99.87	800	120	788	24	789	35
4QS4_25	0.0645	0.0036	1.111	0.068	0.1242	0.0036	99.34	740	120	754	21	759	32

4QS4_29	0.0681	0.0031	1.094	0.058	0.1157	0.0033	94.26	884	93	706	19	749	29
4QS4_20	0.0649	0.0035	1.066	0.062	0.1169	0.0038	96.48	740	120	712	22	738	31
4QS4_30	0.0714	0.0044	1.063	0.068	0.1076	0.0037	89.65	970	130	658	22	734	33
4QS4_08	0.0627	0.0048	1.022	0.081	0.1173	0.0045	100.42	640	160	714	26	711	42
4QS4_05	0.0703	0.0039	1.018	0.064	0.1024	0.004	87.71	920	110	628	23	716	32
4QS4_24	0.0625	0.003	0.748	0.042	0.0858	0.0024	93.65	683	98	531	14	567	24
4QS4_10	0.0678	0.0033	0.719	0.042	0.0766	0.0022	86.08	862	98	476	13	553	24
4QS4_09	0.0565	0.0028	0.603	0.035	0.0771	0.0022	99.79	470	110	479	13	480	22
4QS4_01	0.0547	0.0041	0.539	0.041	0.0702	0.0024	100.23	380	150	437	14	436	28
4QS4_14	0.0526	0.0045	0.53	0.047	0.073	0.0027	106.07	270	160	454	16	428	31
4QS4_23	0.0568	0.0028	0.379	0.022	0.0474	0.0014	91.53	490	110	298.4	8.6	326	16
CQ38S1													
CQ38_01	0.0573	0.0076	0.525	0.082	0.0656	0.0056	96.25	500	190	411	32	427	41
CQ38_02	0.0976	0.0061	2.65	0.16	0.2006	0.0046	75.10	1570	120	1179	25	1309	44
CQ38_03	0.055	0.004	0.502	0.034	0.066	0.0013	99.54	410	140	412.1	7.8	414	23
CQ38_04	0.0579	0.0042	0.576	0.063	0.0734	0.0042	99.13	500	140	457	24	461	35
CQ38_05	0.06	0.0037	0.641	0.037	0.0765	0.0013	95.21	570	120	475.1	7.9	499	21
CQ38_06	0.0722	0.0042	0.726	0.04	0.0718	0.0011	44.67	1000	120	446.7	6.7	553	24
CQ38_07	0.0579	0.0032	0.606	0.03	0.0746	0.001	96.63	510	120	463.8	6	480	19
CQ38_08	0.0613	0.0034	0.563	0.029	0.06696	0.00096	92.00	640	120	417.7	5.8	454	18
CQ38_09	0.0596	0.0032	0.591	0.029	0.07151	0.00095	94.12	590	120	445.2	5.7	473	18
CQ38_10	0.0571	0.0033	0.564	0.03	0.07157	0.00096	98.13	470	120	445.5	5.8	454	20
CQ38_11	0.0858	0.0048	2.42	0.13	0.2021	0.0038	88.30	1350	110	1192	21	1249	39
CQ38_12	0.0561	0.0032	0.591	0.033	0.0764	0.0014	100.57	460	130	474.7	8.7	472	20
CQ38_13	0.0788	0.0045	1.494	0.097	0.1366	0.0048	71.57	1150	110	823	27	927	40
CQ38_14	0.0567	0.0033	0.623	0.033	0.0787	0.0011	99.65	470	120	488.3	6.8	490	20
CQ38_15	0.0577	0.0037	0.501	0.03	0.0616	0.0011	93.93	530	140	385.1	6.8	410	20
CQ38_16	0.0596	0.0033	0.638	0.033	0.0768	0.0012	94.96	580	120	476.7	6.9	502	20
CQ38_17	0.0865	0.0049	2.17	0.15	0.1829	0.0067	81.20	1330	110	1080	36	1169	49
CQ38_18	0.0742	0.004	1.012	0.05	0.0984	0.0011	58.17	1040	110	605	6.4	710	26

CQ38_19	0.0621	0.0037	0.576	0.032	0.0673	0.0011	90.67	660	130	419.8	6.4	463	21
CQ38_20	0.0576	0.0036	0.639	0.038	0.0782	0.0014	97.10	500	120	485.5	8.3	500	23
CQ38_21	0.0564	0.0035	0.5	0.028	0.06523	0.00096	98.83	430	130	407.2	5.8	412	19
CQ38_22	0.0554	0.0033	0.536	0.028	0.07058	0.00095	101.29	420	120	439.6	5.7	434	19
CQ38_23	0.0614	0.0044	0.56	0.12	0.0646	0.0075	89.58	680	120	404	43	451	54
CQ38_24	0.0598	0.0032	0.549	0.027	0.06653	0.00091	93.49	590	110	415.1	5.5	444	18
CQ38_25	0.0977	0.006	3.45	0.21	0.2566	0.0063	92.97	1580	110	1469	33	1510	48
CQ38_26	0.0577	0.0034	0.648	0.037	0.0811	0.0014	99.31	500	130	502.5	8.4	506	23
CQ38_27	0.0569	0.0032	0.472	0.025	0.06034	0.0008	95.96	480	120	378.1	4.8	394	17
CQ38_28	0.0565	0.0034	0.508	0.028	0.06442	0.00076	96.96	450	130	402.4	4.6	415	19
CQ38_29	0.0573	0.0034	0.576	0.033	0.0723	0.0015	98.02	480	130	449.9	9.1	459	21
CQ38_30	0.057	0.0031	0.612	0.032	0.0771	0.001	98.50	490	120	478.7	6.1	486	20
CQ38_31	0.0555	0.0031	0.447	0.025	0.05921	0.00083	99.14	400	120	370.8	5	374	17
CQ38_32	0.078	0.0056	0.651	0.043	0.06011	0.00096	32.43	1160	150	376.2	5.8	511	26
CQ38_33	0.0687	0.0039	1.031	0.052	0.1085	0.0016	92.28	880	120	664.4	9.4	720	26
CQ38_34	0.0993	0.0079	1.36	0.45	0.098	0.017	37.12	1630	110	605	91	875	97
CQ38_35	0.0556	0.0033	0.523	0.03	0.06859	0.00095	100.14	410	130	427.6	5.7	427	20
CQ38_36	0.0618	0.0038	0.731	0.042	0.0855	0.0014	94.60	650	140	528.8	8.4	559	25
CQ38_37	0.0642	0.0035	0.986	0.05	0.1121	0.0014	98.36	730	120	685.6	8.3	697	25
CQ38_38	0.0661	0.0039	0.665	0.042	0.0723	0.0015	87.70	810	120	449.9	9	513	25
CQ38_39	0.0597	0.0034	0.62	0.033	0.0763	0.0015	96.89	590	120	473.8	9.1	489	21
CQ38_40	0.069	0.0041	1.381	0.089	0.1453	0.004	99.89	880	130	875	23	876	37
CQ38_41	0.0683	0.0035	1.379	0.065	0.1452	0.0014	99.31	880	110	873.9	7.7	880	27
CQ38_42	0.0728	0.0044	1.428	0.081	0.1431	0.0036	95.67	980	130	862	21	901	37
CQ38_43	0.0601	0.0033	0.699	0.035	0.0838	0.0012	96.72	590	120	519.4	7	537	21
CQ38_44	0.0556	0.0037	0.465	0.036	0.0621	0.002	100.52	430	140	388	12	386	24
CQ38_45	0.055	0.0034	0.473	0.027	0.0618	0.001	98.02	400	130	386.2	6.2	394	19
CQ38_46	0.0636	0.0071	0.732	0.076	0.0892	0.0036	95.31	600	200	549	21	576	40
CQ38_47	0.0725	0.0042	1.538	0.083	0.1527	0.0025	96.93	970	120	917	14	946	33
CQ38_48	0.0555	0.0031	0.401	0.021	0.04688	0.00087	86.49	440	120	295.8	5.3	342	15

CQ38_49	0.0726	0.0039	1.265	0.063	0.1239	0.0021	75.30	1000	110	753	12	831	28
CQ38_50	0.0938	0.0049	2.49	0.14	0.1902	0.0068	74.30	1510	110	1122	38	1266	51
CQ38_51	0.0677	0.0051	1.004	0.066	0.1096	0.0033	97.10	730	170	669	19	689	38
CQ38_52	0.0564	0.0033	0.485	0.027	0.06237	0.00098	97.48	440	130	389.9	6	400	19
CQ38_53	0.0589	0.0032	0.648	0.036	0.0786	0.0014	96.00	590	110	487.7	8.2	508	22
CQ38_54	0.0616	0.0033	0.674	0.033	0.0786	0.0011	93.00	650	110	487.3	6.8	524	20
CQ38_55	0.0732	0.0044	0.891	0.053	0.0886	0.0015	54.72	1000	120	547.2	8.8	648	29
CQ38_56	0.0789	0.0045	1.035	0.089	0.0958	0.0041	50.78	1160	110	589	24	726	40
CQ38_57	0.058	0.0032	0.604	0.031	0.075	0.0012	97.72	520	120	467.1	7.4	478	20
CQ38_58	0.0575	0.0031	0.603	0.03	0.0755	0.0011	97.89	500	120	468.9	6.3	479	19
CQ38_59	0.0678	0.0064	0.71	0.15	0.0759	0.0057	87.22	820	150	471	33	540	64
CQ38_60	0.1087	0.0099	1.4	0.58	0.096	0.017	33.20	1780	110	591	90	880	110
CQ38_61	0.0595	0.0039	0.541	0.034	0.0653	0.0012	93.70	530	140	407.6	7.2	435	22
CQ38_62	0.0565	0.0092	0.48	0.36	0.063	0.013	98.00	470	170	392	71	400	110
CQ38_63	0.0589	0.0046	0.57	0.12	0.0695	0.0092	95.37	510	140	433	53	454	55
CQ38_64	0.0692	0.0037	1.379	0.069	0.1447	0.0022	98.42	900	110	871	12	885	30
CQ38_65	0.0559	0.0035	0.496	0.029	0.0644	0.0012	98.34	400	130	403.2	7.5	410	20
CQ38_66	0.0581	0.0033	0.569	0.03	0.0712	0.0011	97.21	510	120	443.3	6.4	456	19
CQ38_67	0.0569	0.0035	0.559	0.037	0.0712	0.0021	98.66	470	130	443	12	449	23
CQ38_68	0.057	0.0032	0.63	0.033	0.0798	0.0012	99.82	490	120	495.1	7	496	20
CQ38_69	0.0565	0.0035	0.549	0.032	0.0701	0.0013	98.36	440	130	436.7	7.8	444	21
CQ38_70	0.056	0.011	0.48	0.56	0.063	0.016	98.25	410	210	392	77	399	73
CQ38_71	0.062	0.0045	0.576	0.039	0.0665	0.0014	90.20	630	150	414.9	8.7	460	24
CQ38_72	0.0576	0.0035	0.502	0.03	0.0626	0.0015	94.06	510	130	391.3	8.8	416	20
CQ38_73	0.0588	0.004	0.549	0.036	0.0673	0.0017	93.54	550	140	420	10	449	23
CQ38_74	0.0911	0.0056	2.53	0.17	0.2002	0.0074	81.45	1450	120	1181	39	1285	49
CQ38_75	0.0602	0.0037	0.695	0.039	0.0829	0.0017	96.07	590	130	513	10	534	23
CQ38_76	0.153	0.0078	7.89	0.38	0.3699	0.0058	85.13	2381	91	2027	27	2222	42
CQ38_77	0.0539	0.0036	0.471	0.031	0.0624	0.0013	100.59	320	140	390.3	8	388	21
CQ38_78	0.0568	0.0033	0.579	0.032	0.0746	0.0013	99.91	470	130	463.6	8	464	21

CQ38_79	0.0744	0.0046	1.92	0.11	0.1842	0.0034	103.71	1050	120	1089	18	1084	37
CQ38_80	0.0612	0.0035	0.55	0.029	0.0646	0.0011	90.83	640	120	403.3	6.7	444	19
CQ38_81	0.055	0.0036	0.536	0.034	0.0706	0.0013	100.78	390	130	439.4	8	436	23
CQ38_82	0.0571	0.0038	0.515	0.032	0.065	0.0013	96.55	490	130	405.5	7.7	420	21
CQ38_83	0.0689	0.004	1.118	0.061	0.1181	0.0019	95.12	870	120	721	11	758	30
CQ38_84	0.0872	0.0061	2.62	0.17	0.2181	0.0063	93.31	1360	130	1269	33	1293	49
CQ38_85	0.0772	0.0046	1.77	0.1	0.1648	0.0041	89.27	1100	130	982	23	1027	38
CQ38_86	0.0569	0.0034	0.586	0.034	0.0749	0.0012	99.70	480	130	465.6	7.4	467	21
CQ38_87	0.209	0.011	17.46	0.85	0.595	0.011	103.98	2911	85	3027	46	2964	48
CQ38_88	0.0845	0.0055	2.41	0.15	0.2114	0.0047	95.74	1290	130	1235	25	1243	43
CQ38_89	0.0578	0.0036	0.614	0.036	0.0774	0.0016	99.88	500	140	481.4	9.3	482	23
CQ38_90	0.055	0.0033	0.594	0.032	0.0764	0.0021	100.64	410	130	474	12	471	20
CQ38_91	0.0945	0.0049	2.73	0.13	0.2098	0.0037	80.66	1520	97	1226	20	1337	37
CQ38_92	0.0561	0.0032	0.529	0.029	0.0674	0.0011	97.81	440	130	420.6	6.9	430	19
CQ38_93	0.0556	0.0035	0.478	0.027	0.0621	0.0011	97.59	410	130	388.4	6.4	398	19
CQ38_94	0.1177	0.0065	3.67	0.22	0.2269	0.0057	69.07	1914	95	1322	29	1565	44
CQ38_95	0.0676	0.0036	1.292	0.065	0.1376	0.0023	99.05	840	110	833	13	841	29
CQ38_96	0.065	0.0046	0.863	0.084	0.0981	0.0047	94.96	730	140	603	27	635	40
CQ38_97	0.0661	0.005	1.011	0.084	0.1151	0.0048	100.14	750	160	701	27	700	41
CQ38_98	0.0599	0.0039	0.764	0.045	0.0914	0.0017	97.58	580	140	564	10	578	26
CQ38_99	0.0578	0.0033	0.589	0.031	0.074	0.0014	97.73	510	120	460.3	8.3	471	20
CQ38_100	0.0611	0.0034	0.613	0.032	0.0714	0.0012	91.86	640	120	444.6	7.4	484	20
CQ38_101	0.0559	0.0036	0.5	0.031	0.0644	0.0013	97.86	420	130	402.2	8.2	411	21
CQ38_102	0.0576	0.0032	0.634	0.033	0.0796	0.0014	98.88	500	120	493.4	8.3	499	20
CQ38_103	0.0558	0.0034	0.495	0.028	0.0639	0.0011	98.33	430	130	399.2	6.6	406	19
CQ38_104	0.074	0.0041	0.934	0.05	0.0904	0.0019	54.17	1030	120	558	12	666	27
CQ38_105	0.0565	0.0031	0.551	0.029	0.0703	0.0012	98.39	460	120	438.8	7	446	19
CQ38_106	0.0555	0.0035	0.493	0.029	0.06426	0.0009	98.38	420	130	401.4	5.5	408	19
CQ38_107	0.0679	0.0048	1.409	0.089	0.1485	0.0031	99.55	860	140	892	17	896	37
CQ38_108	0.0567	0.0034	0.498	0.028	0.0636	0.001	97.11	440	130	397.2	6.1	409	19

CQ38_109	0.1013	0.0051	3.91	0.19	0.2845	0.0073	98.72	1640	100	1619	38	1616	44
CQ38_110	0.0689	0.0039	0.669	0.034	0.0706	0.0011	84.92	880	120	439.9	6.6	518	21
CQ38_111	0.0567	0.004	0.553	0.034	0.0718	0.0013	100.18	450	140	446.8	8.1	446	22
CQ38_112	0.0573	0.0074	0.562	0.08	0.071	0.0017	98.00	480	150	442	10	451	37
CQ38_113	0.0572	0.0032	0.586	0.03	0.074	0.0011	98.61	510	120	460.5	6.8	467	19
CQ38_114	0.0697	0.0042	0.688	0.037	0.0716	0.0012	83.88	910	120	447.1	7.2	533	22
CQ38_115	0.0575	0.0033	0.569	0.028	0.0722	0.0011	97.93	510	120	449.5	6.5	459	19
CQ38_116	0.0551	0.0032	0.475	0.027	0.0625	0.0011	98.89	380	130	390.6	6.5	395	19
CQ38_117	0.0573	0.0031	0.622	0.031	0.0799	0.0011	100.69	490	120	495.4	6.7	492	20
CQ38_118	0.057	0.0031	0.602	0.03	0.0763	0.0013	99.29	480	120	473.6	7.8	477	19
CQ38_119	0.0565	0.0034	0.577	0.033	0.0745	0.0012	99.96	450	120	462.8	7.4	463	21
CQ38_120	0.0589	0.0033	0.622	0.032	0.0766	0.0012	96.84	560	120	475.5	7.2	491	20
CQ38_121	0.0559	0.0031	0.617	0.032	0.0789	0.0011	100.33	430	120	489.6	6.8	488	20
CQ38_122	0.0624	0.0041	0.744	0.073	0.087	0.0039	95.72	690	130	537	22	561	36
CQ38_123	0.0605	0.0031	0.536	0.026	0.06402	0.00075	91.53	620	110	400	4.6	437	17
CQ38_124	0.0594	0.0036	0.514	0.05	0.0631	0.0033	93.16	580	120	395	19	424	30
CQ38_125	0.0579	0.0031	0.544	0.028	0.068	0.0011	96.39	510	120	424.1	6.5	440	18
CQ38_126	0.0563	0.0038	0.519	0.032	0.0657	0.0011	97.20	450	130	410.2	6.5	422	21
CQ38_127	0.0871	0.0057	1.417	0.098	0.1191	0.0038	54.48	1340	130	730	22	899	44
CQ38_128	0.063	0.0037	0.649	0.036	0.0755	0.0018	92.14	690	110	469	11	509	22
CQ38_129	0.0575	0.0031	0.601	0.03	0.0749	0.0014	97.53	510	120	465.2	8.4	477	19
CQ38_130	0.0565	0.0034	0.52	0.029	0.0661	0.0012	96.78	460	120	412.3	7.3	426	19
CQ38_131	0.0743	0.0042	1.359	0.072	0.1321	0.0024	76.10	1050	110	799	14	870	31
CQ38_132	0.0558	0.0042	0.502	0.06	0.0649	0.0033	99.02	430	140	405	19	409	35
CQ38_133	0.0554	0.0032	0.51	0.028	0.0654	0.0012	97.75	410	120	408.6	7.1	418	19
CQ38_134	0.0577	0.0032	0.59	0.031	0.0734	0.0011	97.36	520	120	456.6	6.7	469	19
CQ38_135	0.0567	0.0035	0.497	0.031	0.0653	0.0013	99.85	430	130	407.4	7.6	408	20

APPENDIX I: U–Pb geochronology monazite results

Analysis	^{207}Pb/^{206}Pb	2σ	^{207}Pb/^{235}U	2σ	^{206}Pb/^{236}U	2σ	%Conc.	^{207}Pb/^{2006}Pb Age (Ma)	2σ	^{206}Pb/^{238}U Age (Ma)	2σ	^{207}Pb/^{235}U age (Ma)	2σ
QL-1													
MNZ_01	0.0682	0.0083	0.358	0.047	0.03702	0.00098	74.15	830	250	234.3	6.1	316	34
MNZ_02	0.066	0.014	0.34	0.1	0.0375	0.0017	79.00	720	220	237	10	300	50
MNZ_03	0.0523	0.0064	0.263	0.032	0.03595	0.00086	96.48	280	240	227.7	5.3	236	25
MNZ_04	0.0538	0.0093	0.27	0.053	0.0356	0.001	93.18	350	240	225.5	6.2	242	36
MNZ_05	0.067	0.017	0.345	0.092	0.0357	0.0013	75.15	800	240	226.2	8.3	301	52
MNZ_06	0.064	0.01	0.321	0.058	0.0353	0.0011	79.36	680	240	223.8	6.8	282	40
MNZ_07	0.254	0.069	1.8	1.3	0.073	0.015	15.35	2880	280	442	75	970	150
MNZ_08	0.0539	0.0085	0.26	0.042	0.03421	0.00078	92.65	350	240	216.8	4.9	234	31
MNZ_09	0.0573	0.0067	0.279	0.032	0.03432	0.00076	87.35	480	250	217.5	4.7	249	25
MNZ_10	–	–	0.5	5.5	0.048	0.047	78.95	850	470	300	180	380	330
MNZ_11	–	–	0.339	0.046	0.0375	0.0025	79.80	700	200	237	15	297	34
MNZ_12	–	–	0.304	0.047	0.0356	0.0026	83.96	590	180	225	16	268	34
MNZ_13	–	–	0.322	0.069	0.0368	0.0027	82.11	670	200	234	17	285	44
MNZ_14	–	–	0.326	0.065	0.0373	0.0027	82.81	640	180	236	17	285	42
MNZ_15	–	–	0.278	0.046	0.0363	0.0027	92.74	370	190	230	17	248	34
MNZ_16	–	–	0.292	0.038	0.0363	0.0023	88.80	460	180	230	15	259	29
MNZ_17	–	–	0.275	0.041	0.0351	0.0024	90.24	430	190	222	15	246	31
MNZ_18	–	–	0.361	0.046	0.0348	0.0023	21.15	1040	180	220	14	312	34
MNZ_19	–	–	0.264	0.033	0.0346	0.0022	92.41	410	180	219	14	237	26
MNZ_20	0.075	0.019	0.59	0.2	0.0577	0.0084	80.22	900	520	361	51	450	120
MNZ_21	0.1	0.029	0.57	0.23	0.0416	0.0062	16.86	1560	500	263	38	460	130
MNZ_22	0.056	0.017	0.27	0.11	0.0346	0.0053	92.02	440	560	219	33	238	87
MNZ_23	0.058	0.016	0.279	0.098	0.0342	0.0048	87.15	540	570	217	30	249	78
MNZ_24	0.065	0.031	0.32	0.25	0.035	0.0062	78.93	680	530	221	38	280	140
MNZ_25	0.073	0.055	0.49	0.39	0.0453	0.007	28.04	1020	490	286	42	400	190
MNZ_26	0.061	0.018	0.29	0.11	0.034	0.0051	82.44	620	520	216	32	262	85

MNZ_27	0.052	0.015	0.33	0.13	0.0452	0.0065	98.96	310	550	285	40	288	93
MNZ_28	0.058	0.011	0.49	0.12	0.0578	0.0034	88.73	460	410	362	20	408	86
MNZ_29	0.061	0.012	0.368	0.089	0.0392	0.002	78.23	610	400	248	12	317	65
MNZ_30	0.058	0.01	0.287	0.066	0.0344	0.0015	85.57	520	380	218.2	9.6	255	52
MNZ_31	0.062	0.012	0.5	0.12	0.0547	0.003	84.07	640	380	343	18	408	80
MNZ_32	0.065	0.012	0.35	0.082	0.0379	0.0018	78.69	750	370	240	11	305	63
MNZ_33	0.0537	0.0096	0.296	0.068	0.0387	0.0018	92.80	350	380	245	11	264	52
MNZ_34	0.116	0.022	0.71	0.17	0.0482	0.0026	19.80	1530	330	303	16	511	95
MNZ_35	0.063	0.011	0.44	0.1	0.0486	0.0021	82.93	670	380	306	13	369	71
MNZ_36	0.074	0.015	0.4	0.1	0.0364	0.0018	21.70	1060	370	230	11	346	69
MNZ_37	–	–	–	–	–	–	–	–	–	–	–	–	–
MNZ_38	0.0602	0.009	0.41	0.13	0.0489	0.0093	87.25	570	210	308	57	353	78
MNZ_39	0.063	0.024	0.42	0.44	0.046	0.012	83.43	690	260	292	67	350	120
MNZ_40	0.0565	0.0079	0.29	0.1	0.0363	0.0089	89.49	470	210	230	54	257	69
MNZ_41	–	–	–	–	–	–	–	–	–	–	–	–	–
MNZ_42	0.0595	0.0044	0.276	0.039	0.0335	0.0038	85.83	556	89	212	24	247	21
MNZ_43	0.0621	0.0054	0.282	0.065	0.0325	0.0048	82.07	610	120	206	30	251	43
MNZ_44	0.1037	0.0055	0.484	0.072	0.0334	0.0044	12.98	1633	94	212	27	395	47
MNZ_45	0.186	0.024	1.34	0.22	0.0527	0.0076	12.90	2590	210	334	46	843	90
MNZ_46	0.072	0.011	0.45	0.15	0.0443	0.0076	74.01	980	130	279	46	377	71
MNZ_47	0.072	0.0034	0.37	0.047	0.0374	0.0047	74.21	938	95	236	29	318	35
MNZ_48	0.059	0.01	0.32	0.11	0.0397	0.006	88.69	550	150	251	36	283	54
MNZ_49	0.059	0.012	0.29	0.14	0.0338	0.0058	84.25	570	160	214	36	254	74
MNZ_50	0.0555	0.0024	0.283	0.039	0.0365	0.0049	91.67	401	91	231	30	252	30
MNZ_51	0.0609	0.0072	0.282	0.063	0.0332	0.0048	84.06	610	180	211	30	251	40
MNZ_52	0.0584	0.006	0.279	0.067	0.0346	0.0049	87.95	510	120	219	30	249	46
MNZ_53	0.074	0.01	0.37	0.15	0.0368	0.0067	70.61	980	140	233	41	330	68
QL-2													
MNZ_01	0.806	0.028	96	14	0.87	0.13	78.07	4983	63	3890	340	4574	97
MNZ_02	0.2096	0.0071	1.18	0.14	0.0407	0.0044	8.94	2874	48	257	27	786	56

MNZ_03	0.461	0.012	4.56	0.62	0.0706	0.0092	10.72	4106	34	440	55	1729	82
MNZ_04	0.1154	0.0042	0.564	0.073	0.0354	0.0037	11.93	1877	48	224	23	451	42
MNZ_05	0.11	0.017	0.52	0.26	0.0346	0.0052	12.23	1790	110	219	31	422	81
MNZ_06	0.3165	0.0085	2.12	0.2	0.0483	0.0048	8.60	3534	43	304	30	1148	66
MNZ_07	0.163	0.0085	0.78	0.12	0.035	0.0038	9.07	2448	63	222	24	583	52
MNZ_08	0.223	0.014	1.21	0.56	0.0389	0.0084	8.22	2993	40	246	50	802	75
MNZ_09	0.72	0.037	1310	240	11.6	2.2	257.69	4812	94	1.24E+04	1.50E+03	5690	470
MNZ_10	0.1013	0.0066	0.48	0.082	0.0348	0.0036	13.57	1628	81	221	22	394	31
MNZ_11	0.2409	0.0076	1.711	0.087	0.0512	0.0023	10.30	3116	50	321	14	991	29
MNZ_12	0.281	0.014	2.15	0.17	0.0542	0.0028	10.11	3362	80	340	17	1146	53
MNZ_13	0.25	0.012	1.65	0.12	0.046	0.0022	9.08	3193	81	290	14	977	45
MNZ_14	0.282	0.015	1.93	0.16	0.0473	0.0022	9.12	3268	92	298	14	1037	50
MNZ_15	0.1117	0.005	0.565	0.03	0.0358	0.0018	12.58	1804	79	227	11	453	19
MNZ_16	0.5	0.014	5.05	0.23	0.0726	0.0033	10.67	4236	43	452	20	1823	39
MNZ_17	0.242	0.014	1.54	0.12	0.0442	0.0021	9.04	3087	83	279	13	931	46
MNZ_18	0.161	0.0081	0.9	0.066	0.0386	0.0019	9.90	2464	84	244	12	646	34
MNZ_19	0.1267	0.0062	0.62	0.039	0.0351	0.0015	10.94	2037	91	222.9	9.4	486	25
MNZ_20	0.1203	0.0045	0.661	0.053	0.04	0.0025	13.09	1933	68	253	16	511	32
MNZ_21	0.23	0.013	1.41	0.13	0.0459	0.0032	9.54	3028	92	289	19	882	55
MNZ_22	0.1398	0.0084	0.706	0.06	0.0392	0.0028	11.22	2210	100	248	17	541	36
MNZ_23	0.282	0.013	1.89	0.17	0.0467	0.003	8.86	3320	73	294	19	1055	61
MNZ_24	0.331	0.016	2.34	0.2	0.0523	0.0039	9.08	3624	83	329	24	1229	56
MNZ_25	0.218	0.013	1.2	0.12	0.0398	0.0027	8.57	2939	98	252	17	784	56
MNZ_26	0.274	0.014	1.58	0.17	0.0424	0.003	8.09	3301	80	267	18	956	63
MNZ_27	0.611	0.023	14.1	1.5	0.184	0.02	22.44	4523	60	1015	88	2590	110
MNZ_28	0.274	0.01	1.83	0.15	0.0474	0.003	9.03	3299	61	298	19	1032	56
MNZ_29	0.681	0.027	17.5	1.6	0.184	0.014	22.99	4675	65	1075	74	2911	82
MNZ_30	0.1743	0.0063	1.322	0.098	0.0543	0.0026	13.16	2591	58	341	16	854	40
MNZ_31	0.27	0.012	1.91	0.22	0.0508	0.0032	9.74	3276	57	319	19	1068	56
MNZ_32	0.23	0.015	1.37	0.24	0.0439	0.0034	9.11	3042	63	277	21	870	58

MNZ_33	0.449	0.016	4.36	0.35	0.0722	0.0047	10.99	4087	51	449	28	1704	52
MNZ_34	0.1966	0.0062	1.167	0.081	0.0434	0.0022	9.90	2768	50	274	13	780	35
MNZ_35	0.158	0.01	0.87	0.12	0.04	0.0023	10.52	2404	81	253	14	636	49
MNZ_36	0.308	0.016	2.2	0.2	0.0519	0.0032	9.47	3443	70	326	19	1144	49
MNZ_37	0.1597	0.0062	0.844	0.085	0.0384	0.0021	9.91	2451	50	243	13	616	37
MNZ_38	–	–	–	–	–	–	–	–	–	–	–	–	–
MNZ_39	0.578	0.043	8.28	0.83	0.1017	0.0086	14.35	4300	130	617	49	2155	81
MNZ_40	0.573	0.022	8.17	0.6	0.1038	0.0063	14.36	4436	55	637	36	2244	63
MNZ_41	0.387	0.024	3.66	0.75	0.0592	0.0079	9.66	3831	73	370	45	1548	81
MNZ_42	0.269	0.013	1.82	0.14	0.0452	0.0028	8.71	3273	82	285	17	1020	49
MNZ_43	0.246	0.012	1.53	0.12	0.0453	0.0027	9.09	3137	77	285	17	926	47
MNZ_44	0.2098	0.0094	1.322	0.094	0.0459	0.0027	10.00	2891	73	289	17	849	41
MNZ_45	0.119	0.022	0.62	0.34	0.0366	0.0042	11.96	1940	140	232	24	490	70
MNZ_46	0.376	0.016	3.1	0.22	0.0601	0.0035	9.86	3815	63	376	21	1421	53
MNZ_47	0.4	0.032	5.8	1.9	0.077	0.017	12.02	3953	75	475	84	1877	76
MNZ_48	0.128	0.014	0.93	0.2	0.0523	0.0042	16.24	2020	120	328	25	652	72
QL-3													
MNZ_01	0.053	0.044	0.31	0.4	0.0429	0.0075	100.00	220	580	270	39	270	140
MNZ_02	0.164	0.048	1.05	0.35	0.0474	0.0033	12.84	2320	510	298	18	710	170
MNZ_03	0.064	0.018	0.32	0.1	0.0374	0.0015	84.39	670	550	236.3	9.2	280	76
MNZ_04	0.17	0.12	1.7	1.9	0.0687	0.0091	16.36	2610	520	427	52	1040	300
MNZ_05	0.058	0.021	0.31	0.14	0.0404	0.0016	92.06	440	550	255	10	277	95
MNZ_06	0.069	0.022	0.34	0.13	0.0358	0.0015	76.26	920	560	226.5	9.2	297	95
MNZ_07	0.056	0.018	0.29	0.1	0.0375	0.0014	92.18	410	550	236.9	8.6	257	76
MNZ_08	0.059	0.017	0.289	0.092	0.0359	0.0013	88.02	510	570	227.1	7.9	258	72
MNZ_09	0.062	0.019	0.29	0.1	0.0357	0.0014	87.94	590	560	226	8.4	257	72
MNZ_10	0.08	0.026	0.38	0.15	0.0365	0.0014	20.61	1120	540	230.8	8.5	330	100
MNZ_11	0.0561	0.0083	0.295	0.05	0.0378	0.0028	91.92	420	290	239	17	260	39
MNZ_12	0.0539	0.0079	0.282	0.047	0.0374	0.0027	94.80	310	290	237	17	250	37
MNZ_13	0.0532	0.008	0.277	0.048	0.036	0.0027	92.31	330	320	228	17	247	38

MNZ_14	0.0536	0.0079	0.268	0.045	0.0355	0.0027	93.75	330	300	225	17	240	36
MNZ_15	0.0575	0.0085	0.287	0.049	0.0355	0.0027	88.24	480	300	225	17	255	38
MNZ_16	0.075	0.013	0.346	0.063	0.0346	0.0027	75.00	730	330	219	17	292	48
MNZ_17	0.102	0.024	0.75	0.17	0.0496	0.0069	18.25	1710	330	312	43	560	100
MNZ_18	0.0501	0.0072	0.235	0.039	0.0337	0.0025	100.47	190	290	214	16	213	32
MNZ_19	0.09	0.015	0.54	0.1	0.0429	0.0036	19.64	1380	290	271	22	440	68
MNZ_20	0.077	0.012	0.413	0.073	0.039	0.0032	23.98	1030	310	247	20	347	53
MNZ_21	0.073	0.029	0.44	0.22	0.0401	0.006	68.38	970	530	253	37	370	120
MNZ_22	0.08	0.024	0.42	0.18	0.0416	0.0061	23.60	1110	570	262	38	350	120
MNZ_23	0.071	0.031	0.56	0.26	0.0484	0.0074	67.78	980	530	305	45	450	160
MNZ_24	0.055	0.02	0.32	0.14	0.0367	0.0055	82.86	410	610	232	34	280	100
MNZ_25	0.059	0.021	0.3	0.14	0.0367	0.0056	87.22	480	530	232	35	266	95
MNZ_26	0.079	0.023	0.18	0.2	0.0307	0.0055	18.75	1040	590	195	34	160	130
MNZ_27	0.056	0.018	0.29	0.12	0.0355	0.0052	85.23	430	600	225	33	264	90
MNZ_28	0.051	0.015	0.259	0.089	0.0343	0.0048	93.16	230	610	218	30	234	73
MNZ_29	0.093	0.029	0.2	0.22	0.0299	0.0054	15.32	1240	530	190	34	180	140
MNZ_30	0.196	0.069	0.48	0.8	0.0384	0.0081	9.76	2490	530	243	49	390	240
MNZ_31	0.0851	0.0072	0.408	0.063	0.0359	0.0045	19.91	1140	140	227	28	343	41
MNZ_32	0.0642	0.003	0.314	0.035	0.0358	0.0043	82.85	659	93	227	27	274	27
MNZ_33	0.0553	0.0015	0.27	0.029	0.0358	0.0042	93.42	408	58	227	26	243	23
MNZ_34	0.405	0.042	12.3	2.1	0.195	0.038	28.49	3720	180	1060	160	2280	170
MNZ_35	0.414	0.087	19.8	6.1	0.175	0.059	25.07	3470	350	870	240	2330	380
MNZ_36	0.1106	0.0076	0.61	0.075	0.0419	0.005	15.96	1660	130	265	30	471	45
MNZ_37	–	–	–	–	–	–	–	–	–	–	–	–	–
MNZ_38	0.0721	0.004	0.376	0.044	0.0378	0.0045	74.22	890	110	239	28	322	32
MNZ_39	0.326	0.042	3.8	0.57	0.078	0.011	17.89	2660	350	476	67	1310	140
MNZ_40	0.0602	0.0024	0.3	0.02	0.0365	0.0017	86.84	591	80	231	10	266	15
MNZ_41	0.0702	0.0051	0.343	0.032	0.0354	0.0017	76.19	810	120	224	10	294	22
MNZ_42	0.0657	0.0053	0.319	0.032	0.0357	0.0018	80.43	670	140	226	11	281	22
MNZ_43	0.094	0.0067	0.466	0.043	0.0353	0.0018	15.93	1400	130	223	11	386	28

MNZ_44	0.0777	0.0074	0.399	0.046	0.0364	0.0019	21.70	1060	130	230	12	339	30
MNZ_45	0.152	0.012	0.9	0.095	0.0433	0.0022	11.87	2300	120	273	14	634	44
MNZ_46	0.0623	0.0022	0.307	0.019	0.0363	0.0017	84.56	658	73	230	10	272	14
MNZ_47	0.106	0.021	0.61	0.16	0.0419	0.004	15.81	1670	170	264	24	465	63
MNZ_48	0.0537	0.0021	0.248	0.016	0.034	0.0016	95.98	336	79	215	10	224	12
MNZ_49	0.284	0.04	2.03	0.28	0.0514	0.0055	15.19	2100	380	319	33	910	100
CQ38S1													
MNZ_01	0.1	0.01	0.91	0.11	0.0685	0.0011	28.10	1520	220	427.1	6.7	643	61
MNZ_02	0.0714	0.0068	0.728	0.084	0.0638	0.0012	71.77	980	180	398.3	7.2	555	48
MNZ_03	0.0801	0.0075	0.692	0.075	0.0625	0.0015	32.53	1200	190	390.4	8.8	534	43
MNZ_04	0.076	0.014	0.67	0.18	0.0647	0.0013	38.14	1060	200	404.3	8	518	79
MNZ_05	0.0637	0.0058	0.629	0.067	0.06218	0.00099	78.70	720	190	388.8	6	494	42
MNZ_06	0.0717	0.0066	0.621	0.068	0.0629	0.001	80.41	980	190	393.2	6.3	489	43
MNZ_07	0.0621	0.006	0.615	0.067	0.0656	0.0011	84.47	990	190	409.7	6.5	485	42
MNZ_08	0.0721	0.0066	0.615	0.069	0.06468	0.00091	83.13	680	200	404	5.5	486	43
MNZ_09	0.0671	0.0062	0.599	0.065	0.06552	0.00099	85.77	830	190	409.1	6	477	40
MNZ_10	0.065	0.0065	0.597	0.071	0.0658	0.001	86.89	740	190	411	6.3	473	43
MNZ_11	0.068	0.0063	0.587	0.065	0.06349	0.00092	84.58	840	180	396.7	5.6	469	41
MNZ_12	0.0632	0.0058	0.581	0.065	0.0575	0.0011	77.46	710	190	360.2	6.8	465	40
MNZ_13	0.0648	0.006	0.567	0.062	0.0645	0.001	88.79	750	200	403.1	6.4	454	40
MNZ_14	0.0649	0.0059	0.559	0.061	0.0644	0.001	89.29	770	190	402.7	6.1	451	40
MNZ_15	0.0591	0.0053	0.555	0.059	0.06063	0.00098	84.69	560	190	379.4	5.9	448	38
MNZ_16	0.0645	0.0058	0.554	0.06	0.05523	0.00091	77.34	750	190	346.5	5.6	448	40
MNZ_17	0.0612	0.0055	0.553	0.058	0.05591	0.00074	78.46	650	190	350.7	4.5	447	39
MNZ_18	0.06	0.0056	0.547	0.06	0.06613	0.00094	93.18	600	200	412.8	5.7	443	39
MNZ_19	0.0622	0.0056	0.539	0.061	0.05453	0.00096	78.13	690	190	342.2	5.8	438	40
MNZ_20	0.0617	0.0057	0.538	0.059	0.06568	0.00091	93.61	660	190	410	5.5	438	39
MNZ_21	0.0601	0.0056	0.534	0.059	0.0639	0.001	92.19	590	190	399.2	6.3	433	38
MNZ_22	0.062	0.0056	0.529	0.056	0.06242	0.00095	90.53	670	190	390.2	5.8	431	38
MNZ_23	0.0635	0.0061	0.528	0.06	0.06215	0.00086	90.37	720	190	388.6	5.2	430	39

MNZ_24	0.0619	0.0056	0.526	0.057	0.06448	0.00093	93.87	670	190	402.7	5.6	429	38
MNZ_25	0.0584	0.0053	0.522	0.055	0.0602	0.001	88.24	550	200	376.8	6.2	427	37
MNZ_26	0.0585	0.0053	0.521	0.057	0.06457	0.00095	94.89	540	190	403.3	5.7	425	38
MNZ_27	0.06	0.041	0.52	0.89	0.0651	0.0071	96.90	600	330	407	41	420	180
MNZ_28	0.0598	0.0074	0.52	0.12	0.0656	0.0039	96.25	590	180	411	23	427	54
MNZ_29	0.0571	0.0052	0.516	0.056	0.0647	0.001	95.53	490	200	404.1	6.3	423	38
MNZ_30	0.0594	0.0055	0.515	0.055	0.06424	0.00092	95.32	610	200	401.3	5.6	421	37
MNZ_31	0.0578	0.0053	0.513	0.056	0.06431	0.00095	95.42	520	200	401.7	5.8	421	37
MNZ_32	0.0572	0.0052	0.509	0.055	0.06457	0.00096	96.48	500	200	403.3	5.8	418	37
MNZ_33	0.0572	0.0052	0.504	0.055	0.06557	0.00091	98.65	540	200	409.4	5.5	415	37
MNZ_34	0.0584	0.0053	0.504	0.055	0.0656	0.001	99.10	520	200	409.3	6.3	413	37
MNZ_35	0.0574	0.0053	0.504	0.055	0.06516	0.00098	98.17	500	210	407.4	5.9	415	37
MNZ_36	0.0595	0.007	0.503	0.054	0.0654	0.001	98.91	500	190	408.5	6.3	413	37
MNZ_37	0.0571	0.0052	0.503	0.073	0.062	0.0011	93.85	570	200	387.6	6.4	413	44
MNZ_38	0.0552	0.005	0.501	0.054	0.06527	0.00099	98.91	420	210	407.5	6	412	36
MNZ_39	0.0577	0.0053	0.499	0.054	0.06594	0.00095	99.90	510	190	411.6	5.7	412	36
MNZ_40	0.0581	0.0052	0.498	0.054	0.0625	0.00088	95.09	530	200	390.8	5.4	411	36
MNZ_41	0.0574	0.0052	0.498	0.053	0.0644	0.001	98.27	410	210	402.9	6.1	410	36
MNZ_42	0.0551	0.005	0.498	0.054	0.06387	0.00097	97.34	510	200	399.1	5.9	410	37
MNZ_43	0.0568	0.0052	0.497	0.057	0.06613	0.00098	100.93	420	200	412.8	5.9	409	38
MNZ_44	0.0554	0.0053	0.497	0.054	0.0654	0.00093	99.59	470	190	408.3	5.7	410	37
MNZ_45	0.0569	0.0052	0.496	0.055	0.06385	0.00095	97.79	470	200	399	5.9	408	37
MNZ_46	0.057	0.0052	0.493	0.054	0.06387	0.00093	97.82	490	200	399.1	5.6	408	36
MNZ_47	0.0566	0.0051	0.493	0.054	0.06562	0.0009	100.91	470	200	409.7	5.4	406	37
MNZ_48	0.0564	0.0051	0.488	0.053	0.06462	0.00098	100.15	460	210	403.6	5.9	403	36
MNZ_49	0.0605	0.0055	0.485	0.053	0.0575	0.00094	89.85	620	200	360.3	5.8	401	37
MNZ_50	0.0556	0.005	0.484	0.052	0.06392	0.00094	99.60	430	200	399.4	5.7	401	35
MNZ_51	0.057	0.0052	0.483	0.052	0.06218	0.00099	96.96	490	200	388.8	6	401	35
MNZ_52	0.0569	0.0055	0.481	0.056	0.06118	0.0009	96.18	490	170	382.8	5.5	398	34
MNZ_53	0.0565	0.0052	0.48	0.052	0.06478	0.0009	101.40	470	200	404.6	5.4	399	36

MNZ_54	0.0551	0.005	0.479	0.052	0.06379	0.00092	100.40	420	210	398.6	5.6	397	36
MNZ_55	0.0582	0.0059	0.478	0.061	0.0628	0.0011	99.17	530	190	392.7	6.7	396	36
MNZ_56	0.0565	0.0051	0.478	0.053	0.064	0.0013	100.68	460	200	399.7	7.8	397	36
MNZ_57	0.0539	0.0049	0.477	0.051	0.06337	0.00085	100.03	360	200	396.1	5.1	396	35
MNZ_58	0.0551	0.005	0.476	0.051	0.0645	0.00098	101.74	410	200	402.9	5.9	396	35
MNZ_59	0.0569	0.0052	0.475	0.052	0.06241	0.00097	98.54	480	200	390.2	5.9	396	36
MNZ_60	0.0562	0.0052	0.475	0.052	0.06286	0.00091	99.47	450	200	392.9	5.5	395	36
MNZ_61	0.0555	0.005	0.474	0.05	0.06197	0.00089	98.13	430	210	387.6	5.4	395	34
MNZ_62	0.0555	0.005	0.474	0.051	0.06342	0.00095	100.61	450	200	396.4	5.7	394	36
MNZ_63	0.0564	0.0051	0.473	0.051	0.06298	0.00084	100.18	470	200	393.7	5.1	393	35
MNZ_64	0.0568	0.0051	0.468	0.051	0.06048	0.00096	97.30	490	190	378.5	5.8	389	35
MNZ_65	0.0554	0.005	0.467	0.05	0.06259	0.00098	100.33	420	200	391.3	6	390	35
MNZ_66	0.0554	0.005	0.466	0.051	0.06185	0.00086	99.69	430	200	386.8	5.2	388	35
MNZ_67	0.056	0.0053	0.465	0.053	0.06053	0.00087	98.01	460	190	379.3	5.3	387	33
MNZ_68	0.0542	0.0049	0.461	0.05	0.0612	0.0009	99.71	370	200	382.9	5.4	384	35
MNZ_69	0.0558	0.0086	0.46	0.11	0.0626	0.0021	101.82	440	200	392	12	385	55
MNZ_70	0.0537	0.0049	0.459	0.05	0.06178	0.00096	100.89	360	210	386.4	5.8	383	34
MNZ_71	0.0557	0.0051	0.455	0.051	0.06054	0.00092	99.68	440	200	378.8	5.6	380	35
MNZ_72	0.053	0.0049	0.449	0.048	0.05904	0.00091	97.83	330	210	369.8	5.6	378	34
MNZ_73	0.0545	0.005	0.446	0.049	0.05925	0.00089	98.93	390	200	371	5.4	375	34
MNZ_74	0.055	0.017	0.43	0.17	0.0575	0.0015	98.50	430	260	360.5	8.9	366	81
MNZ_75	0.057	0.0052	0.425	0.046	0.05426	0.0008	94.87	490	200	340.6	4.9	359	33
MNZ_76	0.0545	0.0049	0.42	0.048	0.0566	0.001	99.69	390	200	354.9	6.1	356	34
MNZ_77	0.0573	0.0052	0.415	0.045	0.05266	0.00093	93.98	500	200	330.8	5.7	352	33
MNZ_78	0.054	0.0049	0.411	0.045	0.05741	0.00075	102.83	370	200	359.9	4.6	350	32
MNZ_79	0.0539	0.0053	0.405	0.042	0.0553	0.0016	100.87	360	190	348	10	345	32

APPENDIX J: Range of chemistry for selected minerals

Range of chemistry for selected minerals. Representative analyses are given in.

	QL-1	CQ38S1	2QS2	4QS4
Garnet core				
X_{alm}	–	0.573–0.638	-	-
X_{py}	–	0.061–0.074	-	-
X_{grs}	–	0.069–0.086	-	-
X_{sps}	–	0.208–0.278	-	-
Garnet Rim				
X_{alm}	–	0.617–0.714	-	-
X_{py}	–	0.069–0.111	-	-
X_{grs}	–	0.070–0.085	-	-
X_{sps}	–	0.10–0.20	-	-
Cordierite				
X_{Fe}	-	-	0.377–0.382	-
Biotite				
F (wt%)	0.261–0.384	0.20–0.27	0.526–0.528	0.318–0.322
Cl (wt%)	0.014–0.037	0.014–0.036	0.017–0.040	0.005–0.013
TiO2 (wt%)	1.867–2.103	1.249–1.256	1.295–1.453	2.438–2.938
X_{bi}	0.437–0.442	0.474–0.497	0.474–0.487	0.541–0.571
Muscovite				
n(mu)	–	0.122–0.161	0.127–0.135	0.089–0.094
c(mu)	–	0.000–0.002	0	0.001–0.003
p(mu)	–	0.716–0.746	0.687–0.678	0.1–0.772
p(cel)	–	0.050–0.069	0.056–0.058	0.055–0.406
p(fcel)	–	0.050–0.062	0.128–0.131	0.071–0.404
Plagioclase				
p(ab)	0.937–0.940	–	-	0.878
p(an)	0.058–0.061	–	-	0.118
p(san)	0.002	–	-	0.004
Ilmenite				
g(ilm)	–	0.001–0.19	0.001	0.001–0.007
m(ilm)	–	0.061–0.070	0.085–0.104	0.018–0.050
p(ilm)	–	0.937–1.016	0.823–0.895	0.950–0.989
p(hem)	–	(-ve)	0.005–0.090	0.000–0.014
MnO (wt%)	–	1.159–4.708	3.913–4.755	0.827–2.249
TiO2 (wt%)	–	50.189–52.242	47.052–51.063	50.871–53.187

X_{alm}=Fe^{2+}/(Fe^{2+}+Mg+Ca+Mn), X_{py}=Mg/(Fe^{2+}+Mg+Ca+Mn), X_{grs}=Ca/Fe^{2+}+Mg+Ca+Mn), Xsps=Mn/(Fe^{2+}+Mg+Ca+Mn), X_{bi}=Fe/(Fe^{2+}+Mg)

Garnet

Garnet in CQ38S1 is predominantly alamandine-spessartine mixtures, with core X_{alm} of and core X_{spss} of. Consistent with prograde garnet zonation. Neither X_{grs} nor X_{py} show significant zonation. Negligible increase of X_{grs} and decrease of X_{py} towards the core.

Cordierite + Feldspars

2QS2 is the only sample preserving cordierite which isn't wholly pinitized. The range of X_{Fe} values occur between 0.377-0.382. Plagioclase occurs in all samples, but was only analysed in QL-1 and 4QS4—both are identified as albite, QL-1 P_{ab} = 0.937-0.940 and 4QS4 P_{ab} = 0.878.

Biotite

Biotite in all samples is relatively titanium-low, with TiO_2 values of 1.248–2.938 wt%. Sample 4QS4 is most titanium-rich, 2.438–2.938 wt%. Samples QL-1, CQ38S1 and 2QS2 have higher Cl contents (0.014–0.04) than sample 4QS4 (0.005–0.013). 2QS2 has the highest F contents (0.526–0.528) compared to the QL-1, CQ38S1 and 4QS4 (0.20–0.322).

Muscovite

Samples CQ38S1, 2QS2 and 4QS4 consist of 67–77% muscovite component. Of that muscovite component, the paragonite component (amount of Na_2O) occurs between 9–16%.

Ilmenite

QL-1 is ilmenite absent, containing rutile. Samples CQ38S1, 2QS2 and 4QS4 contain 0.827–4.708 wt% MnO and 47.052–53.187 wt% TiO_2. Higher wt% MnO values occur in 2QS2.

APPENDIX K: EPMA methods

Bulk rock and mineral chemistry methodologies follow those of Tucker et al. (2015). Chemical compositions of garnet, cordierite, andalusite, staurolite, plagioclase, chlorite, biotite, muscovite, ilmenite, rutile and magnetite were acquired utilizing a Cameca SXFive electron microprobe at Adelaide Microscopy, The University of Adelaide following the methodology of Tucker et al. (2015). For each spot analysis, a beam current of 20 nA and accelerating voltage of 15 kV was set, and a PAP correction was applied to all data. Each analysis resulted in measurements of SiO2, TiO2, Cr2O3, Al2O3, FeO, MnO, MgO, CaO, Na2O, K2O, ZnO, Cl and F using Wavelength Dispersive Spectrometers (WDS). Callibration was undertaken on natural and synthetic mineral standards, following standard protocols used at Adelaide Microscopy.

APPENDIX L: Extended geochronology methods

U–Pb ISOTOPIC DATING OF ZIRCON AND MONAZITE

Methodologies follow those of Payne et al. (2008). Mounted zircon and monazite grains were imaged using a Quanta 600 Scanning Electron Microscope (SEM), with an attached Gatan Cathodoluminesence (CL) detector (utilized specifically for mounted zircon grains) at Adelaide Microscopy, The University of Adelaide. Zircon in the <79 μm fraction did not show complex internal structure due to grain size (commonly <30 μm). Zircon grains of ~30 μm did, however, show brightness e.g. Fig. 8c. The use of Electron-Dispersive Spectroscopy (EDS) x-ray spot analysis confirmed zircon. Monazites were identified on the basis of brightness (brightest observable grains). In-situ monazite grains in samples QL-1, QL-2 and

QL-3 were imaged using a back-scattered electron (BSE) detector on a Quanta 600 SEM to determine their microstructural locations.

U–Pb DATA ACQUISITION

U–Pb isotopic data were collected using Laser Ablation–Inductively Coupled Plasma–Mass Spectrometry (LA–ICP–MS) on mounted monazite and zircon grains, and in-situ (thin-section) for additional monazite grains. LA–ICP–MS analyses were done at the University of Adelaide, following the method of Payne et al. (2008). Zircon and monazite acquisition was undertaken with 30 seconds of background measurement and 30 seconds of sample ablation.

Zircon U-Pb isotopic analyses (QL-3, 2QS2, 4QS4 and CQ38S1) were acquired using a ASI M50 laser coupled with an Agilent 7700 ICP–MS. Ablation of zircon in all samples was performed with a frequency of 5 Hz and a spot size of 20 µm. Monazite U–Pb isotopic analyses (samples QL-1, QL-2 and QL-3) were acquired using a New Wave 213 nm Nd–YAG laser coupled with an Agilent 7500cs ICP–MS (spot size 15 µm, ablation in a He atmosphere and laser frequency of 4 Hz). U–Pb isotopic analyses for sample CQ38S1 were acquired using an ASI M50 laser coupled with an Agilent 7700 ICP–MS (spot size of 20 µm in a He atmosphere and laser frequency of 5 Hz).

DATA REDUCTION AND PROCESSING

Zircon and monazite isotopic data were reduced using Iolite software (Paton et al., 2011). Elemental fractionation and mass bias for zircon geochronology was corrected using the primary zircon standard GJ (TIMS normalisation data: $^{207}Pb/^{206}Pb$ = 608.3 Ma, $^{206}Pb/^{238}U$ = 600.7 Ma and $^{207}Pb/^{235}U$ = 602.2 Ma; (Payne et al., 2008). For monazite, primary standard MAdel was used (TIMS normalisation data: $^{207}Pb/^{206}Pb$ = 491.0 ± 2.7 Ma, $^{206}Pb/^{239}U$ = 518.37 ± 0.99 Ma and $^{207}Pb/^{235}U$ = 513.13. ± 0.19 Ma: updated from Payne et al. (2008) with additional TIMS analyses). Data accuracy was monitored by the use of secondary standards, including 94-222/Bruna-NW (SHRIMP data: $^{206}Pb/^{238}U$ 450.2 ± 3.4 Ma), MtGt (~325 Ma) and Ambat (~525 Ma).

Bracketing zircon and monazite analyses on unknowns accounted for instrument drift—10 unknown zircon analyses were done before bracketing, and 5–6 unknown monazite analyses were done before bracketing. Weighted average ages of standard analyses in this study are provided in. Ages quoted in this study are predominantly $^{206}Pb/^{238}U$ due to the majority of data being <1000 Ma. However, ages >1,000 Ma are quoted as $^{207}Pb/^{206}Pb$ ages. All errors are at the 2σ level unless stated otherwise. Concordance was calculated using the ratio ($^{206}Pb/^{238}U$) / ($^{207}Pb/^{206}Pb$).

Weighted average ages collected for in-situ monazite analyses (samples QL-1, QL-2 and QL-3) throughout the course of this study for the primary (MADel) and in-house (222, MtGarnet and Ambat) monazite standards; MADel are $^{207}Pb/^{206}Pb$ = 495±20 Ma (n = 147, MSWD = 15), $^{206}Pb/^{238}U$ = 517 ± 1.9 Ma (n = 147, MSWD = 0.99), and $^{207}Pb/^{235}U$ = 513.5 ± 4.1 Ma (n = 147, MSWD = 2.3). 222 were $^{207}Pb/^{206}Pb$ = 420.7±8.4 Ma (n = 49, MSWD = 0.96), $^{206}Pb/^{238}U$ = 447 ± 13 Ma (n = 49, MSWD = 17), and $^{207}Pb/^{235}U$ = 449.1 ± 6.8 Ma (n = 49, MSWD = 2.6). MtGarnet are $^{207}Pb/^{206}Pb$ = 473.2 ± 8.3 Ma (n = 48, MSWD = 1.09), $^{206}Pb/^{238}U$ = 328.6 ± 9.7 Ma (n = 48, MSWD = 12), and $^{207}Pb/^{235}U$ = 346 ± 14 Ma (n = 48, MSWD = 12). Ambat are $^{207}Pb/^{206}Pb$ = 473.2 ± 8.3 Ma (n = 48, MSWD = 1.09), $^{206}Pb/^{238}U$ =537 ± 17 Ma (n = 48, MSWD = 23), and $^{207}Pb/^{235}U$ = 508 ± 5.6 Ma (n = 48, MSWD = 1.4).

Weighted average ages collected for expoy resin mounted monazite analyses in sample CQ38S1 analyses throughout the course of this study for the primary (MADel) and in-house (222, MtGarnet and Ambat) monazite standards; MADel are $^{207}Pb/^{206}Pb$ = 490 ± 23 Ma (n = 75, MSWD = 0.30), $^{206}Pb/^{238}U$ = 518.37 ± 0.86 Ma (n = 75, MSWD = 0.85), and $^{207}Pb/^{235}U$ = 513 ± 5 Ma (n = 75, MSWD = 0.18). 222 were $^{207}Pb/^{206}Pb$ = 443 ± 47 Ma (n = 18, MSWD = 0.25), $^{206}Pb/^{238}U$ = 446.1 ± 1.7 Ma (n = 18, MSWD = 1.3), and $^{207}Pb/^{235}U$ = 446.6 ± 9.1 Ma (n = 18, MSWD = 0.44). MtGarnet are $^{207}Pb/^{206}Pb$ = 423 ± 98 Ma (n = 18, MSWD = 3.8), $^{206}Pb/^{238}U$ = 318.4 ± 3.4 Ma (n = 18, MSWD = 6.8), and $^{207}Pb/^{235}U$ = 328 ± 12 Ma (n = 18, MSWD = 2.2). Ambat are $^{207}Pb/^{206}Pb$ = 575 ± 130 Ma (n = 18, MSWD = 6.5), $^{206}Pb/^{238}U$ = 514.7 ± 3.1 Ma (n = 18, MSWD = 3.3), and $^{207}Pb/^{235}U$ = 519 ± 23 Ma (n = 18, MSWD = 4.3).

Weighted average ages collected for epoxy resin mounted zircon analyses in sample QL-3, 2QS2, 4QS4 and CQ38S1 analyses throughout the course of this study for the primary (GJ) and in-house PLES zircon standards; GJ are $^{207}Pb/^{206}Pb$ = 560 ± 13 Ma (n = 156, MSWD = 0.99), $^{206}Pb/^{238}U$ = 601.8 ± 1.1 Ma (n = 156, MSWD = 0.82), and $^{207}Pb/^{235}U$ = 601.7 ± 2.8 Ma (n = 156, MSWD = 0.99). PLES are $^{207}Pb/^{206}Pb$ = 292 ± 21 Ma (n = 62, MSWD = 1.3), $^{206}Pb/^{238}U$ = 388.9 ± 1.1 Ma (n = 62, MSWD = 1.5), and $^{207}Pb/^{235}U$ = 336.7 ± 3.0 Ma (n = 62, MSWD = 1.4).